DISSERTATION

SPECTROSCOPY OF HIGH ANGULAR MOMENTUM RYDBERG STATES WITH $^2S_{1/2}$ ION CORES

Submitted by

Erica Lynn Snow

Physics

In partial fulfillment of the requirements

For the Degree of Doctor of Philosophy

Colorado State University

Fort Collins, Colorado

Fall 2006

Reproduced with permission of the copyright owner. Further reproduction prohibited without permission.

UMI Number: 3246310

INFORMATION TO USERS

The quality of this reproduction is dependent upon the quality of the copy submitted. Broken or indistinct print, colored or poor quality illustrations and photographs, print bleed-through, substandard margins, and improper alignment can adversely affect reproduction.

In the unlikely event that the author did not send a complete manuscript and there are missing pages, these will be noted. Also, if unauthorized copyright material had to be removed, a note will indicate the deletion.

UMI®

UMI Microform 3246310

Copyright 2007 by ProQuest Information and Learning Company.

All rights reserved. This microform edition is protected against unauthorized copying under Title 17, United States Code.

ProQuest Information and Learning Company
300 North Zeeb Road
P.O. Box 1346
Ann Arbor, MI 48106-1346

Reproduced with permission of the copyright owner. Further reproduction prohibited without permission.

COLORADO STATE UNIVERSITY

August 14, 2006

WE HEREBY RECOMMEND THAT THE DISSERTATION PREPARED UNDER OUR SUPERVISION BY Erica Lynn Snow ENTITLED SPECTROSCOPY OF HIGH ANGULAR MOMENTUM RYDBERG STATES WITH $^2S_{1/2}$ ION CORES BE ACCEPTED AS FULFILLING IN PART REQUIREMENTS FOR THE DEGREE OF DOCTOR OF PHILOSOPHY.

Committee on Graduate Work

Adviser

Department Head

Reproduced with permission of the copyright owner. Further reproduction prohibited without permission.

ABSTRACT OF DISSERTATION

SPECTROSCOPY OF HIGH ANGULAR MOMENTUM RYDBERG STATES

WITH $^2S_{1/2}$ ION CORES

The fine structure intervals of n=17 and 20 have been measured in magnesium and barium for a range, $7 \leqslant L \leqslant 13$, of angular momentum states. This systematic study used microwave spectroscopy with selective laser excitation for detection of Rydberg levels by Stark ionization. These precise measurements lead to up to two orders of magnitude improvement from past experimental determinations of the induced polarizabilities of the ground state ionic cores. The measured polarizabilities are, for Mg^+, $\alpha_d = 35.02(4)a_0^3$ and $\alpha_Q = 202(54)a_0^5$, and for Ba^+, $\alpha_d = 124.09(27)a_0^3$ and $\alpha_Q = 4238(643)a_0^5$.

An opportunity to test the adequacy of the long-range model, historically used to treat high-angular momentum fine structure data, is possible with the availability of independent theoretical calculations. Previously, studies have revealed excellent agreement with calculated values of the induced dipole polarizability of the ion core. A large discrepancy is found, however, between experiment and the best theoretical calculations for the induced quadrupole polarizability. These previous disagreements between theory and experiment for $^2S_{1/2}$ systems have been largely resolved in this work. In addition, the inclusion of core fine structure in the long-range model will be shown to describe the spin-orbit splittings of high-L barium states.

Erica Lynn Snow
Physics Department
Colorado State University
Fort Collins, CO 80523
Fall 2006

Reproduced with permission of the copyright owner. Further reproduction prohibited without permission.

Table of Contents

Reproduced with permission of the copyright owner. Further reproduction prohibited without permission.

List of Tables

Reproduced with permission of the copyright owner. Further reproduction prohibited without permission.

Reproduced with permission of the copyright owner. Further reproduction prohibited without permission.

List of Figures

Reproduced with permission of the copyright owner. Further reproduction prohibited without permission.

Reproduced with permission of the copyright owner. Further reproduction prohibited without permission.

Reproduced with permission of the copyright owner. Further reproduction prohibited without permission.

Introduction

An electron that is in a highly excited state, which is weakly bound to the positive ion core which makes up the rest of the system, is classified as a Rydberg state. Within the class of Rydberg states are those with high angular momentum. As angular momentum increases the centrifugal barrier will block the Rydberg electron from approaching small radii. This centrifugal barrier determines the classical inner turning point of radial motion for hydrogenic states, given by

$$r_- = n^2 a_0 - n^2 a_0 \sqrt{1 - \frac{L(L+1)}{n^2}} \simeq \frac{L(L+1)a_0}{2}\left[1 + \frac{L(L+1)}{4n^2} + \cdots\right], \quad (1)$$

where a_0 is the Bohr radius (0.0529 nm). Therefore, electrons of angular momentum, L, will have an inner turning point greater than $L(L+1)a_0/2$. Angular momentum states where the inner turning point is greater than the largest radial coordinate of the ion core are considered to be non-penetrating, "high-L", Rydberg states. For Rydberg states of sufficiently high L, typically $L \geq 5$, these systems can be approximated as a hydrogenic electron bound to a positive point charge. The interactions present in addition to this dominant Coulomb interaction are weak and exclusively long-range.

The small energy deviations from hydrogenic energies among high-L Rydberg levels create a unique pattern, which is referred to as the fine structure. The fine

Reproduced with permission of the copyright owner. Further reproduction prohibited without permission.

structure is a result of the fact that the ion core is not a point charge. It is instead a collection of electrons surrounding the nucleus which can possess permanent multipole moments or acquire induced moments in the presence of an electric field. The Rydberg electron presents such an electric field. It is known by the Virial Theorem that the Rydberg electron in its large nearly circular orbit is moving much more slowly than the tightly bound ion core electrons. Thus the electric field produced by this nearly stationary point charge can induce an electric dipole moment within the ion core. This increases the Rydberg electron's binding energy by

$$\Delta E = -\frac{1}{2}\vec{p}\cdot\vec{E} = -\frac{1}{2}\alpha_d\vec{E}\cdot\vec{E} = -\frac{1}{2}\alpha_d\left(\frac{e}{r^2}\right)^2 \tag{2}$$

where $\vec{p}$ is the induced dipole moment, $\vec{E}$ is the electric field due to the Rydberg electron, and α is the dipole polarizability. The average squared electric field exerted on the core by the Rydberg electron, $\langle e^2/r^4\rangle$, varies with the angular momentum of the Rydberg electron, producing the characteristic fine structure pattern. Therefore it is possible to use measurements of the fine structure pattern to deduce these polarizabilities, which are properties characteristic of the ion core [1]. Using the high-L Rydberg electron as a sensitive probe of the ion core was first proposed separately by Mayer and Mayer [2] and Van Vleck and Whitelaw [3].

The fine structure pattern can also be predicted by use of Rayleigh-Schrödinger perturbation theory in a quantum mechanical treatment. Higher order multipole terms can also be included to account for induced moments beyond that of the dipole. However, the first terms are most significant. Ignoring the small energies associated with the motion of the Rydberg electron leads to the adiabatic approximation, which

Reproduced with permission of the copyright owner. Further reproduction prohibited without permission.

leads directly to Eq. (2) and higher multipole contributions. By use of an adiabatic expansion, a series of correction terms can also be included which depend on the Rydberg energies. These non-adiabatic correction terms can be thought of as the result of the Rydberg electron not being exactly stationary and the finite time it takes the ion core to adjust to the Rydberg electron's motion. An elegant presentation of this long-range polarization model was developed in detail for the case of helium by Drachman [4].

Experimental investigation of Rydberg fine structure patterns was limited for years because of the lack of access to states of sufficiently high-L. Some of the first studies were able to reach up to $L \geq 5$ by use of grating spectrometers [5, 6] and then by Fourier Transform Spectrometers (FTS) [7, 8, 9] or by identification of solar spectrum emission lines [10, 11]. Stepwise laser excitation followed by microwave induced transitions presented a more efficient way to observe high-L states [12, 13, 14].

Some of these previous studies have investigated Rydberg state of magnesium and barium, the two atoms studied here [11, 13, 15]. Although these works contain precise measurements, they do not access states with $L > 5$. The precision obtained from these studies was limited to about 1% for the dipole polarizability. Little information on the polarizability was extracted. Gallagher's studies of barium pointed out large non-adiabatic effects due to the lowest ion core excited states of Ba^+.

More general access to a wide range of high-L Rydberg states has become possible through the technique of Resonant Excitation Stark Ionization Spectroscopy, here referred to as RESIS. This technique utilizes a fast Rydberg beam produced by single electron capture into high-L Rydberg states by a collision between an accelerated ion

Reproduced with permission of the copyright owner. Further reproduction prohibited without permission.

beam with a Rydberg target. Detection of particular Rydberg states is by upward excitation with a Doppler-tuned CO_2 laser. A microwave interaction region can be used to drive transitions of $\Delta L = \pm 1,2$, and 3 within a principal quantum state. A CO_2 laser transition before the microwave region saturates a transition between a low and high n Rydberg level, typically n=9, L and n=17, $L+1$, equalizing the population. Then a second CO_2 laser after the microwave region saturates the optical transition again resulting in a larger upper state population only if a microwave transition has occurred. The RESIS technique has been used to precisely explore the electric and magnetic fine structure of several atoms, molecules and ions [16, 17, 18, 19, 20]. In this work the RESIS optical and microwave techniques are implemented to take measurements of n=17 and 20, $7 \leq L \leq 11$, Rydberg states of magnesium and barium.

As mentioned above the polarization model has been successfully applied to many systems. Measured fine structure intervals normalized to $\Delta \langle r^{-4} \rangle$ are plotted versus $\Delta \langle r^{-6} \rangle / \Delta \langle r^{-4} \rangle$ and a subsequent linear fit to this pattern gives an intercept and slope, which correspond to one half the dipole polarizability and the coefficient of the $\Delta \langle r^{-6} \rangle$ term respectively. It has often been found that the agreement with theoretical calculations is good for the extracted dipole polarizability, or intercept, but in poor agreement for the slope of the polarization plot [21]. This can be illustrated by recent measurements in several different $^2S_{1/2}$ systems. For example, in silicon III, the extracted dipole polarizability is in perfect agreement with theory, but the quoted slope of -14.6(1.6) is in serious disagreement with -27.4, the best theoretical calculation [19, 22]. A study of magnesium by Lyons and Gallagher reported $33.8(5)a_0^3$ for a dipole polarizability and a slope of -124(4) [15]. This is only two standard

Reproduced with permission of the copyright owner. Further reproduction prohibited without permission.

deviations away from the calculated dipole polarizability of $35.01a_0^3$, but the slope, predicted to be -240, is a factor of two different [22]. A similar situation is found in the case of barium. Experimentally, a dipole polarizability of $124.30(16)a_0^3$ is found with a slope of -518(170), and the theoretical calculations find $124.7(2.5)a_0^3$ and 279 respectively [23]. In each case, the theoretical calculations are made with relativistic many body perturbation theory, similar to that used to obtain the precise calculations needed for the interpretation of parity non-conservation experiments in cesium [22]. These calculations give theoretical values for the ion core matrix elements, which are listed in Appendix C with the calculated polarizabilities. It seems unlikely that these consistent discrepancies are entirely due to errors in the calculated core properties. The comparisons between experiment and theory are summarized in Table 1. This series of discrepancies is the main motivating factor behind this work. An in depth look at the polarization model is performed here, investigating this disagreement, and new data is obtained for the cases of magnesium and barium. It is hoped that either the new data or some new theoretical development will resolve these discrepancies.

Table 1: Experimental values from fitted polarization plots are given in columns 2 and 4 [15, 20, 23]. The calculated values determined by use of matrix elements from relativistic many-body theory (See Appendix C) is listed in columns 3 and 5 [22]. The intercept is one half the dipole polarizability and the slope involves the quadrupole polarizability and a correction to the adiabatic dipole polarizability. Note the disagreement in the slope is severe.

	exp. intercept	theory intercept	exp. slope	theory slope
Si^{3+}	3.702(6)	3.7	-14.6(1.6)	-27.4
Mg^{+}	16.9(3)	17.505	-124(4)	-240
Ba^{+}	62.15(8)	62.4(1.2)	-518(170)	279(77)

Reproduced with permission of the copyright owner. Further reproduction prohibited without permission.

The Ba^+ ion is one of the most interesting ions whose properties could be studied with this method. Knowledge of the quadrupole transition matrix element between the Ba^+ 6S and 5D states is critical to proposed parity non-conservation experiments. The alkali-metal atoms, Cs and Fr, and the alkali-like ions, Ba^+ and Ra^+, are among the best candidates for precise atomic tests of parity violating weak interactions. The most successful measurements to date have been carried out in Cs [24], but measurements are being actively pursued in Fr [25] and Ba^+ [26]. Achieving a precise test of standard model predictions requires both precise experimental measurements and a reliable understanding of the atomic structure matrix elements that connect the measured quantities to fundamental interaction strengths. In Cs, a comparison of measurements and calculations of a number of related atomic properties have been examined to estimate the precision of the matrix elements. In that case, the precision of the calculations appears to be about 0.4 percent, and is the limiting factor in comparing PNC measurements to standard model predictions [24]. Among the atomic properties which can be compared with calculations at this level of precision are excited state lifetimes, hyperfine constants, and polarizabilities or Stark shift rates. In Ba^+, although calculations have been carried out with similar care [27], there are far fewer precise experimental tests. For example, the lifetime of both 6P and both 5D states in Ba^+ has been measured only to a precision of about 1.3% and 6% respectively. [28, 29, 30, 31]. More recently, Sherman, et al. have measured the off-resonant vector ac Stark effect (or light shift) in the $6S_{1/2}$ and $5D_{3/2}$ states to 0.1% precision [32]. A precise measurement of the ground state polarizability of Ba^+ by means of spectroscopy of Rydberg states of barium would be a significant

Reproduced with permission of the copyright owner. Further reproduction prohibited without permission.

additional test of the theory of this interesting ion. Obtaining the polarizability from measurements of the barium fine structure pattern requires high confidence in the polarization model.

This study is organized into chapters where the theoretical model is developed, the experimental techniques are described, and the data is presented followed by a critical discussion. Chapter 1 begins with a review of the long-range polarization model, but is extended to systems larger than helium that have $^2S_{1/2}$ ion cores. This model is revisited in order to include for the first time the spin of the core electron. A discussion is presented investigating the applicability of this model to helium and similar systems. Chapter 2 lays out the apparatus and experimental techniques utilized in this study. Contained in Chapter 3 are the measurements of magnesium and barium. Chapter 4 will present the data treated with the long-range model and a critical comparison with the existing independent theoretical calculations.

Reproduced with permission of the copyright owner. Further reproduction prohibited without permission.

Chapter 1

Theoretical Model

The polarization model is an expression for the binding energy of high angular momentum Rydberg levels, characterizing the ion core with a small set of properties. The model gives the energy as the difference in the binding energy from hydrogenic energies. It describes the difference from hydrogenic atoms or ions with an expectation value of an effective potential. The effective potential consists of terms with increasing negative powers of the radial coordinate of the Rydberg electron.

The polarization model has effectively described high-l Rydberg states of helium. The most complete theoretical development was presented by Drachman, in which all terms proportional to $\langle r^{-s} \rangle$ for $s \leq 10$ are included with their coefficients calculated analytically [4]. Similar models have been employed to describe measured Rydberg fine structures in other atomic, molecular and ionic systems [17, 18, 19, 20, 23, 33]. However, there has been little explicit theoretical work added to extend and improve the foundation of the polarization model. Some of the more recent theoretical work has been focused on developing a framework for describing Rydberg states with

Reproduced with permission of the copyright owner. Further reproduction prohibited without permission.

anisotropic core ions, such as neon with a $^2P_{3/2}$ ion core state. [17, 34, 35] This work, in contrast, studies application of the polarization model to $^2S_{1/2}$ state ion cores of increasing size. Because of the similarity to the $^2S_{1/2}$ ion core of helium Rydberg states, we refer here to these atoms as "helium-like".

This chapter will present a discussion of the simple model and the extensions made to it in order to adapt to larger systems. The first section describes the simple polarization model. These calculations exclude any contribution of electron spin. The second section revisits the model, but is now generalized to include core spin. The reason for developing this original addition is that the spin-orbit interactions in the core grow increasingly significant as the number of electrons in the core increases. While the effects of core spin-orbit splittings may be insignificant in helium, they turn out to play a very significant role in heavier "helium-like" Rydberg systems. The third section describes the use of the theoretical model to analyze experimental data, and discusses some of its limitations.

This work will be limited to "helium-like" Rydberg systems with $^2S_{1/2}$ ion cores, in which the Rydberg electron is bound to a positive ion consisting of a closed shell of ions with one additional $^2S_{1/2}$ valence electron. The high-L Rydberg system can be described as having two major parts; the ion core and the Rydberg electron, shown schematically in Fig. 1.1. The Rydberg electron is in a high angular momentum state, which means it is prevented by the centrifugal barrier from approaching the core ion. This justifies the two major assumptions in the long-range model:

(1) The Rydberg electron is distinguishable from all the other core electrons.

Reproduced with permission of the copyright owner. Further reproduction prohibited without permission.

Therefore, exchange can be ignored so that the wavefunction of the multi-electron atom does not need to be fully anti-symmetrized.

(2) The Rydberg electron is always a greater distance from the nucleus than any of the core electrons. Core penetration is a negligible effect, which further simplifies the model.

This leads to the conclusion that the polarization of the core is the only major contribution to the quantum defect of the Rydberg electron energy.

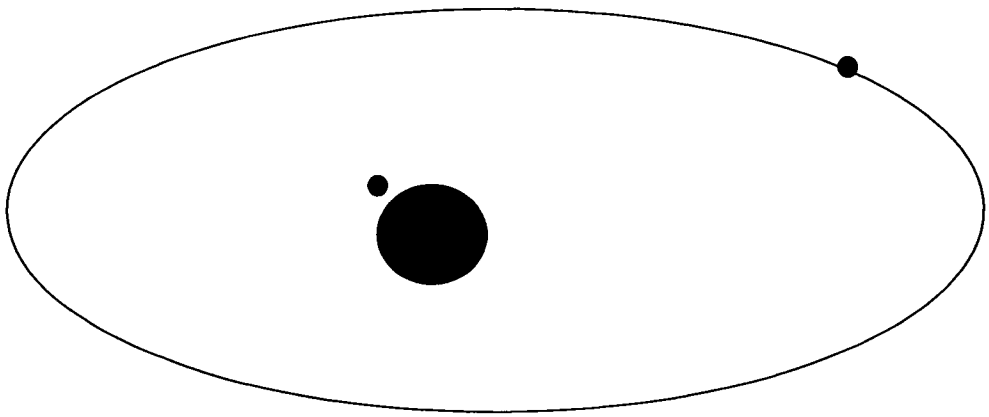

Figure 1.1: The $^2S_{1/2}$ system for a high angular momentum Rydberg state consists of the ion core, shown here depicting the nucleus as a closed shell of electrons and one more valence electron in an S orbital. The remaining electron is the Rydberg electron, which is in a non-penetrating orbit around the ion core.

1.1 Long-Range Polarization Model

For simplicity, all electron spins are ignored in the simple polarization model described here as in several publications [4, 36]. The non-relativistic Hamiltonian for these

Reproduced with permission of the copyright owner. Further reproduction prohibited without permission.

Rydberg states is

$$
\begin{aligned}
H &= H_0 + V, \\
H_0 &= \left[\sum_{i=1}^{N-1}\left(\frac{|\overrightarrow{p_i}|^2}{2} - \frac{Z}{r_i}\right) + \sum_{\substack{i=1 \\ j>i}}^{N-1}\frac{1}{r_{ij}}\right] + \left[\frac{|\overrightarrow{p_{Ryd}}|^2}{2} - \frac{Q}{r_{Ryd}}\right], \\
V &= \sum_{i=1}^{N-1}\frac{1}{r_{iRyd}} - \frac{(N-1)}{r_{Ryd}} = \sum_{i=1}^{N-1}\sum_{k=1}^{\infty}\frac{r_i^k}{r_{Ryd}^{k+1}}C^k(\Omega_i)\cdot C^k(\Omega_{Ryd}),
\end{aligned} \tag{1.1}
$$

where Z is the nuclear charge, N is the total number of electrons, Q=Z-N+1 is the charge of the ion core, r_i and r_{Ryd} are the radial positions of the core electrons and the Rydberg electron respectively, and Ω denotes the angular coordinates. Simply put, H_0, describes the energy of a free ion and a hydrogenic Rydberg electron. The remaining part of the Hamiltonian, V, is expected to produce only small deviations from this picture. It is conveniently represented, as in Eq.(1.1), by the multipole expansion where the lowest term is the dipole term.

It is straight forward to determine the energy of the Rydberg electron through the use of perturbation theory, where

$$
\begin{aligned}
E &= E^{[0]} + E^{[1]} + E^{[2]} + E^{[3]} + \cdots \\
E^{[1]} &= <\Psi^0|V|\Psi^0> \\
E^{[2]} &= \sum_{\Psi'^0 \neq \Psi^0}\frac{<\Psi^0|V|\Psi'^0><\Psi'^0|V|\Psi^0>}{E_\Psi - E_{\Psi'}} \\
E^{[3]} &= \sum_{\Psi'^0,\Psi''^0 \neq \Psi^0}\frac{<\Psi^0|V|\Psi'^0><\Psi'^0|V|\Psi''^0><\Psi''^0|V|\Psi^0>}{(E_\Psi - E_{\Psi'})(E_\Psi - E_{\Psi''})} \\
&\quad - <\Psi^0|V|\Psi^0>\sum_{\Psi'^0,\Psi''^0 \neq \Psi^0}\frac{<\Psi^0|V|\Psi'^0><\Psi'^0|V|\Psi^0>}{(E_\Psi - E_{\Psi'})^2}.
\end{aligned} \tag{1.2}
$$

The zeroth order wavefunction is the product of the free ion core and hydrogenic

Reproduced with permission of the copyright owner. Further reproduction prohibited without permission.

Rydberg functions resulting from H_0,

$$\Psi^0 = \Psi^0_{Core} \otimes \Psi^0_{nl} \equiv |g, nl; L>, \tag{1.3}$$

where "g" denotes the $^2S_{1/2}$ ground state of the ion core. The zeroeth order energy is,

$$E^{[0]} = E_{Core} - \frac{Q^2}{2n^2}. \tag{1.4}$$

Here, as below, energies are expressed in atomic units, $\frac{e^2}{a_0} \approx 27.2eV$.

For helium-like systems with $^2S_{1/2}$-state cores the core is isotropic. The first order energy, $E^{[1]}$, vanishes in the integral over the core's angular coordinates. The first non-zero contribution comes from the second order energy, or induced multipole moments. The perturbation, V, separates the energy into a series of contributions from each multipole order of the expansion. Since each term in V is a scalar, only intermediate states with $L_{Tot} = L$ are allowed, where $\vec{L}_{Tot} = \vec{L}_C + \vec{L}_{Ryd}$ The energy denominator can be separated into two parts; ΔE_{Core}, the difference in energy between the core ground state and core excited states, and ΔE_{Ryd}, the difference in energy of the Rydberg electron. The second order energy can be written explicitly as,

$$E^{[2]}(g, nL) = -\sum_{\substack{k, n_C, l_C \\ , n', l'}} \frac{\left| \left\langle g, (n, L) \left| \frac{\sum_{i=1}^{N-1} r_i^k C^k(\Omega_i) \cdot C^k(\Omega_{Ryd})}{r_{Ryd}^{k+1}} \right| (n_C, l_C), (n', l') \right\rangle \right|^2}{\Delta E_{Core} + \Delta E_{Ryd}}, \tag{1.5}$$

where

$$\begin{aligned} \Delta E_{Core} &= E(n_C, l_C) - E(g), \\ \Delta E_{Ryd} &= E(n', l') - E(n, L). \end{aligned} \tag{1.6}$$

Here g is the notation used to indicate the ion core's ground state, $3^2S_{1/2}$ for magnesium and $6^2S_{1/2}$ for barium. Since only the difference in core ion energies occurs in

Reproduced with permission of the copyright owner. Further reproduction prohibited without permission.

Eq.(1.6), the ground state energy will be designated as zero so $\Delta E_{Core} \equiv E(n_C l_C)$. The sum includes both discrete states and those in the continuum. Similar expressions are given with slightly different notation in Refs. [4, 34, 35, 36]. The angular part can be separated and easily evaluated by methods given in Edmonds [37]. The scalar product of two commuting tensor operators gives

$$\left|\left\langle g,(nL)\left|\frac{\sum_{i=1}^{N-1} r_i^k C^k(\Omega_i)\cdot C^k(\Omega_{Ryd})}{r_{Ryd}^{k+1}}\right|(n_C l_C),(n'l')\right\rangle\right|^2 =$$
$$\left\{\begin{array}{ccc} L & L & 0 \\ k & 1 & l' \end{array}\right\}^2 \left|\left\langle g\|\sum_{i=1}^{N-1} r_i^k C^k(\Omega_i)\|n_C l_C\right\rangle\langle nL\|C^k(\Omega_{Ryd})\|n'l'\rangle\right|^2$$
$$\left|\left\langle nL\left|r_{Ryd}^{-(k+1)}\right|n'l'\right\rangle\right|^2, \tag{1.7}$$

Two of the factors in Eq.(1.7) can be condensed in the definition:

$$\begin{aligned} A(k,l_C,l'_C,L,l') &\equiv \left\{\begin{array}{ccc} L & L & l_C \\ k & l'_C & l' \end{array}\right\} \left|\langle nL\|C^k(\Omega_{Ryd})\|n'l'\rangle\right| \\ &= (-1)^l\sqrt{(2L+1)(2l'+1)(2k+1)} \\ &\quad\times\left\{\begin{array}{ccc} L & L & l_C \\ k & l'_C & l' \end{array}\right\}\left(\begin{array}{ccc} L & k & l' \\ 0 & 0 & 0 \end{array}\right). \end{aligned} \tag{1.8}$$

At this point, explicit evaluation of the second order energy becomes difficult due to the calculation of the sum of the matrix elements and the energy denominator. The energy denominator can be formally expanded in a power series expansion in the ratio of the Rydberg to core energy differences,

$$\frac{1}{E(n_C l_C)+\Delta E_{Ryd}} \sim \frac{1}{E(n_C l_C)}\left(1-\frac{\Delta E_{Ryd}}{E(n_C l_C)}+\left(\frac{\Delta E_{Ryd}}{E(n_C l_C)}\right)^2+\cdots\right), \tag{1.9}$$

This expansion is referred to as the "adiabatic expansion". The adiabatic expansion requires one additional assumption; the Rydberg energy difference must be smaller

Reproduced with permission of the copyright owner. Further reproduction prohibited without permission.

than the core energy difference. This allows the following grouping of terms,

$$
\begin{aligned}
E^{[2]} \quad = & -\sum_{\substack{k,n_C,l_C \\ n',l'}} A(k,0,l_C,L,l')^2 \frac{\left\langle g\| \sum_{i=1}^{N-1} r_i^k C^k(\Omega_i) \| n_C l_C \right\rangle^2}{E(n_C l_C)} \left\langle nL \left| r^{-(k+1)} \right| n'l' \right\rangle^2 \\
& + \sum_{\substack{k,n_C,l_C \\ n',l'}} A(k,0,l_C,L,l')^2 \frac{\left\langle g\| \sum_{i=1}^{N-1} r_i^k C^k(\Omega_i) \| n_C l_C \right\rangle^2}{E(n_C l_C)^2} \Delta E_{Ryd} \left\langle nL \left| r^{-(k+1)} \right| n'l' \right\rangle^2 \\
& - \sum_{\substack{k,n_C,l_C \\ n',l'}} A(k,0,l_C,L,l')^2 \frac{\left\langle g\| \sum_{i=1}^{N-1} r_i^k C^k(\Omega_i) \| n_C l_C \right\rangle^2}{E(n_C l_C)^3} \Delta E_{Ryd}^2 \left\langle nL \left| r^{-(k+1)} \right| n'l' \right\rangle^2 \\
& + \cdots
\end{aligned} \tag{1.10}
$$

The first term is the adiabatic term, the second and third terms are the first and second of a series of non-adiabatic correction terms. Within each of these terms is another series of terms from the multipole expansion. Now that the energy denominator can be pulled outside the summation over n', the expression of the second order energy can be simplified further. It is not difficult to show, using the the completeness of Rydberg radial wave functions of fixed l' that

$$
\sum_{n'} \left| \langle n', l' \left| r^a \right| n, l \rangle \right|^2 = \left\langle r^{2a} \right\rangle_{nl}, \tag{1.11}
$$

and that the following is a simplified way of writing the adiabatic portion of the second order energy,

$$
E_{Ad}^{[2]} = -\frac{1}{2}\alpha_d \left\langle r^{-4} \right\rangle - \frac{1}{2}\alpha_Q \left\langle r^{-6} \right\rangle + \cdots \tag{1.12}
$$

where,

$$
\begin{aligned}
\alpha_d &= \frac{2}{3} \sum_{n_C} \frac{\left\langle g\| \bar{D} \| n_C, P \right\rangle^2}{E(n_C P)} \\
\alpha_Q &= \frac{2}{5} \sum_{n_C} \frac{\left\langle g\| \bar{Q} \| n_C, D \right\rangle^2}{E(n_C D)},
\end{aligned} \tag{1.13}
$$

Reproduced with permission of the copyright owner. Further reproduction prohibited without permission.

and

$$\bar{D} \equiv \sum_{i=1}^{N-1} r_i C^1(\Omega_i) \tag{1.14}$$

$$\bar{Q} \equiv \sum_{i=1}^{N-1} r_i^2 C^2(\Omega_i). \tag{1.15}$$

In a similar fashion, the sum over products of the squared Rydberg matrix element and the Rydberg energy difference can be reduced. The radial wave equation satisfied by the Rydberg radial wave function can be substituted in and then integration by parts reduces the product to a form where the completeness of the radial wave function can be applied. These steps lead to the following relation,

$$\sum_{n'} \left|\langle n', l' \left| r^{-s} \right| n, l \rangle\right|^2 (E(n') - E(n)) = \frac{1}{2}\left[(s^2 - l(l+1) + l'(l'+1)\right] \left\langle r^{-2s-2)} \right\rangle_{nl}. \tag{1.16}$$

With this simple relation it can be easily seen that the first non-adiabatic energy can be written as,

$$E_{1NA}^{[2]} = 3\beta_d \left\langle r^{-6} \right\rangle + \frac{15}{2}\beta_Q \left\langle r^{-8} \right\rangle + \cdots \tag{1.17}$$

where

$$\begin{aligned} \beta_d &= \frac{1}{3}\sum_{n_C} \frac{\langle g \| \bar{D} \| n_C, P \rangle^2}{E(n_C P)^2} \\ \beta_Q &= \frac{1}{5}\sum_{n_C} \frac{\langle g \| \bar{Q} \| n_C, D \rangle^2}{E(n_C D)^2}. \end{aligned} \tag{1.18}$$

The appearance of a sequence of terms with increasing negative powers of r_{Ryd} is characteristic of the polarization model. Higher negative powers decrease more rapidly with L, therefore the leading terms are dominant for high-L systems. All significant terms up to r^{-8} will be treated in this work. This includes terms in the polarization

Reproduced with permission of the copyright owner. Further reproduction prohibited without permission.

energy that scale with $\langle r^{-7} \rangle$ and $L(L+1)\langle r^{-8} \rangle$. These contributions result from the first terms in the 3rd order perturbation and from the 2nd non-adiabatic correction to the dipole term.

The significance of these additional terms can be illustrated by looking at a scaled plot identical to the polarization plots used in previous studies. The polarization plot consists of the energy intervals normalized to $\Delta\langle r^{-4} \rangle$ and plotted versus $\Delta\langle r^{-6} \rangle / \Delta\langle r^{-4} \rangle$. It is usually assumed that higher terms proportional to $\langle r^{-7} \rangle$, $L(L+1)\langle r^{-8} \rangle$, or $\langle r^{-8} \rangle$ would not contribute to the slope of such a plot near x=0, but only introduce some curvature. Shown in Fig. 1.2 are the scaled differences in the $\Delta\langle r^{-7} \rangle$, $\Delta[L(L+1)\langle r^{-8} \rangle]$ and $\Delta\langle r^{-8} \rangle$ for several values of transitions from L to $L+1$. The plotted points correspond to states similar to those in this study, n=20 starting with $L = 7$ to $L = 8$ transition at the far right of the plot up to the $L = 13$ to $L = 14$ transition near x=0. By inspection of this plot it can be seen that even for high-L states the contribution from $\Delta\langle r^{-7} \rangle$ and $\Delta[L(L+1)\langle r^{-8} \rangle]$ may significantly affect the slope of the polarization plot. A simple linear fit to these three sets of points, $L(L+1)\langle r^{-8} \rangle$, $\langle r^{-7} \rangle$, and $\langle r^{-8} \rangle$ in fig. 1.2 gives a crude estimate of the expected change in slope of 0.087(7), 0.041(3), and 0.0016(2) due to a unit value of each of the terms respectively. The effect on the slope, however, is a matter of degree due to the magnitude of the coefficient attached to these terms. The coefficients of these terms depend on the inverse of the core excited energy squared and cubed. This will cause these terms to become increasingly significant for larger systems where the core excited energies are small, such as in barium. Contributions proportional to $\Delta\langle r^{-8} \rangle$ do not seem to affect the initial slope significantly, since it is an order of magnitude

Reproduced with permission of the copyright owner. Further reproduction prohibited without permission.

smaller than the other two terms. Evaluation of the coefficients for the first two terms will be performed in order to determine the significance with respect to the slope.

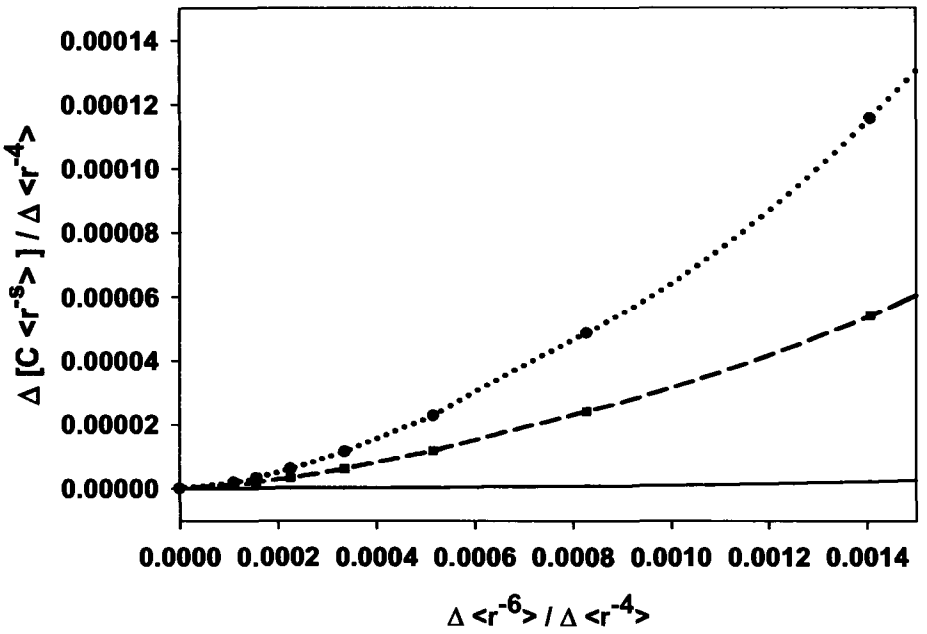

Figure 1.2: The scaled contributions of the $\Delta \langle r^{-7} \rangle$ (dashed line), $\Delta[L(L+1) \langle r^{-8} \rangle]$ (dotted line) and $\Delta \langle r^{-8} \rangle$ (solid line) are plotted versus $\Delta \langle r^{-6} \rangle / \Delta \langle r^{-4} \rangle$ for n=20 L to $L+1$ transitions with $7 \leq L \leq 13$, where the L=7 to 8 transition is at 0.0014 and the transitions of progressively higher L approach zero. This illustrates the contribution of the higher order terms to the slope of a polarization plot.

The derivation of these remaining terms is straight forward and is simply an extension to the work presented above regarding the simple polarization model. The third order in the Rayleigh-Schrödinger perturbation is given in Eq.(1.2). The lowest multipole terms are the largest contribution to the polarization energy. As performed above an adiabatic expansion is taken with the first term, the adiabatic contribution, as the one of interest. The angular factor can be calculated for each of the possible transitions above. By use of completeness of the radial wavefunction, Eq.(1.11), the

Reproduced with permission of the copyright owner. Further reproduction prohibited without permission.

adiabatic 3rd order energy can be written as,

$$E_{Ad}^{[3]} = (-1)^{L+1}2 \sum_{\substack{n_C,n'_C \\ l',l''}} \left[\frac{< g\|\bar{D}\|n_C P >< n_C P\|\bar{D}\|n'_C D >< n'_C D\|\bar{Q}\|g >}{E(n_C P)E(n'_C D)} \right.$$
$$\left. \times A(1,0,1,L,l')A(1,1,2,l',l'')A(2,2,0,l'',L) \right] < r^{-7} >_{nL}$$
$$+(-1)^{L} \sum_{\substack{n_C,n'_C \\ l',l''}} \left[\frac{< g\|\bar{D}\|n_C P >< n_C P\|\bar{Q}\|n'_C P >< n'_C P\|\bar{D}\|g >}{E(n_C P)^2} \right.$$
$$\left. \times A(1,0,1,L,l')A(2,1,1,l',l'')A(1,1,0,l'',L) \right] < r^{-7} >_{nL} . \qquad (1.19)$$

Carrying out the sum over l' and l'' leads to the following,

$$E_{Ad}^{[3]} = \frac{2\sqrt{2}}{15} \langle r^{-7} \rangle \sum_{n_C,n'_C} \frac{< g\|\bar{D}\|n_C P >< n_C P\|\bar{D}\|n'_C D >< n'_C D\|\bar{Q}\|g >}{E(n_C P)E(n'_C D)}$$
$$+\frac{\sqrt{30}}{45} \langle r^{-7} \rangle \sum_{n_C,n'_C} \frac{< g\|\bar{D}\|n_C P >< n_C P\|\bar{Q}\|n'_C P >< n'_C P\|\bar{D}\|g >}{E(n_C P)^2}, \qquad (1.20)$$

An estimate of the result can be obtained including only the lowest core excited P and D states. This is justified by the fact that the next excited states are considerably larger in energy thus reducing the significance through the magnitude of the energy denominator.

$$E_{Ad}^{[3]} \approx \frac{2\sqrt{2}}{15} \langle r^{-7} \rangle \frac{\langle g\|\bar{D}\|P \rangle \langle P\|\bar{D}\|D \rangle \langle D\|\bar{Q}\|g \rangle}{E(P)E(D)}$$
$$+\frac{\sqrt{30}}{45} \langle r^{-7} \rangle \frac{\langle g\|\bar{D}\|P \rangle \langle P\|\bar{Q}\|P \rangle \langle P\|\bar{D}\|g \rangle}{E(P)E(P)}, \qquad (1.21)$$

where $|P>$ and $|D>$ denote the lowest core excited states of these symmetries.

Additional terms proportional to r^{-7} and $L(L+1)r^{-8}$ occur in the second non-adiabatic correction to the dipole second order energy. The calculation of the 2nd non-adiabatic dipole term starts with the expansion of Eq.(1.10). The third term with

Reproduced with permission of the copyright owner. Further reproduction prohibited without permission.

k=1 is the 2nd non-adiabatic dipole term of interest here. Now the sum of the product of the square of the matrix element and the square of the Rydberg energy difference must be determined. Details of this calculation can be found in Appendix A. Using the radial wave equation satisfied by the Rydberg radial wavefunction, completeness of the radial wave function, and integration by parts, it can be shown that,

$$\begin{aligned}\sum_{n'} \left|\langle n', L' \left|r^{-s}\right| n, L\rangle\right|^2 \left(\frac{1}{n_2} - \frac{1}{n'^2}\right)^2 = \\ + \left[-s(s+1) - L(L+1) + L'(L'+1)\right]^2 \left(\frac{1}{Q}\right)^2 \left\langle r^{-2s-4}\right\rangle \\ + s(2s+3)\left[-s(s+1) - L(L+1) + L'(L'+1)\right] \left(\frac{1}{Q}\right)^2 \left\langle r^{-2s-4}\right\rangle \\ + 4(s+1)(2s+3)s^2 \left(\frac{1}{Q}\right)^2 \left\langle r^{-2s-4}\right\rangle \\ - 4s^2 \left(\frac{1}{Q}\right)^2 \left(-2Q\left\langle r^{-2s-3}\right\rangle + L(L+1)\left\langle r^{-2s-4}\right\rangle + \frac{Q^2}{n^2}\left\langle r^{-2s-2}\right\rangle\right),\end{aligned} \tag{1.22}$$

where again Q is the ion core charge, Q=Z-N+1. For the dipole term, where $s = 2$, the n^2 that appears in the expression can be re-written with a relation given by Drachman [4],

$$-\frac{Q^2}{n^2}\left\langle r^{-6}\right\rangle = -\frac{11Q}{5}\left\langle r^{-7}\right\rangle + \frac{3}{10}\left[(2L+1)^2 - 36\right]\left\langle r^{-8}\right\rangle. \tag{1.23}$$

Combining the above with the summation over the two possible l' states gives the 2nd order non-adiabatic dipole energy, neglecting terms proportional to $\langle r^{-8}\rangle$ without the factor $L(L+1)$, as follows,

$$E^{[2]}_{2ndNAD} = \sum_{n_C} \frac{\left|\langle g\|\bar{D}\|n_C P\rangle\right|^2}{E(n_C P)^3}\left[\frac{4Q}{15}\left\langle r^{-7}\right\rangle - 6\frac{L(L+1)}{10}\left\langle r^{-8}\right\rangle\right] + \cdots. \tag{1.24}$$

Reproduced with permission of the copyright owner. Further reproduction prohibited without permission.

Again, the coefficients can be estimated including only the lowest P state, giving

$$E^{[2]}_{2ndNAD} \approx \frac{4Q}{15}\langle r^{-7}\rangle \frac{\left|\langle g\|\bar{D}\|P\rangle\right|^2}{E(P)^3} - 6\frac{L(L+1)}{10}\langle r^{-8}\rangle \frac{\left|\langle g\|\bar{D}\|P\rangle\right|^2}{E(P)^3}. \quad (1.25)$$

Summarizing, the simple polarization model gives a correction to the zeroth order energy as given below, where only significant terms up to the order of $\langle r^{-8}\rangle$ are shown,

$$E = -\frac{1}{2}\alpha_d\langle r^{-4}\rangle - \frac{1}{2}(\alpha_Q - 6\beta_d)\langle r^{-6}\rangle + \left(\frac{1}{2}\delta + \frac{8}{5}\gamma\right)\langle r^{-7}\rangle - 36\gamma\left(\frac{L(L+1)}{10} + \cdots\right)\langle r^{-8}\rangle + \cdots \quad (1.26)$$

where Eq.(1.18) defines the previously mention coefficients, and now

$$\gamma = \frac{Q}{6}\sum_{n_C}\frac{\left|\langle g\|\bar{D}\|n_C P\rangle\right|^2}{E(n_C P)^3}$$

$$\delta = \frac{4\sqrt{2}}{15}\sum_{n_C,n'_C}\frac{\langle g\|\bar{D}\|n_C P\rangle\langle n_C P\|\bar{D}\|n'_C D\rangle\langle n'_C D\|\bar{Q}\|g\rangle}{E(n_C P)E(n'_C D)} + \frac{2\sqrt{30}}{45}\sum_{n_C,n'_C}\frac{\langle g\|\bar{D}\|n_C P\rangle\langle n_C P\|\bar{Q}\|n'_C P\rangle\langle n'_C P\|\bar{D}\|g\rangle}{E(n_C P)E(n'_C P)}. \quad (1.27)$$

Equation (1.26) is completely parallel to Drachman's Eq.(46) except that the terms of order r^{-8} are not included and the coefficients are defined in terms of core matrix elements and energies instead of being explicitly calculated [4].

1.2 Polarization Model with Core Electron Spin

Experimental studies of Rydberg states of high-L in helium, where exchange energies are negligible, shows slightly different energies for states with different orientations

Reproduced with permission of the copyright owner. Further reproduction prohibited without permission.

of spin. The splitting is referred to as the magnetic fine structure because it is due mostly to the interactions of the electron spin magnetic moments with the magnetic field produced by the motion of the Rydberg electron. Unlike the lower-L states where an isolated singlet state is accompanied by three closely spaced triplet states, the high-L states where exchange is negligible exhibit a splitting of four roughly equally spaced states. Two states are purely triplet states, $J = L \pm 1$. However the other two, $J = L$, are approximately odd and even superpositions of singlet and triplet states. The energy splittings in high-L states of helium are determined by the spin-orbit interactions and are well described by the approximate spin Hamiltonian,

$$H_{MFS} = \frac{\alpha^2}{2r^3}[\bar{L} \cdot \bar{S_R} - 2\bar{L} \cdot \bar{S_C}]. \tag{1.28}$$

The physical interpretation of this model is simply that the two electrons are acting as free magnets. They interact at a distance through the magnetic field created by the orbiting Rydberg electron and their respective magnetic moments. This results in the standard Dirac spin-orbit interaction for the Rydberg electron, but also includes a spin-orbit interaction from the stationary core electron of opposite sign and twice the size because it is not reduced by the Thomas precession. Figure 1.3 illustrates this four-fold spin structure. This pattern is characteristic of all high-L levels in helium and has been confirmed both by experiment and calculations [38]. The exclusion of spin in the case of the helium polarization model is justified by the small size and intuitive nature of these magnetic interactions.

The spin-orbit theory for helium was expected to apply also to other "helium-like" systems, since the spin magnetic moments are the same. However, a similar

Reproduced with permission of the copyright owner. Further reproduction prohibited without permission.

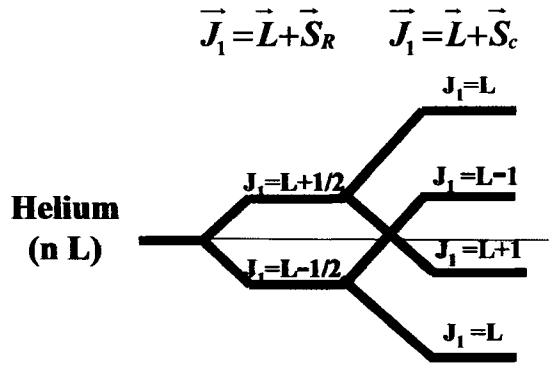

Figure 1.3: Each high-l level in helium is split into four approximately equally spaced levels by the magnetic interactions in the spin Hamiltonian. The two spin-orbit terms, which differ by a factor of -2 are responsible for the overall qualitative pattern.

structure of four roughly equally spaced spin levels was not observed in barium or in silicon III experiments [13, 19]. As first observed by Gallagher, et al. [13], there are doublet splittings in the barium fine structure pattern much larger than the predicted magnetic spin-orbit splittings. These splittings and other deviations from the expected magnetic spin structure observed in Si^{2+} were first explained as an indirect spin-orbit interaction of the core spin with the angular momentum of the Rydberg electron [39]. For systems with large polarizabilities the isotropic ion core deviates from its symmetry as a result of the electric field produced by the Rydberg electron. This electric field causes an admixture of multipole character into the wavefunction of the ion core. These virtual excitations of the $^2S_{1/2}$ ion core to states of higher angular momentum result in a non-zero contribution to the Rydberg energy from the spin-orbit interaction of the ion core angular momentum and the orientation of the core electron. This effect is dominated by the leading two terms from the lowest P and D excited states, which can be approximated by including them as a perturbation.

Reproduced with permission of the copyright owner. Further reproduction prohibited without permission.

The magnitude of the indirect spin-orbit effect is dependent on the polarizability, the energy difference between ground and excited states, and the fine structure splitting of the ion core electron. For this reason, the indirect spin-orbit splittings are large in barium, noticeable in silicon III, but of negligible size in helium. This indirect spin-orbit treatment indicates that these Rydberg spin splittings would be absent if the core fine structure energies were zero. The same conclusions were drawn by a similar calculation by Shuman et al. [40].

The importance of the ion core fine structure can be illustrated by examining the energies for the four systems of interest in this work. Table 1.1 lists the ion core energies and the fine structure splittings for the He^+, Mg^+, Si^{3+} and Ba^+ ions. The Ba^+ ratio of the fine structure splitting to the average core energy for the 5D state, is much larger than the other systems. It is unlikely for Ba^+ that ignoring the fine structure, especially in the 5D state, is a valid approximation. The best way to proceed would be to leave the dependence of the core electron spin in the calculations explicitly.

Table 1.1: Experimental values are given for the fine structure energy splittings in the lowest two excited states of the core and the average energy from the ground state. All energies listed are in atomic units [41].

	$\Delta E_{F.S.}(P)$	E(P)	$\Delta E_{F.S.}(P)/E(P)$	$\Delta E_{F.S.}(D)$	E(nD)	$\Delta E_{F.S.}(D)/E(D)$
He^+	2.67E10-5	1.50	1.78E-05	2.63E-06	1.778	1.48E-06
Si^{3+}	2.10E-03	0.326	6.44E-03	-5.42E-06	0.7307	7.42E-06
Mg^+	4.17E-04	0.163	2.56E-03	3.95E-06	0.3257	1.21E-05
Ba^+	7.70E-03	0.0975	8.00E-02	3.65E-03	0.02439	1.50E-01

In order to accurately model these $^2S_{1/2}$ systems of larger size the long-range polarization model must be expanded to include the spin of the core electron. Including

Reproduced with permission of the copyright owner. Further reproduction prohibited without permission.

the core spin means representing the ion core states in LS coupling notation. Although "LS notation" will be used for the ion core states, the assumption of pure LS coupling is not made in the following work. The Rydberg levels will now be written in the form $(^2S_{1/2}, nL : K)$, where $\bar{K} = \bar{J}_C + \bar{L}$. Consequently, the coupling of the core spin with the Rydberg electron's angular momentum gives two Rydberg levels for each value of L with $K = L \pm 1/2$. The only way in which magnetic interactions are included in the following calculation is that the core excitation energies implicitly include these interactions within the core. Magnetic interactions of the core and Rydberg electron are omitted, as are the Rydberg spin-orbit energies. Presumably, these small energies can still be modeled with Eq. (1.28).

Beginning again with the second and third order energies shown in Eq.(1.2). When the spin structure of the core electron is included the factoring of the scalar product of two commuting tensor operators gives a different angular factor as shown below,

$$B(k, j_C, j'_C, l, l', K) \equiv (-1)^{K+j'_C} \begin{Bmatrix} K & l & j_C \\ k & j'_C & l' \end{Bmatrix} \begin{pmatrix} l & k & l' \\ 0 & 0 & 0 \end{pmatrix}. \tag{1.29}$$

Now the second order energy can be written as follows,

$$E^{[2]} = - \sum_{\substack{k, n_C, l_C, j_C \\ n', l', K}} B(k, \frac{1}{2}, j_C, L, l', K)^2 \frac{\left\langle g \| \sum_{i=1}^{N-1} r_i^k C^k(\Omega_i) \| n_C l_C j_C \right\rangle^2}{(E(n_C l_C j_C) + \Delta E_{Ryd})} \left\langle nL \left| r^{-(k+1)} \right| n' l' \right\rangle^2 . \tag{1.30}$$

The adiabatic third order energy for only the lowest multipole term is given below

Reproduced with permission of the copyright owner. Further reproduction prohibited without permission.

in a similar fashion to that of Eq.(1.19) from the spinless case,

$$E_{Ad}^{[3]} = 2 \sum_{\substack{n_C,n'_C,j_C,j'_C \\ n',l',n'',l'',K}} \left[\frac{< g\|\bar{D}\|n_C P_{j_C} >< n_C P_{j_C}\|\bar{D}\|n'_C D_{j'_C} >< n'_C D_{j'_C}\|\bar{Q}\|g >}{E(n_C P_{j_C})E(n'_C D_{j'_C})} \right.$$
$$\left. \times B(1,\frac{1}{2},j_C,L,l',K)B(1,j_C,j'_C,l',l'',K)B(2,j'_C,\frac{1}{2},l'',L,K) \right] < r^{-7} >_{nL}$$
$$+ \sum_{\substack{n_C,n'_C,j_C,j'_C \\ n',l',n'',l'',K}} \left[\frac{< g\|\bar{D}\|n_C P_{j_C} >< n_C P_{j_C}\|\bar{Q}\|n'_C P_{j'_C} >< n'_C P_{j'_C}\|\bar{D}\|g >}{E(n_C P_{j_C})E(n_C P_{j'_C})} \right.$$
$$\left. \times B(1,\frac{1}{2},j_C,L,l',K)B(2,j_C,j'_C,l',l'',K)B(1,j'_C,\frac{1}{2},l'',L,K) \right] < r^{-7} >_{nL} . \tag{1.31}$$

The same process that was shown in the spinless case can be used again, but now the number of terms has greatly increased making this a much more tedious calculation. The relations given in Eqs.(1.11),(1.16),(1.22),and (1.23) are used again to further simplify the expression of the second order energy.

Summarizing the result, the center of gravity of the $K = L \pm 1/2$ states of common L gives an expression identical to that found in Section 1 including terms of interest up to order $< r^{-8} >$ as,

$$\begin{aligned} E &= -\frac{1}{2}\alpha_d \langle r^{-4} \rangle - \frac{1}{2}(\alpha_Q - 6\beta_d)\langle r^{-6} \rangle + \left(\frac{1}{2}\delta + \frac{8}{5}\gamma\right)\langle r^{-7} \rangle \\ &+ \left(-36\gamma\left(1 + \frac{L(L+1)}{10}\right) + \frac{15}{2}\beta_Q + \cdots\right)\langle r^{-8} \rangle + \cdots \end{aligned} \tag{1.32}$$

However, now the terms are defined as follows. The second order adiabatic coefficients are

$$\begin{aligned} \alpha_d &= \frac{1}{3}\sum_{n_C}\left[\frac{\langle g\|\bar{D}\|n_C P_{1/2}\rangle^2}{E(n_C P_{1/2})} + \frac{\langle g\|\bar{D}\|n_C P_{3/2}\rangle^2}{E(n_C P_{3/2})}\right] \\ \alpha_Q &= \frac{1}{5}\sum_{n_C}\left[\frac{\langle g\|\bar{Q}\|n_C D_{3/2}\rangle^2}{E(n_C D_{3/2})} + \frac{\langle g\|\bar{Q}\|n_C D_{5/2}\rangle^2}{E(n_C D_{5/2})}\right]. \end{aligned} \tag{1.33}$$

Reproduced with permission of the copyright owner. Further reproduction prohibited without permission.

The second order first non-adiabatic coefficients are

$$\begin{aligned}\beta_d &= \frac{1}{6}\sum_{n_C}\left[\frac{\langle g\|\bar{D}\|n_C P_{1/2}\rangle^2}{E(n_C P_{1/2})^2} + \frac{\langle g\|\bar{D}\|n_C P_{3/2}\rangle^2}{E(n_C P_{3/2})^2}\right] \\ \beta_Q &= \frac{1}{10}\sum_{n_C}\left[\frac{\langle g\|\bar{Q}\|n_C D_{3/2}\rangle^2}{E(n_C D_{3/2})^2} + \frac{\langle g\|\bar{Q}\|n_C D_{5/2}\rangle^2}{E(n_C D_{5/2})^2}\right].\end{aligned} \tag{1.34}$$

The second order second non-adiabatic coefficient is

$$\gamma = \frac{1}{12}\sum_{n_C}\left[\frac{\langle g\|\bar{D}\|n_C, P_{1/2}\rangle^2}{E(n_C P_{1/2})^3} + \frac{\langle g\|\bar{D}\|n_C, P_{3/2}\rangle^2}{E(n_C P_{3/2})^3}\right]. \tag{1.35}$$

The third order adiabatic coefficient is

$$\begin{aligned}\delta = \frac{1}{30}\sum_{n'_C, n''_C}\Bigg[& -2\sqrt{10}\frac{\langle g\|\bar{D}\|n'_C, P_{1/2}\rangle\langle n'_C, P_{1/2}\|\bar{D}\|n''_C, D_{3/2}\rangle\langle n''_C, D_{3/2}\|\bar{Q}\|g\rangle}{E(n'_C P_{1/2})E(n''_C D_{3/2})} \\ & -2\frac{\langle g\|\bar{D}\|n'_C, P_{3/2}\rangle\langle n'_C, P_{3/2}\|\bar{D}\|n''_C, D_{3/2}\rangle\langle n''_C, D_{3/2}\|\bar{Q}\|g\rangle}{E(n'_C P_{3/2})E(n''_C D_{3/2})} \\ & +2\sqrt{6}\frac{\langle g\|\bar{D}\|n'_C, P_{3/2}\rangle\langle n'_C, P_{3/2}\|\bar{D}\|n''_C, D_{5/2}\rangle\langle n''_C, D_{5/2}\|\bar{Q}\|g\rangle}{E(n'_C P_{3/2})E(n''_C D_{5/2})} \\ & +\sqrt{5}\frac{\langle g\|\bar{D}\|n'_C, P_{3/2}\rangle\langle n'_C, P_{3/2}\|\bar{Q}\|n''_C, P_{3/2}\rangle\langle n''_C, P_{3/2}\|\bar{D}\|g\rangle}{E(n'_C P_{3/2})E(n''_C P_{3/2})} \\ & +2\sqrt{10}\frac{\langle g\|\bar{D}\|n'_C, P_{1/2}\rangle\langle n'_C, P_{1/2}\|\bar{Q}\|n''_C, P_{3/2}\rangle\langle n''_C, P_{3/2}\|\bar{D}\|g\rangle}{E(n'_C P_{1/2})E(n''_C P_{3/2})}\Bigg].\end{aligned} \tag{1.36}$$

The difference of the non-adiabatic energy of the K states of similar L can explain the observations in experimental data in Si^{2+} and barium. The difference in the second order energy between the two $K = L \pm 1/2$ states,

$$\delta E = E^{[2]}_{K=L+1/2} - E^{[2]}_{K=L-1/2} + E^{[3]}_{K=L+1/2} - E^{[3]}_{K=L-1/2} \quad , \tag{1.37}$$

gives the splitting of each fine structure level. The splitting of the energy levels is written below, where it has been divided into terms beginning with the most significant.

Reproduced with permission of the copyright owner. Further reproduction prohibited without permission.

The first non-adiabatic dipole and quadrupole splitting contribution:

$$\delta E^{[2]}_{1NA} = \frac{(2L+1)}{12}\left\langle r^{-6}\right\rangle_{nL}\sum_{n_C}\left[\frac{2\left\langle g\|\bar{D}\|n_C P_{1/2}\right\rangle^2}{E(n_C P_{1/2})^2} - \frac{\left\langle g\|\bar{D}\|n_C P_{3/2}\right\rangle^2}{E(n_C P_{3/2})^2}\right] + \frac{(2L+1)}{20}\left\langle r^{-8}\right\rangle_{nL}\sum_{n_C}\left[\frac{3\left\langle g\|\bar{Q}\|n_C D_{3/2}\right\rangle^2}{E(n_C D_{3/2})^2} - \frac{2\left\langle g\|\bar{Q}\|n_C D_{5/2}\right\rangle^2}{E(n_C D_{5/2})^2}\right]. \quad (1.38)$$

The second non-adiabatic dipole splitting contribution:

$$\delta E^{[2]}_{2NA} = -\frac{3(2L+1)}{4}\left\langle r^{-8}\right\rangle_{nL}\sum_{n_C}\left[\frac{2\left\langle g\|\bar{D}\|n_C P_{1/2}\right\rangle^2}{E(n_C P_{1/2})^3} - \frac{\left\langle g\|\bar{D}\|n_C P_{3/2}\right\rangle^2}{E(n_C P_{3/2})^3}\right]. \quad (1.39)$$

The third order first non-adiabatic splitting contribution:

$$\begin{aligned}\delta E^{[3]}_{1NA} = \frac{(2L+1)}{60}\sum_{n'_C,n''_C}\Bigg[&5\sqrt{10}\frac{\left\langle g\|\bar{D}\|n'_C P_{1/2}\right\rangle\left\langle n'_C P_{1/2}\|\bar{D}\|n''_C D_{3/2}\right\rangle\left\langle n''_C D_{3/2}\|\bar{Q}\|g\right\rangle}{E(n'_C P_{1/2})E(n''_C D_{3/2})}\\ &+2\frac{\left\langle g\|\bar{D}\|n'_C P_{3/2}\right\rangle\left\langle n'_C P_{3/2}\|\bar{D}\|n''_C D_{3/2}\right\rangle\left\langle n''_C D_{3/2}\|\bar{Q}\|g\right\rangle}{E(n'_C P_{3/2})E(n''_C D_{3/2})}\\ &+3\sqrt{6}\frac{\left\langle g\|\bar{D}\|n'_C P_{3/2}\right\rangle\left\langle n'_C P_{3/2}\|\bar{D}\|n''_C D_{5/2}\right\rangle\left\langle n''_C D_{5/2}\|\bar{Q}\|g\right\rangle}{E(n'_C P_{3/2})E(n''_C D_{5/2})}\\ &+\sqrt{5}\frac{\left\langle g\|\bar{D}\|n'_C P_{3/2}\right\rangle\left\langle n'_C P_{3/2}\|\bar{Q}\|n''_C P_{3/2}\right\rangle\left\langle n''_C P_{3/2}\|\bar{D}\|g\right\rangle}{E(n'_C P_{3/2})E(n''_C P_{3/2})}\\ &+\sqrt{10}\frac{\left\langle g\|\bar{D}\|n'_C P_{1/2}\right\rangle\left\langle n'_C P_{1/2}\|\bar{Q}\|n''_C P_{3/2}\right\rangle\left\langle n''_C P_{3/2}\|\bar{D}\|g\right\rangle}{E(n'_C P_{1/2})E(n''_C P_{3/2})}\Bigg]\left\langle r^{-9}\right\rangle_{nL}. \quad (1.40)\end{aligned}$$

It turns out that the energies of the $K = L \pm 1/2$ states are exactly equal if only the adiabatic terms are included, but the non-adiabatic contributions for different K states are different. This zero contribution from the adiabatic terms was also found in the indirect spin-orbit method. A look at the different couplings of each of the K states leads to some reasoning as to why different energies arise for different K

Reproduced with permission of the copyright owner. Further reproduction prohibited without permission.

states of similar L. Consider here the case of the dipole second order energy for the barium $6s_{1/2}20$(L=7) K states where the intermediate core states are $^2P_{1/2}$ states. The K=7.5 state will couple only to the $6p_{1/2}$nL state with L=8, since the $6p_{1/2}$, L=6 level does not have a state of similar K ($\Delta K = 0$). The L=7, K=6.5 state will couple just to states of $6p_{1/2}$nL with L=6 for the same reason. The different energy due to the specific Rydberg electron coupling results in different second order energies for different K states, which can be seen by inspection of Eq.(1.30). The Rydberg energies actually span a range of energies for the bound and continuum states. The average difference in energy of the Rydberg electron transition is a weighted average of the energies by the matrix elements of r^{-s} that couple the two Rydberg states. The denominator can be simplified using completeness as shown in Eq.(1.11). This numerator can also be simplified by using Eq.(1.16) as shown,

$$\begin{aligned} \bar{E}_{snll'} &\equiv \frac{\sum_{n'} |\langle n', l' | r^{-s} | n, l \rangle|^2 \left(E(n') - E(n)\right)}{\sum_{n'} |\langle n', l' | r^{-s} | n, l \rangle|^2} \\ &= \frac{\left[(s^2 - l(l+1) + l'(l'+1)\right] \left\langle r^{-(2s+2)} \right\rangle_{nl}}{2 \left\langle r^{-2s} \right\rangle_{nl}}. \end{aligned} \tag{1.41}$$

For the K=$L-1/2$ state in the example $\bar{E}_{2,20,7,6}$=-0.00479, while $\bar{E}_{2,20,7,8}$=0.00958 for the K=$L+1/2$ state. The energy of the K=$L-1/2$ coupling is smaller, as demonstrated for the example, and therefore causes a larger effect in the dipole non-adiabatic energy. The adiabatic energies of both the second and third order perturbation, which ignore the Rydberg energy difference, give zero contribution to the splitting. Similar arguments apply to the quadrupole couplings and higher non-adiabatic terms. Although this can be easily determined by examining the mathematics, a physical reason explaining why this is an entirely non-adiabatic effect is elusive.

Reproduced with permission of the copyright owner. Further reproduction prohibited without permission.

The K splitting result obtained here by inclusion of core spin in the polarization model can be reduced to the same result procured by the indirect spin-orbit method, while also providing insight into the magnitude of the splitting due to effects of core fine structure and deviations from pure LS coupling. The core matrix elements, allowig for deviations from pure LS coupling, can be written as

$$\begin{aligned}
< g\|\bar{D}\|P_{1/2} > &\equiv \sqrt{\frac{2}{3}}\,\langle g|r|n_C P\rangle\,(1+\epsilon_{p1}) \\
< g\|\bar{D}\|P_{3/2} > &\equiv \sqrt{\frac{4}{3}}\,\langle g|r|n_C P\rangle\,(1+\epsilon_{p3}) \\
< g\|\bar{Q}\|D_{3/2} > &\equiv \sqrt{\frac{4}{5}}\,\langle g|r^2|n_C D\rangle\,(1+\epsilon_{d3}) \\
< g\|\bar{Q}\|D_{5/2} > &\equiv \sqrt{\frac{6}{5}}\,\langle g|r^2|n_C D\rangle\,(1+\epsilon_{d5})
\end{aligned} \tag{1.42}$$

Also the core energies can be written in terms of the center of gravity and the core fine structure splitting.

$$E(L_{J_C}) = \frac{2\vec{L}\cdot\vec{S}}{2L+1}\Delta E(L_C) + E_{C.G.}(L_C) \tag{1.43}$$

where $E_{C.G.}$ is the center of gravity of the core fine structure levels. Note that if the states are purely LS coupled, then $\Delta\epsilon_p = 0$. Substituting the above energies and matrix elements into the first non-adiabatic splitting and only keeping terms of order

Reproduced with permission of the copyright owner. Further reproduction prohibited without permission.

ϵ gives

$$\delta E^{[2]}_{1NA} \approx \frac{1}{9}(2L+1)\left\langle r^{-6}\right\rangle \frac{\langle g|r|n_C P\rangle^2}{E_{C.G.}(P)^2}\left[\frac{(1+\epsilon_{p1})^2}{\left(1-\frac{2\Delta E(P)}{3E_{C.G.}(P)}\right)^2}-\frac{(1+\epsilon_{p3})^2}{\left(1+\frac{\Delta E(P)}{3E_{C.G.}(P)}\right)^2}\right]$$
$$+\frac{3}{25}(2L+1)\left\langle r^{-8}\right\rangle \frac{\langle g|r^2|n_C D\rangle^2}{E_{C.G.}(D)^2}\left[\frac{(1+\epsilon_{d3})^2}{\left(1-\frac{3\Delta E(D)}{5E_{C.G.}(D)}\right)^2}-\frac{(1+\epsilon_{d5})^2}{\left(1+\frac{2\Delta E(D)}{5E_{C.G.}(D)}\right)^2}\right] \tag{1.44}$$

Assuming that the fine structure is much smaller than the energy difference to the core excited state, a power series expansion of the energy denominator gives the same result as the indirect spin-orbit method if pure LS coupling is assumed, explicitly

$$E^{[2]}_{1NA} \approx \frac{2}{9}(2L+1)\left\langle r^{-6}\right\rangle \frac{\langle g|r|n_C P\rangle^2}{E_{C.G.}(P)^2}\left[\Delta\epsilon_p+\frac{\Delta E(P)}{E_{C.G.}(P)}+\cdots\right]$$
$$+\frac{6}{25}(2L+1)\left\langle r^{-8}\right\rangle \frac{\langle g|r^2|n_C D\rangle^2}{E_{C.G.}(D)^3}\left[\Delta\epsilon_d+\frac{\Delta E(D)}{E_{C.G.}(D)}+\cdots\right] \tag{1.45}$$

A few things can be noted from this reduction to the indirect spin-orbit splitting. First, the splitting depends largely on the size of the core excited state energy and the core fine structure. Second, the splitting vanishes entirely only if both the core fine structure is zero and the states are pure LS coupled. Note that this conclusion is in contrast to the previous conclusions of Snow et al. [39] and Shuman [40], which did not allow for deviations from LS coupling. The energies are known to a high level of precision, but the extent of LS coupling is unknown. Measurements of these splittings are sensitive to the deviation from pure LS coupling.

A strikingly similar but apparently unrelated effect appears for high-L Rydberg states with non-S-state cores. This is the "vector hyperpolarizability" term predicted by Zygelman and Clark et al. [42, 34]. This splitting has the same dependence on

Reproduced with permission of the copyright owner. Further reproduction prohibited without permission.

$\langle r^{-6} \rangle$ and L found here for the lowest order K splitting. Another common characteristic is that it is entirely the result of non-adiabatic effects. However the vector hyperpolarizability is predicted to be zero for S-state cores and is purely electrostatic.

1.3 Application of Long-Range Model

Section 1.1 presents the simple polarization model similar to the work of Drachman [4], which does not account for spin of the electrons, but extends the model to include systems larger than helium that have a $^2S_{1/2}$ ion core. The higher order terms of $\langle r^{-7} \rangle$ and $L(L+1)\langle r^{-8} \rangle$ are from the second non-adiabatic dipole term and the lowest multipole adiabatic third order energy. Larger systems are expected to be more non-adiabatic and therefore the series may not converge as quickly as helium, so higher order terms may be more significant.

Since this work is aimed at the study of larger systems where the core fine structure becomes increasingly important, the polarization model was re-derived to include core spin-orbit energies. This is the first presentation of the long-range model that includes the core spin, which is given in the second section. The results give the same overall series of terms converging to the final energy correction, but the coefficients of each term now specifically includes the core fine structure energies and related reduced matrix elements. A difference in energy is found for states of different total angular momentum, $K = L \pm 1/2$. This splitting should be evident in systems with large polarizabilities and significant core fine structure. As expected, the model including spin can be reduced to the spinless model by taking the weighted average of the two

Reproduced with permission of the copyright owner. Further reproduction prohibited without permission.

K states and assuming pure LS coupling to reduce the matrix elements while also neglecting core fine structure energies.

The models presented in the first and second sections can be used to interpret measurements of the fine structure pattern of sufficiently high-L. One such fine structure data pattern exists in helium. Previous experiments have very precisely determined several n=7, 9 and 10 fine structure intervals of helium [43]. The data from these studies will be used here as an example of application of the long-range polarization model.

The measured helium fine structure intervals used in this example are listed in Table 1.2. Also listed are the contributions to these fine structure splittings from mechanisms not explicitly included in the long-range model. The first contribution shown is from relativistic effects, given here as ΔE_{rel}. The other listed value is the "effective second order energy". The long-range model describes the energy of the system with a series of terms, which can be written as the expectation value of an effective potential, $V_{eff} = -\frac{1}{2}\alpha_d r^{-4} - \frac{1}{2}\alpha_Q r^{-6} + 3\beta_d r^{-6} + \cdots$. The "effective second order energy" contribution is from the second order perturbation of the first term in the effective potential, corresponding to the dipole polarizability. This "effective second order energy" is also referred to as the series mixing term and is discussed in detail by Arcuni, et al. with respect to the H_2 molecule [18]. The energy intervals with the relativistic and second order contributions removed will be referred to as the "corrected" energy intervals.

The corrected energy intervals normalized by $\Delta \langle r^{-4} \rangle_{nl}$ are shown in Table 1.2 with the corresponding $\Delta \langle r^{-6} \rangle_{nl} / \Delta \langle r^{-4} \rangle_{nl}$ value which determines the position on the x-

Reproduced with permission of the copyright owner. Further reproduction prohibited without permission.

Table 1.2: The relativistic (ΔE_{rel}) and second order (ΔE_{Sec}) contributions to each measured transition are shown in columns 3 and 4 respectively. ΔE_{Corr} is the measured interval ΔE_{Obs} corrected for the relativistic effects and second order energies. The corrected interval is normalized to $\Delta < r^{-4} >$ in column 6 and the calculated ratio $\Delta < r^{-6} > / \Delta < r^{-4} >$ for each transition is also given.

(n,L)-(n',L')	ΔE_{Obs} (MHz)	ΔE_{rel} (MHz)	ΔE_{Sec} (MHz)	$\Delta \langle r^{-4} \rangle$ (MHz)	$\Delta \langle r^{-6} \rangle / \Delta \langle r^{-4} \rangle$	$\Delta E_{Corr} / \Delta \langle r^{-4} \rangle$
(10,4)-(10,5)	491.00726(36)	7.07444	0.18722	3474.5398	0.0119	0.13922581(10)
(10,5)-(10,6)	157.05241(23)	4.89770	0.01657	1086.1587	0.0046	0.14006991(21)
(10,6)-(10,7)	60.81595(20)	3.59164	0.00217	407.5671	0.0021	0.14039930(49)
(10,7)-(10,8)	27.17472(52)	2.74654	0.00037	173.8129	0.0011	0.14054086(298)
(9,4)-(9,5)	665.84935(58)	9.70431	0.24957	4709.8032	0.0116	0.13926176(12)
(9,5)-(9,6)	211.79171(33)	6.71837	0.02166	1463.6239	0.0044	0.14009862(23)
(7,4)-(7,5)	1359.0003(25)	20.6252	0.4744	9598.2577	0.0104	0.13938995(26)
(7,5)-(7,6)	423.4887(11)	14.2790	0.0380	2918.5653	0.0036	0.14019618(38)

axis. The hydrogenic radial expectation values are listed in Appendix D. Figure 1.4 is the polarization plot for the n=9 and 10 high-L states of helium. This polarization plot can be fit by the following equation,

$$\frac{E}{\Delta \langle r^{-4} \rangle} = A_4 + A_6 \frac{\Delta \langle r^{-6} \rangle}{\Delta \langle r^{-4} \rangle} + A_8 \frac{\Delta \langle r^{-8} \rangle}{\Delta \langle r^{-4} \rangle} \tag{1.46}$$

where A_4 is 1/2 the dipole polarizability, α_d. A_6 is 1/2 the quadrupole polarizability, α_Q, minus three times the first correction term to the dipole polarizability, β_d, and A_8 is a contribution from higher order terms.

The parameters fit to this data pattern,

$$\begin{aligned} A_4 &= 0.140692(10) \\ A_6 &= -0.1392(33) \\ A_8 &= 0.76(10), \end{aligned}$$

result in a dipole polarizability, $\alpha_d = 2A_4$=0.281384(20), and a quadrupole polariz-

Reproduced with permission of the copyright owner. Further reproduction prohibited without permission.

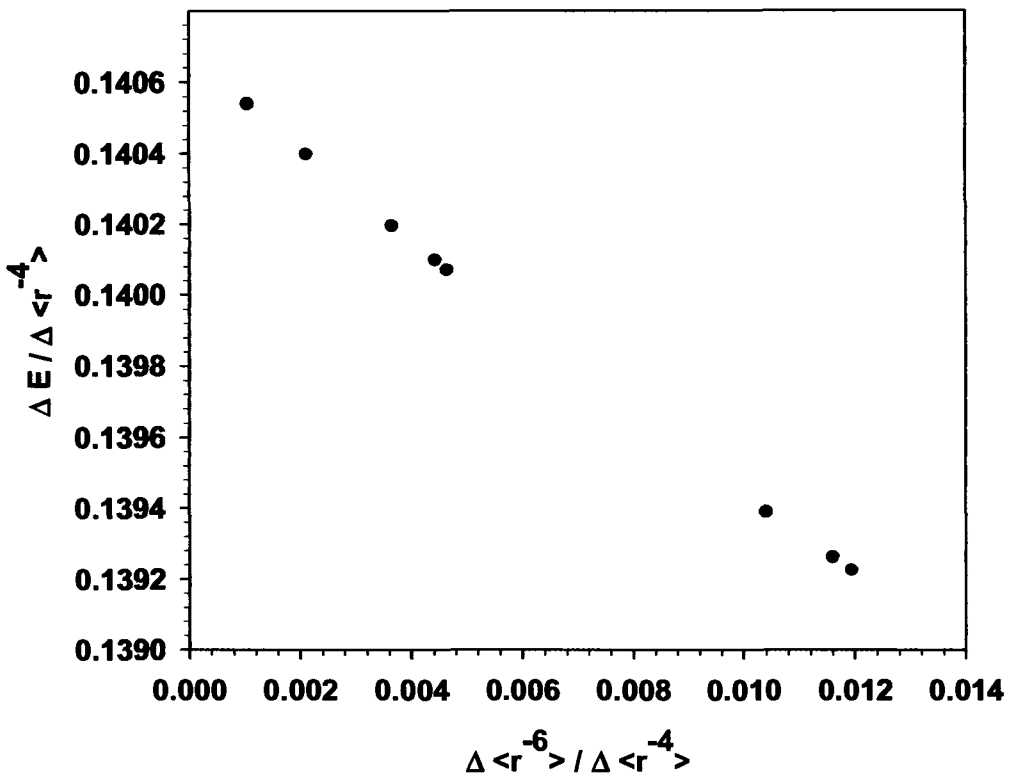

Figure 1.4: The measured helium fine structure intervals corrected for relativistic and 2nd order energy effects as described in the text and normalized to $\Delta < r^{-4} >$ are plotted versus $\Delta < r^{-6} > / \Delta < r^{-4} >$.

ability, $\alpha_Q = 2A_6 + 6\beta_d$=0.226(7), with the assumption that the first non-adiabatic dipole coefficient, β_d, is 0.08398 as calculated by Drachman [4].

In order to implement the extended long-range model, which should be more accurate than neglecting terms of $\langle r^{-7} \rangle$ and $L(L+1)\langle r^{-8} \rangle$, the second non-adiabatic dipole and first third order adiabatic terms must be calculated. Use of theoretically calculated values of $\delta = 213/512$ and $\gamma = 319/12288$ from Drachman [4] leads to the following contributions to the state energies,

$$E_{H.O.T.} = 0.249545 < r^{-7} >_{nL} -0.093457L(L+1) < r^{-8} >_{nL} . \qquad (1.47)$$

Reproduced with permission of the copyright owner. Further reproduction prohibited without permission.

The helium data with this higher order contribution subtracted off is plotted in Fig. 1.5. Only a very slight difference can be observed and largely for the lower L states.

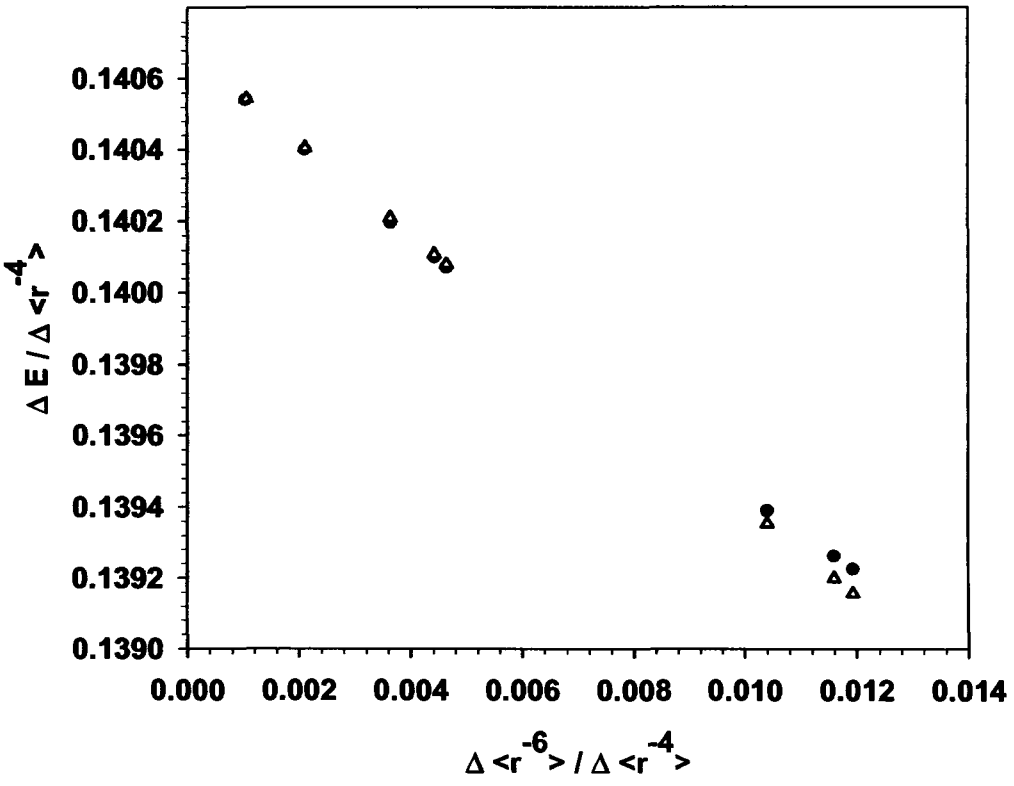

Figure 1.5: The corrected fine structure intervals normalized to $\Delta < r^{-4} >$ (solid points) and the corrected intervals with the higher order term contributions removed normalized to $\Delta < r^{-4} >$ (open points) are plotted versus $\Delta < r^{-6} > / \Delta < r^{-4} >$.

The fit to the helium data pattern with the higher order contribution removed gives the following values for the parameters,

$$A_4 = 0.140677(6)$$

$$A_6 = -0.1295(19)$$

$$A_8 = 0.099(56),$$

Reproduced with permission of the copyright owner. Further reproduction prohibited without permission.

Table 1.3 summarizes the results of the two forms of analysis and compares with the theoretical values. The dipole polarizability is extremely accurate and precise. The slope of the polarization plot, however, has a precision of 2% and differs from theory by about 2 standard deviations. The theoretical values listed here are the result of calculations by Drachman [4] with a few additional corrections of very small magnitude but necessary for this level of precision. These corrections to the theoretical intercept account for reduced mass corrections (9.6×10^{-5}), relativistic correction (-3.1×10^{-5}), lamb shift correction (4×10^{-6}) and retardation correction (-1.3×10^{-5}). The calculated slope includes the reduced mass corrections and it is noted that the relativistic corrections to the slope are small [16].

Table 1.3: The parameters extracted from the fine structure measurements by both methods of analysis are listed with the theory predictions.

	Experiment	Experiment with H.O.T.	Theory
A_4	0.140692(10)	0.140677(6)	0.140681
A_6	-0.1392(33)	-0.1295(19)	-0.1350

In order to accurately treat experimental data with this model, all of the assumptions made in the calculations must be met. The two basic assumptions made are that the Rydberg electron is always a greater distance from the nucleus than the core electrons and it is distinguishable from any of the core electrons. This was necessary so as to be able to neglect core penetration and exchange interactions. Both of these assumptions are valid if the Rydberg electrons are in sufficiently high angular momentum states. As discussed earlier the centrifugal barrier provides a naive

Reproduced with permission of the copyright owner. Further reproduction prohibited without permission.

estimate of how sufficiently high-L can be defined, typically $L \geq 5$. In addition to these assumptions the radial matrix elements must also be well defined, which puts a restriction of $L \geq 3$ if only terms of $\langle r^{-s} \rangle$ for $s \leq 8$ are concerned.

This, however, is not the complete story, because within the polarization model an adiabatic expansion was performed. This adiabatic expansion, Eq. (1.9), is in fact a power series expansion of the energy denominator, involving the ratio of the Rydberg electron energy difference to the ion core energy difference. Typically for the power series to converge, this ratio of the Rydberg energy to the energy of the core must be less than one. The application of this model to experimental data would ideally only include the first few terms in the series. Therefore a ratio of much less than one would be preferred so that the neglect of the remaining terms would be insignificant. In other words, the hope is to have a rapidly converging series.

It is not exactly the Rydberg energy difference that causes the non-adiabatic effects, but the energy distribution of the matrix elements $\langle nl|r^{-s}|n'l' \rangle$. The magnitude of the spread in energies determines the magnitude of the non-adiabatic effects. Instead of calculating each matrix element over this energy spread, the average Rydberg electron energy difference for coupling by matrix elements of r^{-s}, as defined in Eq.(1.41) and repeated here for convenience,

$$\Delta\bar{E}_{snll'} = \frac{[s^2 - l(l+1) + l'(l'+1)] \left\langle r^{-(2s+2)} \right\rangle_{nl}}{2 \left\langle r^{-2s} \right\rangle_{nl}},$$

will be used here. Figure 1.6 shows the absolute value of the average Rydberg dipole energy (s=2) for each of the squared matrix elements, $\Delta L = \pm 1$. Also shown are the energies of the first excited state for the systems of interest in this study. If

Reproduced with permission of the copyright owner. Further reproduction prohibited without permission.

the average Rydberg energy is much less than the core energy, then the long-range model series should converge rapidly, which is a simple way of determining whether the dipole series will converge. Both extremes shown in fig. 1.6, helium and barium, are expected to converge for $L \geq 5$.

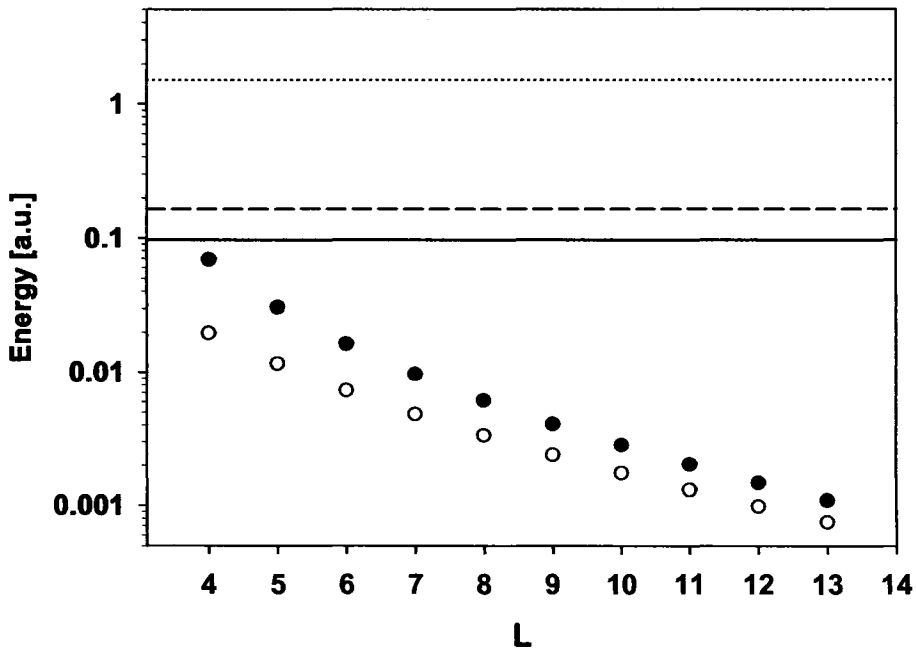

Figure 1.6: The absolute value of the average Rydberg dipole energy difference, $\bar{E}_{1,20L,L'}$, is plotted here for several values of L to $L' = L + 1$ (solid points) and $L' = L - 1$ (open points). The lines represent the first excited dipole core energy of barium (solid), magnesium (dashed), and helium (dotted).

Another check on the convergence of the dipole series is performed by calculation of each of the terms. Table 1.4 lists theoretical values for each of the dipole terms in the polarization model for a case in helium and in barium. The contributions to the total second order dipole energy are shown to decrease rapidly for the first three terms in the series. This reinforces the conclusion of convergence drawn from Fig. 1.6

Reproduced with permission of the copyright owner. Further reproduction prohibited without permission.

for both helium and barium and consequently also for systems which have properties similar to these systems.

Table 1.4: The calculated second order adiabatic and first two non-adiabatic dipole energy contributions are listed here for several states of interest. The progression to higher order terms is seen here to decrease rapidly for helium and barium, illustrating the convergence of the adiabatic expansion.

Helium (n,L)	$E^{[2]}_{Ad.}$	$E^{[2]}_{1NA}$	$E^{[2]}_{2NA}$
(10,4)	-747.7	12.0	-1.59
(10,5)	-258.8	1.55	-0.08
(10,6)	-106.0	0.28	-0.01
(10,7)	-48.6	0.06	-0.001
Barium (n,L)			
(20,6)	-6591	342	-187
(20,7)	-3160	87	-31
(20,8)	-1658	26	-6.6
(20,9)	-932	9	-1.7
(20,10)	-554	3	-0.5
(20,11)	-344	1	-0.2

The next question to ask is whether the quadrupole series will also converge. Figure 1.7 plots the absolute value of the average ΔE_{Ryd} for the quadrupole (k=2) term for each of the three squared matrix elements $\Delta L = 0, \pm 2$. For systems such as helium and magnesium the Rydberg energy is insignificant compared to even the first excited core D state energy shown as dotted and dashed lines respectively. However, barium has an extremely low lying first excited D state, which suggests that the power series may not converge in the polarization model even for states of $L = 7$.

In order to examine the significance of the non-adiabatic effects for each L level, the contribution to the second order energy of barium from just the first excited state, 5D, can be evaluated separately. A multiplicative factor, k_Q, can be introduced to account for non-adiabatic effects instead of using a power series expansion [13, 23].

Reproduced with permission of the copyright owner. Further reproduction prohibited without permission.

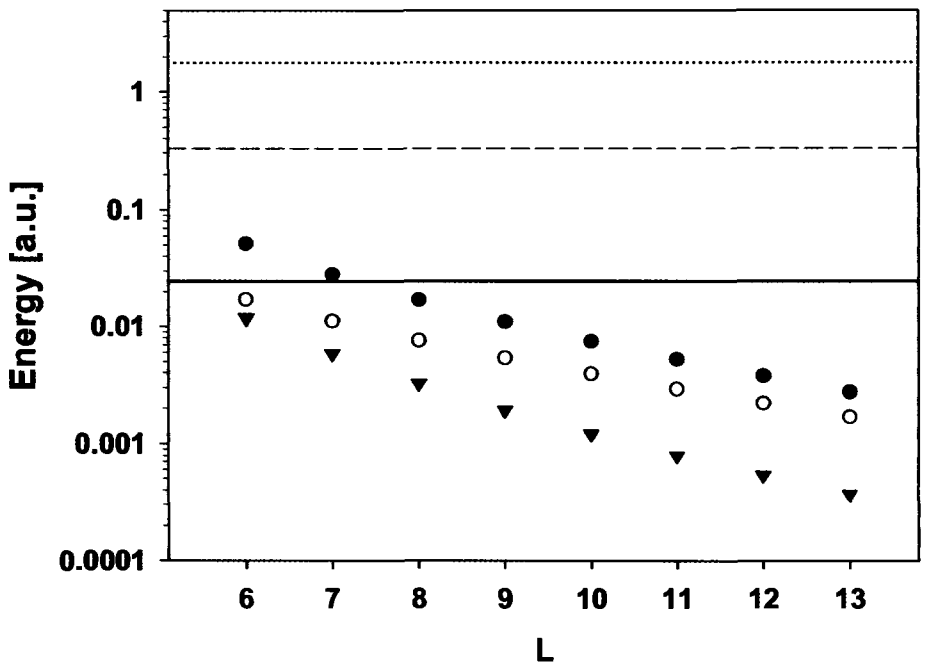

Figure 1.7: The absolute value of the average Rydberg quadrupole energy differences, $\bar{E}_{2,20,L,L'}$, are plotted here for several values of L to $L' = L + 2$ (solid points), $L' = L - 2$ (open points), and $L' = L$ (solid triangles). The lines represent the first excited quadrupole core energy of barium (solid), magnesium (dashed), and helium (dotted).

The k_Q correction factor is defined as follows,

$$E^{[2]}_{k=2}(6^2S_{1/2}, nL)_{5D} = -\sum_{n',l'} \frac{A(2,0,2,L,l')^2 \langle g\|Q\|5D\rangle^2 \left\langle nL\left|\frac{1}{r^3}\right|n'l'\right\rangle^2}{E(5D) + [E(n') - E(n)]}$$
$$\equiv -\frac{1}{2} k_Q \alpha^0_Q \langle r^{-6}\rangle \qquad (1.48)$$

where

$$\alpha^0_Q = \frac{2}{5} \frac{\langle 6S|r_i^2|5D\rangle^2}{E_{5D} - E_{6S}}. \qquad (1.49)$$

The factor, k_Q, can be estimated by three different methods. The three methods only vary in the treatment of the energy denominator in the second order energy from the core 5D state. Method 1 uses the "adiabatic expansion" including only the first non-

Reproduced with permission of the copyright owner. Further reproduction prohibited without permission.

adiabatic term. Method 2 uses the Dalgarno-Lewis technique to explicitly sum the matrix elements in Eq. (1.48). Both of these two methods are described by Snow et al. [23]. Method 3 approximates the second order quadrupole energy by substituting $\Delta\bar{E}_{snLl'}$, given in Eq.(1.41), into the energy denominator of Eq. (1.48. The matrix elements obtained from relativistic many-body theory are used in these calculations, but the actual value of the matrix element is immaterial to the comparison of the three methods. Table 1.5 lists the K_Q values for the n=17 $6 \leq L \leq 10$ calculated by all three methods. From the comparison of Method 2 k_Q's and the Method 1 values, it can be seen that the adiabatic expansion in Method 1 does not adequately describe the non-adiabatic effects for these states. The correction terms do not, in fact, monotonically decrease, but change sign near $L = 7$. Method 3 is only a few percent different from the explicitly calculated values of the Dalgarno-Lewis technique in Method 2. This instills confidence in the calculated k_Q values obtained by Method 2.

Table 1.5: The non-adiabatic quadrupole correction factors, k_Q, for n=17 barium of $6 \leq L \leq 10$ are listed for three different methods of calculation. Method 1 uses the adiabatic expansion including only the first two terms of the series. Method 2 uses the Dalgarn-Lewis method [23]. Method 3 uses an average energy difference for the Rydberg electron.

(n,L)	Method 1	Method 2	Method 3
(17,6)	0.201	1.614	1.380
(17,7)	0.609	1.059	0.996
(17,8)	0.789	0.984	0.951
(17,9)	0.878	0.971	0.953
(17,10)	0.927	0.973	0.963

Figure 1.8 plots the k_Q correction factors of a few values of L with n=17 for all three methods of calculation. This plot illustrates the significant difference in the non-

Reproduced with permission of the copyright owner. Further reproduction prohibited without permission.

adiabatic correction by use of Method 1, which assumes convergence of the adiabatic expansion. Both Methods 2 and 3 give correction factors that scale similarly but with just slightly different magnitude.

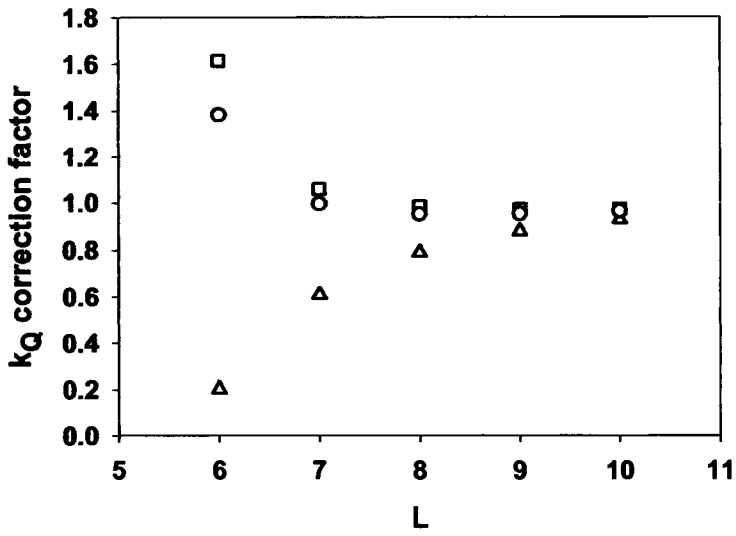

Figure 1.8: The open squares are the non-adiabatic quadrupole correction factors, k_Q, estimated by Method 2 involving the Dalgarno-Lewis technique. The open triangles are the approximate correction factor from Method 1, the adiabatic expansion. The open circles are the approximate energies using Method 3, the average energy difference substitution. This illustrates that the adiabatic expansion method (Method 1) is not adequate to model the data pattern.

Figure 1.9 plots the quadrupole energy from only the 5D excited state of barium versus $\Delta\langle r^{-6}\rangle / \Delta\langle r^{-4}\rangle$, where the slope is one half the quadrupole polarizability for the purely adiabatic case as shown by solid circles. The hollow squares represent the inclusion of the k_Q multiplicative factor, calculated by use of the Dalgarno-Lewis method, to the adiabatic 5D quadrupole energy, which is the best estimate of the true energy. For states of $L \geq 7$, k_Q differs from one by no more than 7%. However, it can be seen that for L=6 the deviation from adiabatic is large. The open triangles

Reproduced with permission of the copyright owner. Further reproduction prohibited without permission.

approximate the total 5D quadrupole energy with the adiabatic expansion. As was mentioned in reference to the calculated values of k_Q, this illustrates the fact that the adiabatic expansion does not adequately model the non-adiabatic effects for $L \leq 10$. The hollow circles are the 5D quadrupole energy with the correction factor calculated by approximating the Rydberg electron energy with the average energy difference.

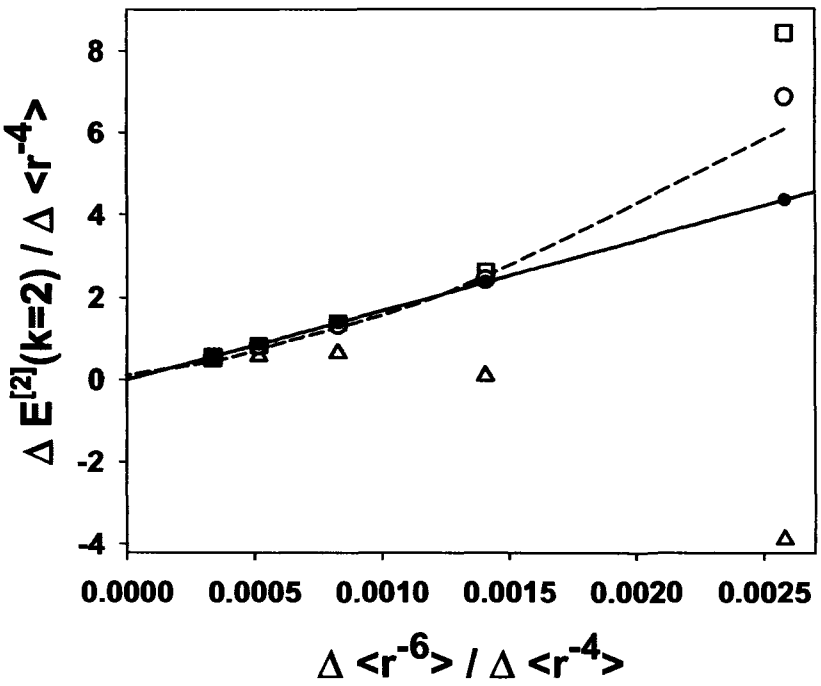

Figure 1.9: The solid points represent the contribution to the adiabatic quadrupole second order energy of barium by the 5D excited core state for a range of transitions from L to L+1 starting with L=6 at 0.0025 and increasing in L as x=0 is approached. The open squares are the same quadrupole second order energies, but include a calculated multiplicative factor to correct for non-adiabatic effects by Method 2 involving the Dalgarno-Lewis technique. The open triangles are the approximate 5D energy using Method 1, the adiabatic expansion. The open circles are the approximate energies using Method 3, the average energy difference substitution. The dotted line is a fit to the $L \geq 7$ transitions, which includes a term that scales with $\Delta < r^{-8} > / \Delta < r^{-4} >$, to the corrected energies. The solid line is a similar fit to the adiabatic energies.

What is of interest is specifically how the slope is effected by the non-adiabatic

Reproduced with permission of the copyright owner. Further reproduction prohibited without permission.

contributions for states of $L \geq 7$. The data pattern in fig. 1.9 can be fit to a linear function, which ignores any non-adiabatic effects. The fitted slope to the corrected data (open squares) of $L \geq 7$ results in a slope that is 14% larger than the purely adiabatic result. This data pattern can instead be fit to a function which accounts for the first non-adiabatic contribution by inclusion of a term that scales with $\Delta \langle r^{-8} \rangle / \Delta \langle r^{-4} \rangle$. This fit to the states of $L \geq 17$, shown as a dashed line, results in a slope that is 27% smaller than expected. Neither method of fitting adequately treats the data pattern. The best way to proceed with the data is to include a correction to the energy interval from the calculated k_Q factor to account for the non-adiabatic effects in the second order quadrupole energies of barium.

The quadrupole energy contribution from the lowest excited core state is less than approximately 2% of the total 2nd order energy. This puts in context the overall significance of the non-adiabatic correction term. These correction factors were used to explain the discrepancy in the fine structure data pattern of barium for states including $4 \leq L \leq 9$, where the $L \leq 6$ did not lie on the predicted slightly curved line [23]. However, for a large system such as barium, the contribution of other possible non-linear effects may not be negligible. For instance, penetration of the ion core by the Rydberg electron becomes increasingly significant for states of $L \leq 6$, to name one of many. There is a need for the non-adiabatic correction factor, however, the interpretation of the k_Q term to extract the contribution of the first excited state to the total quadrupole polarizability made by Snow, et al. was naive. Not only are there other possible contributing factors, but the fit is dependent on the very small deviations of the correction terms from the actual. The non-linear effects

Reproduced with permission of the copyright owner. Further reproduction prohibited without permission.

can be accounted for by use of the multiplicative correction factor, but extraction of information from this parameter is probably not reliable.

Reproduced with permission of the copyright owner. Further reproduction prohibited without permission.

Chapter 2

Experimental Techniques

2.1 Overview of the RESIS Technique

Measurements of fine structure patterns can provide precise determinations of the ion core properties of high-L Rydberg atoms and ions such as dipole polarizability and quadrupole moments, which control these interactions and so set the scale of the fine structure patterns. Achieving precise polarizabilities requires measurements in a wide enough range of L's to establish the fine structure pattern clearly, and in states with large enough L, typically L$\geq$5, so that complications due to core penetration can be neglected. The Resonant Excitation Stark Ionization Spectroscopy technique provides a general method of accessing the high angular momentum levels that are required for such studies. The apparatus is shown schematically in Fig. 2.1. With the RESIS method, the Rydberg atoms, molecules or ions are formed by single electron capture from an accelerated ion beam. The capture occurs from collision with a thermal beam of Rb that is stepwise excited to its 9F/10D state by three diode lasers. All possible

Reproduced with permission of the copyright owner. Further reproduction prohibited without permission.

angular momentum states are formed at some level in this process. All states of n≥15 are ionized by Stark ionization in the pre-stripper and repelled out of the beam path. This is done in order to remove any initial upper Rydberg state population, which would be Stark ionized in the detector, causing a background regardless of laser excitation. Specific high-L Rydberg levels in the resulting fast beam can be excited upward by a Doppler-tuned CO_2 laser. The upper state of the excitation is ionized in a Stark field and the resulting ions are steered into a channel electron multiplier (CEM) for detection.

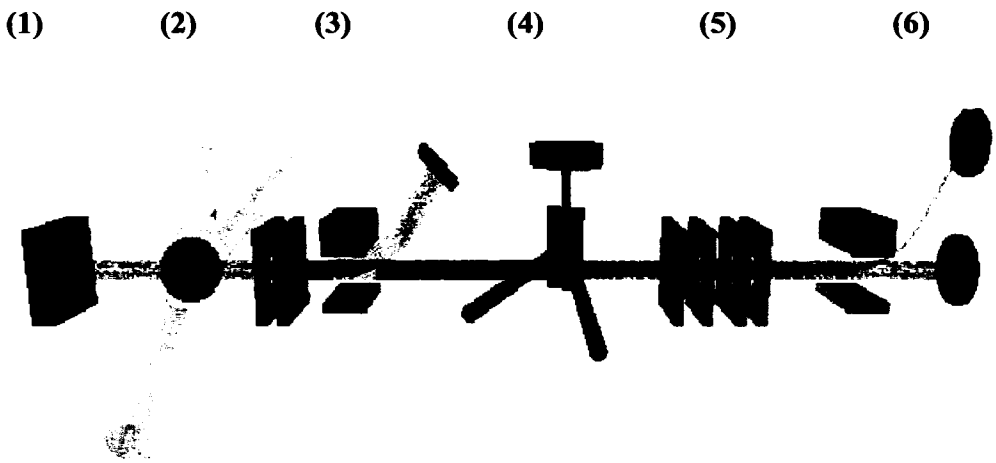

Figure 2.1: Schematic diagram of optical RESIS apparatus used for this study. (1) An ion beam is created in a Colutron model-101 ion source. The ions are then collided with a selectively excited 9F/10D Rb target at (2) where some ions capture an electron. States of n = 15 and higher are then Stark ionized in the initial stripper and deflected with the remaining Ba+ ions at (3) to be collected in a Faraday cup. Neutral barium atoms with n<15 enter the CO_2 laser interaction region (4). Here a Doppler-tuned CO_2 laser excites a particular transition to a higher state of neutral barium, for example n=9 atoms might be excited to n=20. The excited states are then Stark ionized in the stripper and focused by the lens at (5) and the resulting signal ions are deflected and collected on a channeltron plate at (6) while the neutral beam continues straight and is collected in a Faraday cup.

Reproduced with permission of the copyright owner. Further reproduction prohibited without permission.

The fact that the laser excitation is upwards from existing levels means that all angular momentum states are eligible to be detected in this way, and as long as the fine structure energies exceed the laser resolution, individual Rydberg levels can be selectively detected. Figure 2.2 shows an optical RESIS scan of n=10 to n=30 neutral magnesium. In some cases, such as barium, the fine structure energies have been large enough that simply measuring the frequencies of the RESIS transitions was sufficient to determine the fine structure energies at an interesting level of precision[23]. In most past studies, the relatively small fine structure intervals have been measured directly using microwave resonance methods, relying on the selective RESIS excitation to provide detection of those transitions.

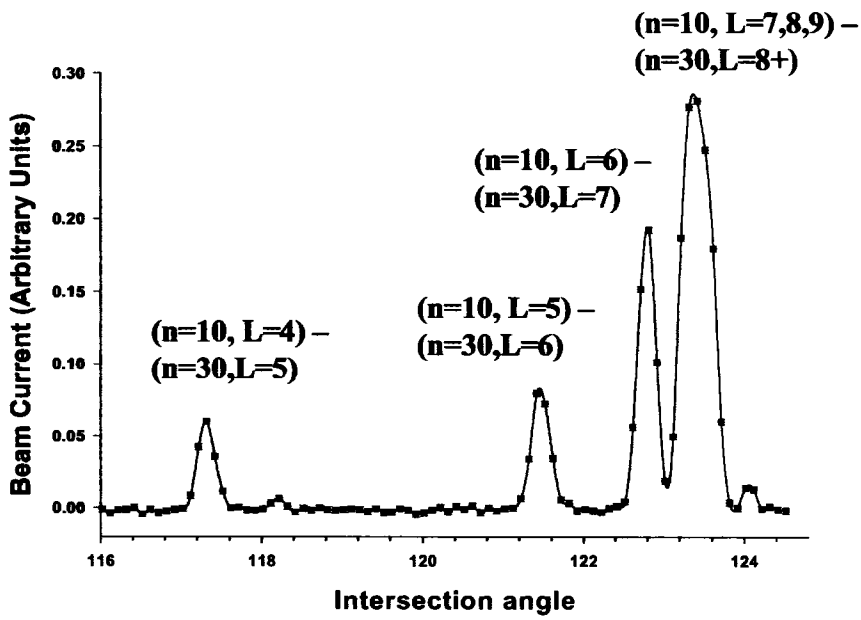

Figure 2.2: Measured ion current resulting from the magnesium n=10 excitation to the n=30 states versus the recorded stage angle. Levels within n=10 with L=4 to 6 are resolved. The unresolved L>6 levels form the large peak near where the hydrogenic transition would occur on the right.

Reproduced with permission of the copyright owner. Further reproduction prohibited without permission.

In this work a microwave resonance in the upper Rydberg state of the RESIS transition is detected using the method demonstrated in earlier H_2 studies. [18] All angular momentum states of the upper Rydberg states will be ionized in the Stark field, so an additional technique must be implemented in order to determine if a microwave transition occurred in the upper Rydberg state. In order to differentiate whether the angular momentum state has changed as a result of the microwave interaction, a second laser interaction region is inserted before the detector. Now the RESIS apparatus is extended to include a coaxial microwave region between two CO_2 laser interaction regions. The CO_2 lasers are set to the same frequency and angle. The first laser populates a high-L state in an upper principal quantum state, n. The second laser is used to repopulate the upper state if population has been transferred to a different angular momentum state by the microwave interaction. Figure 2.3 shows an example of population transfer in the microwave RESIS technique. For example, let it be assumed for simplicity that all the n=9 L states are equally populated with 8000 atoms each, and the n=20 upper Rydberg state has zero population as a result of the pre-ionizer. The laser excitation from the n=9 and L=7 state to the n=20 and L=8 state saturates the transition putting 4000 atoms in both the lower and upper Rydberg states. This is followed by a microwave transition from the n=20 and L=8 to the L=9 state, moving 2000 atoms to the n=20, L=9 state. The second laser saturates the optical transition again, equalizing the populations of the two states involved, placing 1000 more electrons in the n=20 and L=8 state. When the entire n=20 Rydberg state population is ionized 5000 atoms are detected if the microwave transition has occurred , 4000 if not.

Reproduced with permission of the copyright owner. Further reproduction prohibited without permission.

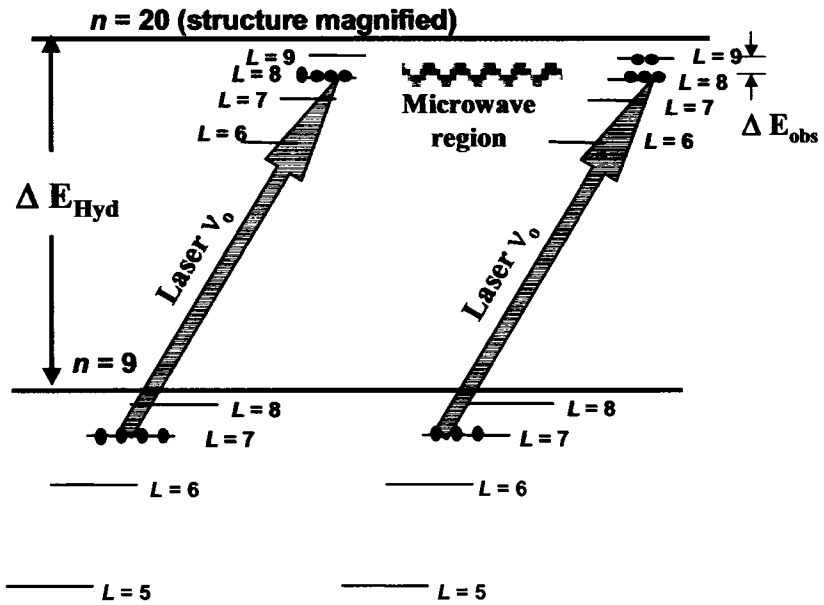

Figure 2.3: The fine structure of the n=9 and magnified n=20 high-L levels are illustrated. Each circle represents 1000 atoms residing in the energy level they are overlapping. The first laser puts each populations in the n=9, L=7 and n=20, L=8 levels. A microwave transition moves 2000 of the n=20, L=8 atoms to the n=20, L=9 level. The second laser re-equilibrates the n=9, L=7 and n=20, L=8 levels, putting an additional 1000 atoms in the n=20, L=8 state. All of the n=20 population will be ionized and detected. A total signal of 5000 ions is found if the microwave transition occurs, but only 4000 ions are detected if not.

2.2 Population and preparation of Rydberg States

A 9.5 keV ion beam is created in a Colutron model-101-O ion source and the ion mass is selected by use of a $\bar{\mathbf{v}} \times \bar{\mathbf{B}}$ velocity filter. The Colutron Ion Beam Kit consists of an ion source, heat sink, acceleration and focusing system, vertical deflection plates, and velocity filter. A 20 mil tungsten filament heats the area and vaporizes the metal charge, and emits electrons which ionize the charge. Typical running conditions required full power on the filament with a maximum of 19A/18V and a low ion source pressure near 100 mTorr of argon support gas. An oven can also be used in

Reproduced with permission of the copyright owner. Further reproduction prohibited without permission.

this Colutron model ion source. The oven consists of a 15 mil tungsten wire wrapped tightly around a hollow ceramic tube. It can be run at a few amperes in order to create higher temperatures to vaporize the charge metal. This additional source of heat will also alleviate the stress on the filament by allowing the filament to be run at a lower power, which results in a longer filament lifetime. The solid charge can also be placed inside the ceramic tube with quartz wool packed on either side to keep the charge in place, but allow for the transport of the vaporized charge material. This method, however, was not found to significantly improve the quantity or quality of the ion beams. The anode voltage set at approximately 100 V creates a discharge in the plasma. Then the ions are extracted and accelerated by the 9.5 keV high voltage supply. Ion beams of the metals vary in size from 6nA to about 50nA on a good day. Careful attention must be given to prevent oxidization of the metals by exposure to atmosphere.

The ions are collided with a selectively excited 9F/10D Rb Rydberg target. An ampoule of Rb is heated to approximately 230 degrees Celsius to create a thermal beam. This thermal beam is excited by three New Focus Vortex diode lasers to populate the 9F state. The presence of a maser transition between the 9F and 10D state, which lies just below the former state in energy, populates the 10D state and then the electron can decay to the 5P state and emit a blue photon [44]. A phototube with an interference filter detects the fluorescence which allows for a relative measurement of target strength. Depending on the target conditions, charge transfer occurs for 0.5 to 2 percent of the ion beam. When charge transfer of a single electron takes place, the binding energy of the electron tends to remain constant, creating a fast neutral beam

Reproduced with permission of the copyright owner. Further reproduction prohibited without permission.

with a population centered about n=9 and with a significant fraction in the n=9 and 10 levels. All the angular momentum states are present to some level in the neutral beam. The position of the Rydberg target is optimized to create the largest neutral beam by adjusting the intersection point of the three diode lasers to peak an optical or microwave signal. A difference of approximately a millimeter can have as much as a factor of two difference in signal size.

Excitations by the CO_2 laser populate higher principal quantum states which are detected by Stark ionization. The signal to noise is much improved by pre-ionizing any atoms initially formed in these upper states. This is performed by the pre-ionizer, pictured in Fig. 2.4. A new design was implemented to increase the maximum stripping field possible and also to reduce the beam path between the Rydberg target and the laser interaction region. Two stainless steel plates are separated by 5 mm with a 0.5 mm aperture in the center for the beam to pass through. The upstream plate is at ground while the other is held at a potential of +12.75 kV. The resulting longitudinal field of 25500 V/cm will ionize any states of $n \geq 15$. Since the potential is greater than that of the beam, the initial stripper will also repel any of the ions that are present. This piece of apparatus is contained within a $2\frac{3}{4}$" conflat cross, which reduces the distance from the Rydberg target to the laser interaction region to 29 cm from the previous 50 cm setup [45]. The reduction of this distance decreases the loss of states of interest with shorter lifetimes.

Reproduced with permission of the copyright owner. Further reproduction prohibited without permission.

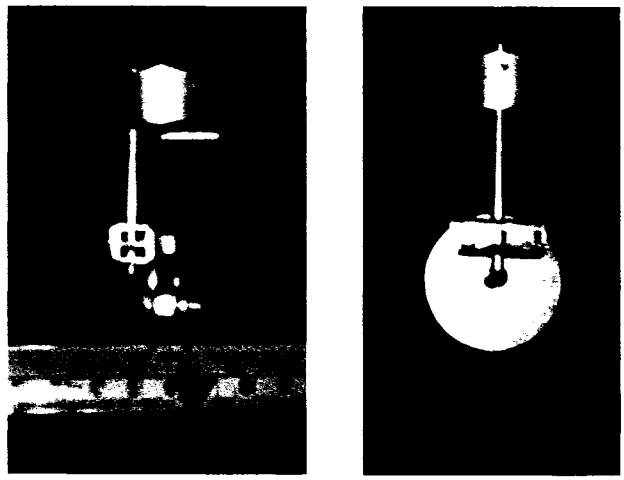

Figure 2.4: The Pre-ionizer

2.3 Resonant Excitation

The Doppler tuning range of the CO_2 laser determines which magnesium and barium lines can be observed. The CO_2 laser can be set to any of the dozens of discrete laser lines, shown in Fig 2.5, and then continuously tuned from that frequency by changing the angle of intersection with the neutral beam. The speed of the beam limits the tuning range to less than 0.04 percent of the CO_2 laser line frequency, or about 0.38 cm^{-1} for barium and about 0.07 percent or 0.76 cm^{-1} for magnesium. Since the separation between CO_2 laser lines is about 2 cm^{-1}, this leaves some frequencies unavailable. A majority of transitions to the high angular momentum states of n=9 to n=17 or 20 can be obtained. Transitions near the center of the gain curve were chosen because the higher power was necessary for saturation of the transition in order to produce adequate signal to noise ratios.

As seen in Fig. 2.1, the Doppler tuning of the CO_2 laser is accomplished with a

Reproduced with permission of the copyright owner. Further reproduction prohibited without permission.

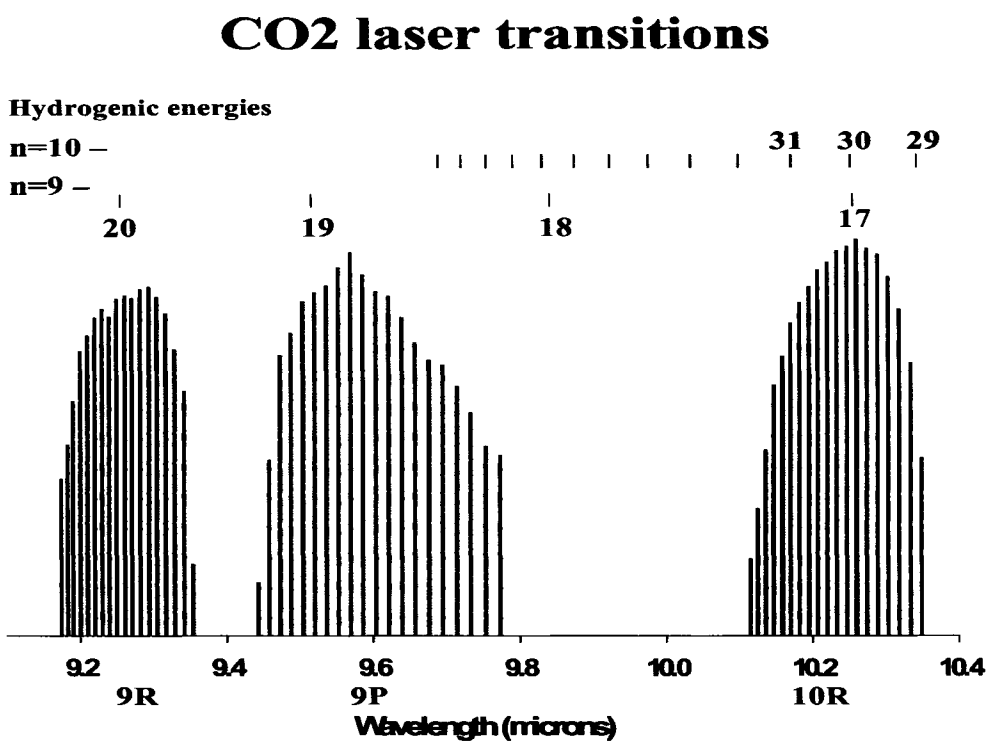

Figure 2.5: Three branches of the CO_2 laser spectrum are plotted here, where the amplitude corresponds to the line strength. The hydrogenic transition energies for n=9 and 10 to higher Rydberg levels are shown above for this range of wavelengths.

single mirror mounted on a rotation stage. The laser interaction region (LIR) is internally lined with μ-metal in order to shield the region from the earth's magnetic field. The laser enters the region through a ZnSe window, intersecting the beam initially at approximately ninety degrees and then reflecting off the mirror to intersect the beam a second time at an angle controlled by the setting of the stage. The intersection angle is measured with respect to the beam axis, with zero degrees representing laser propagation directly into the beam. The angle of intersection is given by

$$\theta_{Int} = 90 - 2(\theta_{stage} - \theta_{perp}) \tag{2.1}$$

Reproduced with permission of the copyright owner. Further reproduction prohibited without permission.

where θ_{Stage} is the reading of the rotation stage, which per se has no significance since it contains an arbitrary offset, and θ_{Perp} is the reading of the rotation stage at which the reflected laser beam intersects the beam at exactly ninety degrees. Figure 2.6 shows an example of a RESIS optical scan for helium n=9 and L=3 to n=17 and L=4, in units of stage angle. The value of θ_{Perp} must be determined carefully by calibration measurements in order to convert the recorded stage angle reading to an actual intersection angle.

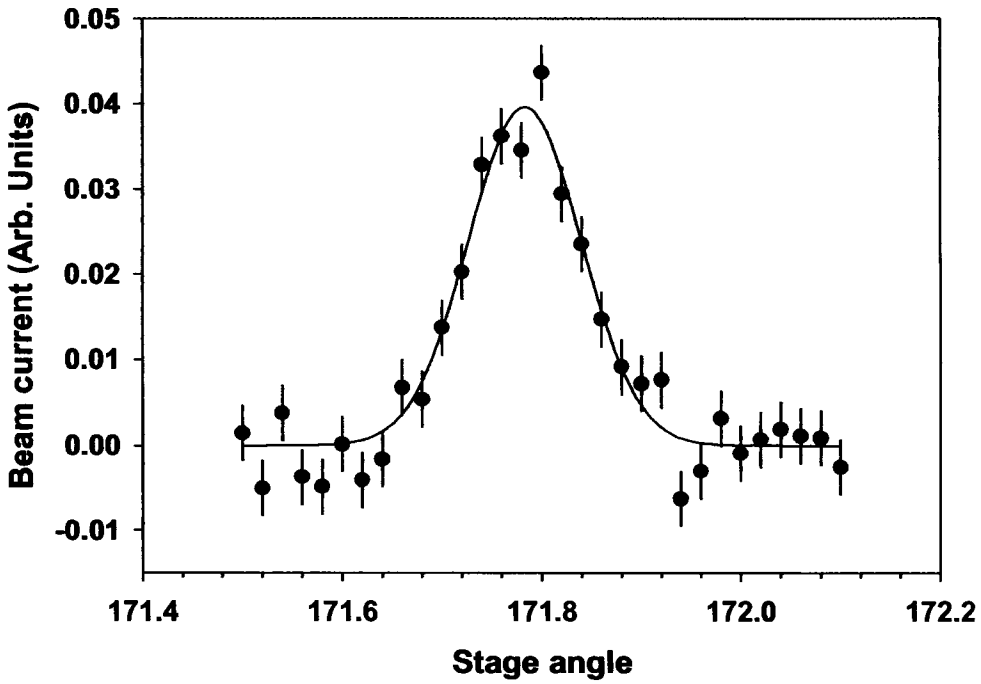

Figure 2.6: The ion beam current created by the helium n=9, L=3 to n=17, L=4 transition is plotted versus the recorded stage angle corresponding to the angle of intersection of the CO_2 laser with the He^+ beam.

Calibration of this system was performed by inducing transitions in the helium atom whose frequencies have been calculated to high precision. The speed of the

Reproduced with permission of the copyright owner. Further reproduction prohibited without permission.

helium beam at 9.5 keV is an order of magnitude faster than the barium beam and as a result these transitions can be measured with multiple CO_2 laser lines at different Doppler-tuned angles. Numerous observations of these helium transitions can be fit with unique values of β and θ_{Perp} to the following relation, which translates the stage angle to a frequency,

$$\nu' = \frac{\nu_L}{\sqrt{1-\beta^2}}(1 + \beta \sin(2(\theta_{Stage} - \theta_{Perp}))) \tag{2.2}$$

where ν' is the transition frequency, ν_L is the frequency of the laser line, and $\beta = v/c$. The frequencies of the CO_2 laser lines, ν_L, are taken from a standard reference [46], and are manually maintained within 10 MHz of the center of the gain profile. Listed in Table 2.1 are the helium transition frequencies, obtained from the calculations of Drake [47]. Also given are the stage angles at which these transitions were observed, the CO_2 line used in the observation, the stage angles predicted from the fit to Eq. (2.2), and the difference of the observed angle from that predicted by the best fit. The difference of the fit from the observed angles has a root mean square of 0.034 degrees.

The calibration procedure was repeated following two separate data runs measuring the barium RESIS transitions, and consistent results were found in the two calibrations. However, it was observed that the scatter in the observed helium resonance angular positions was somewhat larger than the statistical errors obtained in fits of the resonance lines. The limiting error in the calibration appears to be the pointing stability of the helium beam. This was collimated to a full width of about 0.20 degrees. It appears that variations in the average angular position of the he-

Reproduced with permission of the copyright owner. Further reproduction prohibited without permission.

Table 2.1: Helium calibration transitions listed with the calculated frequency, the laser frequency used, the observed stage angle, the fitted angle predicted from Eq. (2.2), and difference of the observed from the fit. Standard spectroscopic notation is used here for the angular momentum states of helium.

nL-n'L'	Actual (cm^{-1})	Laser	Laser freq. (cm^{-1})	stage angle (°)	from fit (°)	obs - fit (°)
10F-30G	975.4016	10R(22)	977.2139	155.880(17)	155.823	0.057
10F-30G	975.4016	10R(20)	975.9304	176.552(5)	176.603	-0.051
10F-30G	975.4016	10R(20)	975.9304	176.580(4)	176.603	-0.023
10F-30G	975.4016	10R(18)	974.6219	193.914(11)	193.967	-0.053
10F-30G	975.4016	10R(18)	974.6219	193.915(13)	193.967	-0.052
10F-29G	966.8487	10R(6)	966.2504	191.543(20)	191.509	0.034
10F-29G	966.8487	10R(8)	967.7072	171.910(5)	171.927	-0.017
10F-27G	946.8042	10P(16)	947.7420	170.552(8)	170.493	0.059
10F-27G	946.8042	10P(18)	945.9802	194.963(5)	194.904	0.058
10G-27H	946.7372	10P(16)	947.7420	169.511(3)	169.481	0.030
10G-27H	946.7372	10P(18)	945.9802	193.902(17)	193.934	-0.032
9G-17H	979.9665	10R(18)	974.6219	188.091(8)	188.080	0.011
9G-17H	979.9665	10R(20)	975.9304	170.543(9)	170.555	-0.012
9G-20H	1080.3235	9R(20)	1078.5906	206.268(18)	206.306	-0.039
9G-20H	1080.3235	9R(24)	1081.0874	174.420(6)	174.420	0.000
9F-17G	975.0555	10R(18)	974.6219	189.284(8)	189.261	0.023
9F-17G	975.0555	10R(20)	975.9304	171.818(8)	171.834	-0.016
9F-20G	1080.4139	9R(24)	1081.0874	175.525(5)	175.534	-0.009
9F-20G	1080.4139	9R(24)	1081.0874	175.491(9)	175.534	-0.043
9F-20G	1080.4139	9R(20)	1078.5906	207.884(22)	207.869	0.015
2nd run						
10F-30G	975.4016	10R(22)	977.2139	155.789(14)	155.783	0.0058
10F-30G	975.4016	10R(22)	977.2139	155.775(9)	155.783	-0.0082
10F-30G	975.4016	10R(20)	975.9304	176.6462(5)	176.579	0.0669
10F-30G	975.4016	10R(20)	975.9304	176.630(5)	176.579	0.0509
10F-30G	975.4016	10R(18)	974.6219	193.948(4)	193.951	-0.0027
10F-30G	975.4016	10R(18)	974.6219	193.963(5)	193.951	0.0124
9F-17G	975.0555	10R(18)	974.6219	189.227(10)	189.243	-0.016
9F-17G	975.0555	10R(18)	974.6219	189.245(3)	189.243	0.0016
9F-17G	975.0555	10R(20)	975.9304	171.783(3)	171.807	-0.0241
9F-20G	1080.4139	9R(24)	1081.0874	175.491(4)	175.509	-0.0186
9F-20G	1080.4139	9R(20)	1078.5906	207.856(4)	207.864	-0.0079

Reproduced with permission of the copyright owner. Further reproduction prohibited without permission.

lium beam, within this 0.20 degrees window are responsible for the 0.034 degrees rms scatter in the calibration fit. Examination of the time correlation of the fit residuals indicates that the pointing stability error is approximately random, so we attach this statistical error to the best value of θ_{Perp} determined from the calibration fits. The best values of θ_{Perp} and β for the helium calibration runs were found to be

$$\beta_{He} = 0.0022516(12)$$

$$\theta_{Perp} = 183.587(34).$$

The fitted value of β_{He} corresponds to a kinetic energy of 9.449(13) keV, in approximate agreement with the nominal 9.50 keV acceleration voltage. The value of θ_{Perp} is the same for all of the beams. Note that any adjustment of the CO_2 laser or beamline position will alter the value of θ_{Perp} and therefore a calibration run must be repeated.

The acceleration voltage of the ion source remains the same for all the ions. Thus the speed of the a beam is simply the square root of the mass ratio of the beam mass to helium times the speed of the helium beam. The mass of the $^{138}Ba^{+}$ ion is 137.9050 a.m.u. and the He^{+} ion has a mass of 4.002055 a.m.u. giving, β_{Ba}=0.0003836(21). This was used to convert the fitted stage angle positions to the Doppler shifted frequencies. Because the mass resolution of our velocity filter is Δm/m=0.04, for the case of barium, all ions are present in the ion beam at their natural abundance. However, because of the different speeds due to the different masses, the RESIS signals are partially mass resolved. A partially resolved barium line is given in Fig. 2.7 with a simulated line. The simulated line shape is a composite of four gaussian peaks for each of the naturally occurring isotopes. The amplitude of each of gaussian is

Reproduced with permission of the copyright owner. Further reproduction prohibited without permission.

directly proportional to the percent of abundance and the width is determined by the best fit to the measured line. The vertical lines in Fig. 2.7 illustrate where the line center occurs for each of the isotopes. This center varies only as a result of the mass, and therefore velocity, of each of the respective isotopes exiting the velocity filter. Simulations show that the center of the composite RESIS signal is very close to the position expected for a pure ^{138}Ba beam, the most abundant isotope (72 percent).

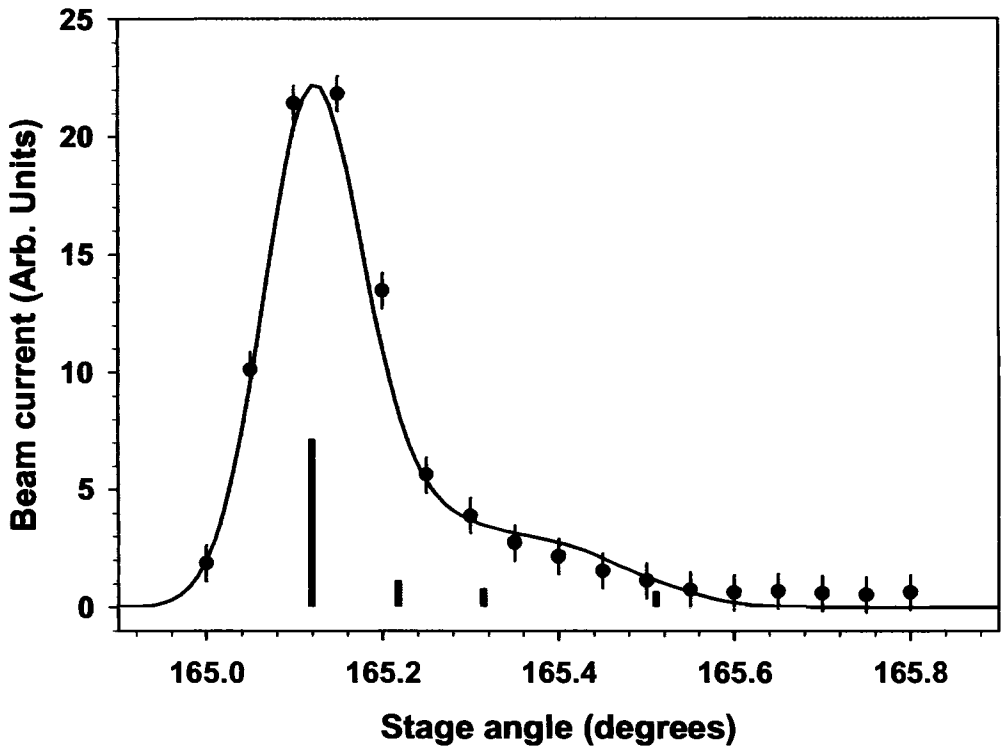

Figure 2.7: The partially mass resolved barium optical RESIS signal for n=9, L=6, and K=5.5 to n=17, L=7, and K=6.5 is plotted versus stage angle. The stick diagram indicates the centers for the four naturally occurring isotopes. The solid line is a simulation consisting of four gaussian peaks with amplitude and center corresponding the the abundance and velocity of the respective isotopes.

Microwave measurements are more precise measurements of the fine structure within a principle quantum state. These measurements are insensitive to the system-

Reproduced with permission of the copyright owner. Further reproduction prohibited without permission.

atics from the determination of θ_{Perp} and β in the optical measurements. Microwave transitions are obtained in an off-axis coaxial transmission region. The microwave frequency is produced by an HP microwave generator and is modulated at 300 Hz and is terminated in a 50 Ω load. Measurements are performed with the microwave field co-propagating and counter-propagating in order to average out the Doppler shift due to the speed of the beam. The transit time, T, of the beam through the region determines the linewidth, 1/T, of the transition. The microwave region is shielded from motional fields due to the earth's magnetic field by two layers of μ-metal. Stray DC electric fields can build up in the microwave region, causing a Stark shift in the signal. This systematic effect will be discussed further in the following chapters.

In order to set up for a microwave scan both CO_2 lasers must be precisely on the same transition. This is done by performing a "dip scan", as seen in fig. 2.8 for the case of n=9, L=7 to n=20, L=8 transition of magnesium. First the optical spectra must be obtained, then the downstream laser interaction region (LIR) is set at the peak of one of the optical transitions. This whole process is conducted while optically chopping the second laser for reference in the lock-in detection of the ion beam current. Then both lasers are optimized on the same transition by scanning through the same transition in the upstream LIR while the second laser remains on the optical signal peak. The 1 mV offset here is the peak optical signal from the second LIR. The dip in signal results from the equalization of the population by the first laser between the n=9, L=7 and n=20, L=8 levels, leaving the effect of the second laser to be zero. The first, or upstream, LIR is then set to the angle corresponding to the minimum

Reproduced with permission of the copyright owner. Further reproduction prohibited without permission.

signal in the "dip scan". This assures the peak excitation of the same transition in both LIRs, which maximizes the possible microwave signal.

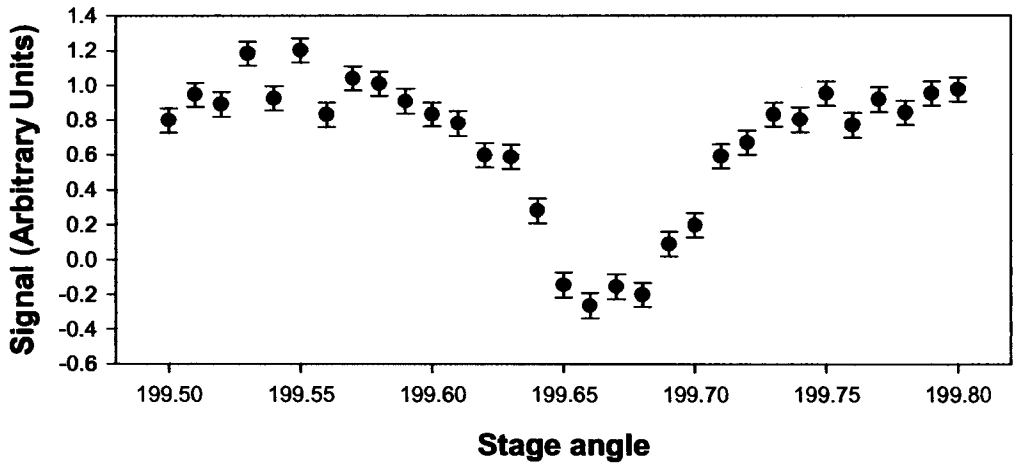

Figure 2.8: The ion beam current, referenced to the second of two doppler-tuned CO_2 lasers, is plotted versus the stage angle of the first laser for the Mg n=9, L=7 to n=20, L=8 transition. The dip in the signal corresponds to the first CO_2 laser saturating the transition, resulting in a zero contribution to the signal from the second laser. This process ensures that both lasers are optimally set to the same transition.

Once the laser transitions are set appropriately, the microwave field in the region has to be introduced with the necessary power in order to saturate the transition. The microwave power should not be above the saturation point, because this could produce broadening and shifts of the transition. Once a microwave transition is observed, a scan of microwave power can be conducted to assure that the settings are correct. An example of a saturation curve is given in Fig. 2.9 of the Ba n=20, L=7 to n=20, L=8 transition. The information from such a saturation curve is valuable when addressing the systematic error of AC Stark shifts. This will be discussed in detail later. The power necessary for saturation can be simply calculated using knowledge of the beam energy and the z matrix elements for the transitions. Once the saturation power is

Reproduced with permission of the copyright owner. Further reproduction prohibited without permission.

obtained for one transition, it can be easily scaled to the appropriate value for all other transitions.

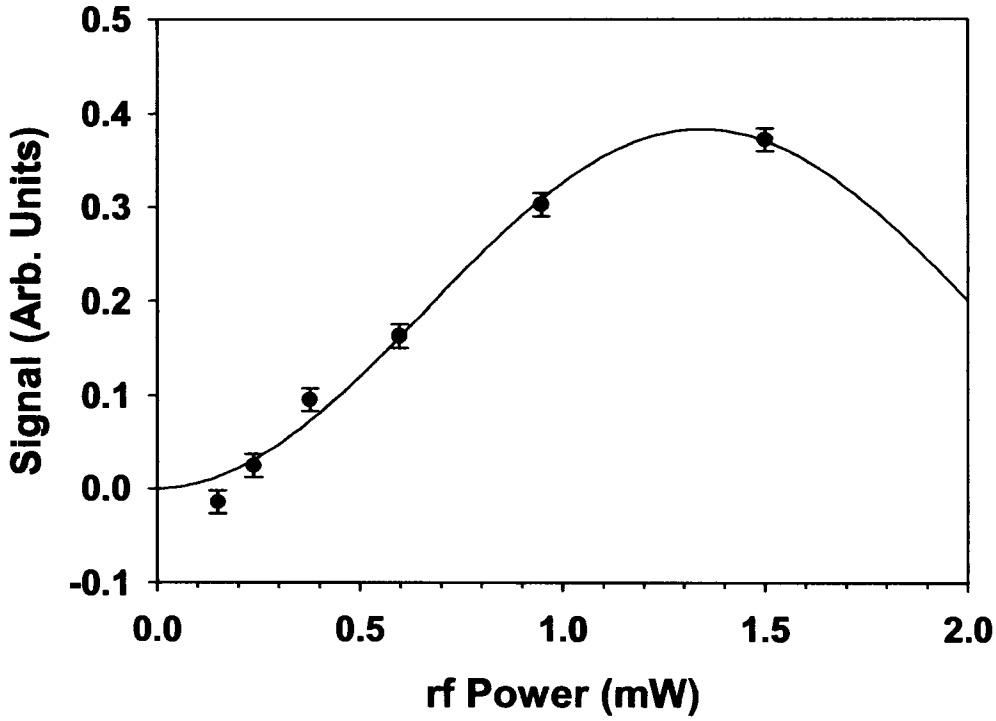

Figure 2.9: The signal on the barium n=17, L=8 to n=17, L=10 microwave transition observed in the PLJ rf region is plotted versus the rf electric field power. The smooth curve is a $sin^2(x)$ fit to the data, which can be used to determine the AC Stark shifts as discussed in the text.

Two different microwave regions were used in this work. Both regions used are 50 Ω eccentric coaxial transmission regions for propagation of TEM00 modes. The regions were constructed out of non-magnetic stainless steel but have different geometries and therefore different characteristics. Figure 2.10 shows schematics of both regions with the respective names of RAK and PLJ in reference to the students, Robert A. Komara and Phillip L. Jacobson, who constructed them. The details of these two regions will be discussed here.

Reproduced with permission of the copyright owner. Further reproduction prohibited without permission.

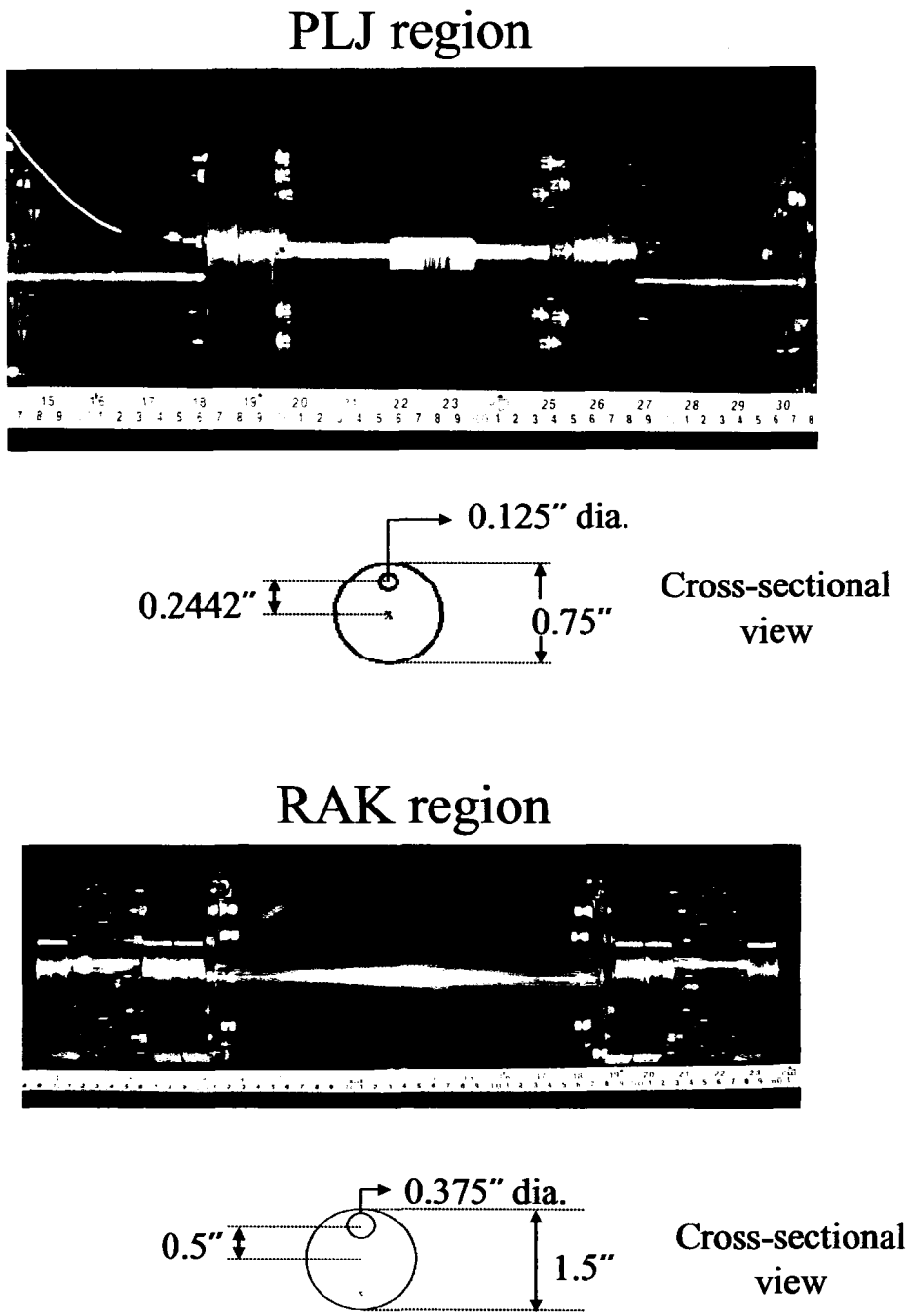

Figure 2.10: The two rf regions used in this study are pictured here with a schematic of their respective cross-sections. The x in the schematic represents the ion beam position.

Reproduced with permission of the copyright owner. Further reproduction prohibited without permission.

The RAK region is a coaxial transmission line with both the outer and inner conductor constructed of non-magnetic stainless steel. The length of this region is 30cm which corresponds to a 0.7 MHz linewidth for barium. The SMA feedthroughs are designed for microwave transmission and should not contribute any significant reflections. The frequency range of this region is limited to approximately 2.4 GHz, where reflections become substantial and other modes begin to propagate.

The PLJ region is also a coaxial transmission line. The frequency range of this region is limited to approximately 6 GHz, which allowed for the measurement of some transitions not accessible with the RAK region. The length of this region is 20cm which unfortunately leads to a larger linewidth. This region has a much smaller diameter. As a result, alignment of the beam through the region becomes more critical. DC electric fields can develop more severely in a narrower region due to accumulation of stray charge on the surfaces. Even in light of this, no significant difference was observed in measurements with the two regions of different geometry.

The final systematic effect to be discussed here is that of the AC Stark shifts. These shifts are due to the AC electric field of the rf which is driving the transition. The only transitions affected by this systematic effect are the two-photon transitions, which require higher powers for transitions through an off-resonance intermediate state. A state "a" is shifted by

$$\sum_k \left(\frac{V_{ak}^2}{E_a - E_k + \nu} + \frac{V_{ak}^2}{E_a - E_k - \nu} \right), \tag{2.3}$$

where ν is the photon energy, V is the matrix element of $eE_{rf} \langle a|z|k \rangle / 2h$, and the sum is over all states with non-zero matrix elements. Only states of similar n will

Reproduced with permission of the copyright owner. Further reproduction prohibited without permission.

contribute significantly because the remaining terms have such large energy denominators in comparison. These AC Stark shifts can be calculated by use of Eq.(2.3). The matrix elements involved depend on m_J, and so the average over all the m states is used assuming equal populations of all m states. Experimentally measured energy differences are used in this calculation. Finally, what is needed is the electric field of the rf felt by the atoms, but only the transmitted power through the region is known. The method of extracting the rf electric field from knowledge of the transmitted power is described in detail below.

The value of the rf electric field can be obtained from a saturation curve, as shown in Fig. 2.9. The saturation curve is fit to the expected

$$C \sin^2 (BP_{rf}), \tag{2.4}$$

where

$$\begin{aligned} B &= 2\pi V_{eff} T / P_{rf}, \\ V_{eff} &= \frac{V_{ak} V_{kl}}{E_a - E_k - \nu}, \\ V_{ak} &= eE_{rf} \langle a|z|k\rangle / 2h, \end{aligned} \tag{2.5}$$

the variable of the fit P_{rf} is the transmitted power, and T is the transit time through the rf region. For the case of Ba n=17, L=8 to 10 in the PLJ region, shown in Fig. 2.9, the fit to $\sin^2(BP_{rf})$ finds the parameter B to be 1.15(11) $(\text{mW})^{-1}$. The microwave scans for this transition were taken at a transmitted power of 1.5 mW, and the transit time through the PLJ region is 1.74μs giving a V_{eff} of 0.158(14) MHz. Now using Eq.(2.5), and the experimental energies we find a V^2 of 44(4) $(\text{MHz})^2$,

Reproduced with permission of the copyright owner. Further reproduction prohibited without permission.

which corresponds to an rf electric field of 0.022(2) V/cm. This V^2 value is then substituted into Eq.(2.3) to find the AC shift for the Ba n=17, L=8 to 10 transition of 0.054(5) MHz. This can also be calculated without a fit to the saturation curve, if one assumes that the data is taken at the peak of the saturation curve. Then it can be seen from Eq.(2.4) that V_{eff} is simply 1/(4T). This method leads to V_{eff}=0.144 MHz for the case in discussion here, which results in a AC shift that is consistent with the previous results. Once V_{eff}, or in other words the rf electric field, is known for each rf region, V^2 can be determined for any state and the AC shifts calculated. Multiple saturation curves were observed on several transitions and were found to be in good agreement with the ideal 1/(4T) calculation, which is used as the final AC Stark shift correction. The error bars on the AC shift reflect the variation found by the fitting of the observed saturation curves. The calculated AC stark shift for the two-photon transitions in this work for each region are listed in Table 2.2.

Table 2.2: AC Stark shifts are given in MHz for each of the 2-photon transitions in both of the rf regions used in this study.

	PLJ (MHz)	RAK (MHz)
Mg 17,9 - 17,11	0.105(20)	0.070
Ba 17,8 - 17,10	0.049(5)	0.033(10)
Ba 20,9 - 20,11	0.044(6)	0.027

2.4 Detection

A high electric field region is produced to Stark ionize high-n Rydberg states, while also boosting their energy to distinguish them from collisionally produced ions created

Reproduced with permission of the copyright owner. Further reproduction prohibited without permission.

along the beamline. These energetically boosted ions are then deflected onto a channel electron multiplier (CEM) plate by a set of vertical and horizontal electric field plates. The physical apparatus was constructed by Jacobson [45]. The longitudinal Stark ionizing field is produced between two plates where the beam passes through an aperture in the center. The gap between plates is 0.8 cm and a series of stripping potentials were used for the different upper states ranging from -600 V for n=30 to 6500 V for n=17 states. The CEM current is sent through a 10^8 V/A electrometer. An additional low pass filter was inserted before the lock-in to further reduce background noise.

The reference for optical and microwave RESIS is implemented in two different ways. (1) The optical RESIS signal is modulated by chopping the CO_2 laser with a 50/50 rotating chopper wheel for reference in lock-in detection. (2) For the microwave RESIS signal detection, the microwave frequency is modulated by the HP microwave generator itself. In the RESIS microwave technique neither CO_2 laser is modulated. These respective modulations enable lock-in amplifier detection on an SRS detector of the CEM current due to the either laser or microwave frequency.

Reproduced with permission of the copyright owner. Further reproduction prohibited without permission.

Chapter 3

Measurements

Resonant Excitation Stark Ionization Spectroscopy microwave techniques were used to measure the high-L fine structure of the n=17 and 20 upper states of magnesium and barium optical transitions. Each microwave scan consisted of small steps either 0.1 or 0.2 MHz and each point collected was averaged over 60 seconds. The microwave region is used in two physical orientations where the side labeled A is upstream and side B is downstream or the reverse orientation. This allows an average of the signals to remove any asymmetries, which should be small, in the construction of the coaxial microwave region. Alternatively, the use of a second rf region would also test for asymmetries or construction defects. Two types of scans were completed for each transition and orientation of the rf region consisting of co- and counter-propagating microwave fields with respect to the ion beam. The centers of the two scans of different microwave propagation are averaged in order to remove any doppler effects. The notation for each of these scans is given in Table 3.1.

The predicted microwave line shape is discussed in detail by Hessels [48]. The

Reproduced with permission of the copyright owner. Further reproduction prohibited without permission.

Table 3.1: The configurations for all the types of microwave scans with the corresponding notation.

Notation	Upstream Side	Microwave Propagation Direction
PLJA Co	A	Co-propagating
PLJA Counter	A	Counter-propagating
PLJB Co	B	Co-propagating
PLJB Counter	B	Counter-propagating
RAKA Co	A	Co-propagating
RAKA Counter	A	Counter-propagating

data from each scan will be fit to the following function,

$$y = C * \sin^2(\pi T(f - f_0)) / (\pi T(f - f_0))^2 \tag{3.1}$$

where f_0 is the line center in MHz and T is the transit time through the rf region in μs. An unweighted fit to the data is performed for each transition. The uncertainty of the line center is determined by the RMS deviation of the data from the fit.

The observed line shape is well described by this fit. The counter-propagating microwave RESIS signals for barium n=17, L=8, K=7.5 to n=17, L=9, K=8.5 and magnesium n=17 L=6 to n=17 L=7 are shown in figures 3.1 and 3.2 with the fitted line shape. The error on each point is determined by the scatter observed in the Y channel of the lock-in detector, which nominally contains zero signal. This method of assigning error may be an underestimate of the true error. One other possible source of error would be fluctuations in the ion beam current which are hard to monitor.

The presence of DC electric fields causes a shift in the observed resonance. The accumulation of charge within the interaction region can cause Stark shifting of the energy levels. Although attempts are made to reduce any stray DC electric fields, their presence cannot be eliminated. The rate at which the Stark shifting occurs can

Reproduced with permission of the copyright owner. Further reproduction prohibited without permission.

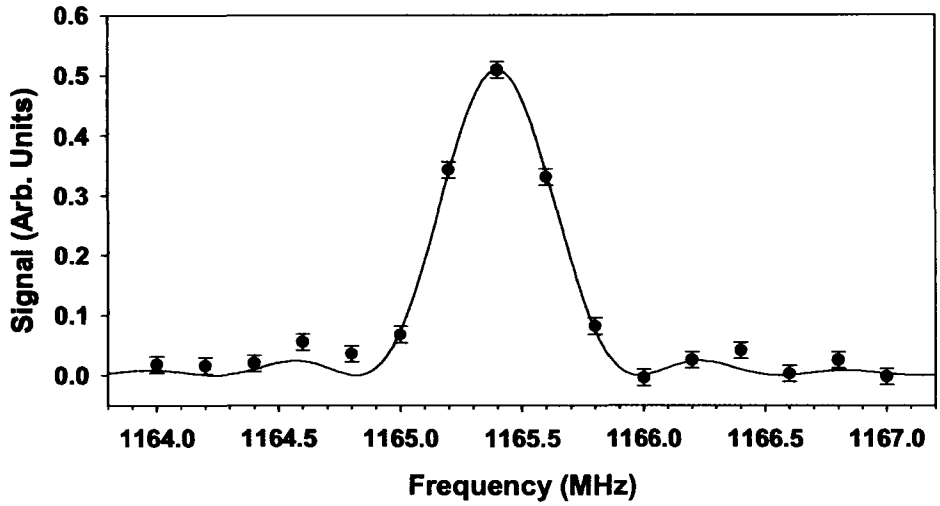

Figure 3.1: Measured ion current resulting from the barium n=17, L=8, K=7.5 excitation to the n=17, L=9, K=8.5 state for a counter-propagating microwave field versus frequency. The solid line represents the fit to the lineshape as discussed in the text.

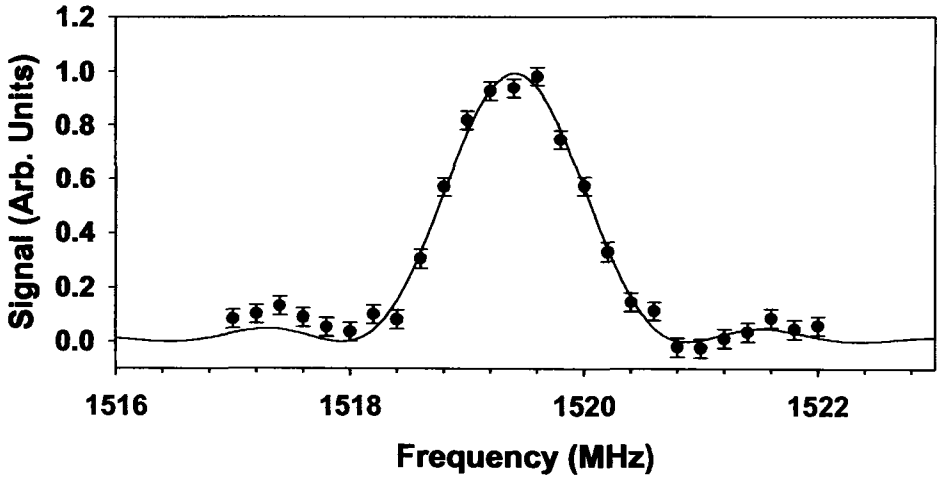

Figure 3.2: Measured ion current resulting from the magnesium n=17, L=6 excitation to the n=17, L=7 state for a counter-propagating microwave field versus frequency. The solid line represents the fit to the lineshape as discussed in the text.

Reproduced with permission of the copyright owner. Further reproduction prohibited without permission.

be calculated for each state of interest. The Stark shift for an nLm level perturbed by the neighboring $L+1$ level is

$$\Delta E_{Stark}^{L+1} = \frac{e^2 E^2 \langle nLm|z|n(L+1)m\rangle^2}{\Delta E_{L,L+1}}, \tag{3.2}$$

where E is the electric field and $\Delta E_{L,L+1}$ is the fine structure energy difference between the two levels. The calculation of the Stark shift rate includes the shift of the transition of interest due to both the upper and lower perturbing states. Assuming equal populations of all the m states an average of the Stark shift rate is taken.

States of higher n and L are more sensitive to Stark shifts by stray fields. The z matrix element squared can be written as

$$\langle nLm|z|n(L+1)m\rangle^2 = \left(\frac{3n}{2}\right)^2 (n^2-(L+1)^2)\left[\frac{(L+1)^2-m^2}{(2L+3)(2L+1)}\right], \tag{3.3}$$

which goes as n^4. Now if one assumes that the fine structure energy difference is due only to the adiabatic dipole energy then the energy denominator can be substituted with $\frac{1}{2}\alpha_d \langle r^{-4}\rangle$. The $\langle r^{-4}\rangle$ has a closed analytical form which scales with n^{-3} roughly. Combining these two factors shows that the Stark shift rate depends on n^7, which will result in greater Stark shift sensitivity in the higher-n levels. A similar look at the L dependence also indicates larger Stark shift rates for higher-L states.

The fluctuation of stray fields in the apparatus was monitored by observation of a Stark sensitive transition. A high n and L state was observed at the beginning and end of a set of data, spanning the course of at most 24 hours. The measurement of the Stark sensitive line did not show any evidence of a systematic shift, indicating that the field within the apparatus did not change to within 0.02(2) V/cm. This by no

Reproduced with permission of the copyright owner. Further reproduction prohibited without permission.

means indicates that the field is zero in the system, but that the field is constant. The amount of field present will be addressed for each system in the respective sections.

3.1 Magnesium n=17 Fine Structure

Given in Table 3.2 is a list of all the observations obtained in n=17 neutral magnesium and Table 3.3 lists the n=20 observations. The type of microwave scan, the date, the lab book page number, the corresponding optical line, and line center, and T a parameter of the fit is also given. The parameter T, from the fit gives the fitted transit time and hence the linewidth, 1/T. Appendix B contains one type of scan of the microwave signal versus frequency for each of the transitions measured in this study.

An asymmetry was revealed in the line shape for the series of lines in n=20 for magnesium. Two examples of this asymmetric line shape are shown in Figs. 3.3 and 3.4. The n=20 magnesium lines are much more sensitive to Stark shifts from electric fields. It is likely that this lineshape is the result of some form of an inhomogeneous electric field. Fields of this sort have been known to develop from deposition of stray charge onto surfaces as noted in previous RESIS works. Due to large Stark shift rates the Stark shifts for the n=20 magnesium energy levels are greater than the line width and so complicated line shapes are not surprising. The exact nature of these line shapes is as of yet, not fully understood. The magnesium n=20 measured energy intervals will therefore not be used in the polarization analysis, except in order to determine the magnitude of the stray electric fields. The centroid of the

Reproduced with permission of the copyright owner. Further reproduction prohibited without permission.

Table 3.2: All of the observed magnesium n=17 lines are listed with the corresponding type of microwave scan, the lab book page number and date, the optical line used to access the microwave transition, the observed frequency, and the parameter T, which is related to the line width.

n=17 L - L'	rf region	page #	date	Optical line	frequency (MHz)	T (μs)
6 - 7	RAK co	10_092b	10/4/2005	9,6 -17,7	1522.201(12)	0.967(28)
6 - 7	RAK counter	10_92	10/4/2005	9,6 -17,7	1519.420(12)	1.006(28)
6 - 7	PLJA co	12_017	4/26/2006	9,6 -17,7	1522.229(20)	0.672(22)
6 - 7	PLJA counter	12_017d	4/26/2006	9,6 -17,7	1519.406(16)	0.678(17)
6 - 7	PLJB co	12_033c	5/3/2006	9,6 -17,7	1522.224(15)	0.750(22)
6 - 7	PLJB counter	12_033b	5/3/2006	9,6 -17,7	1519.375(13)	0.756(17)
7 - 8	RAK co	10_090	10/4/2005	9,7 - 17,8	670.208(12)	0.994(28)
7 - 8	RAK counter	10_090b	10/4/2005	9,7 - 17,8	668.963(13)	0.967(28)
7 - 8	PLJA co	12_017b	4/26/2006	9,6 -17,7	670.265(35)	0.733(44)
7 - 8	PLJA co	12_017b	4/26/2006	9,6 -17,7	670.243(42)	0.683(44)
7 - 8	PLJA counter	12_017c	4/26/2006	9,6 -17,7	668.944(28)	0.667(33)
7 - 8	PLJB co	12_034	5/3/2006	9,6 -17,7	670.218(22)	0.767(28)
7 - 8	PLJB counter	12_033	5/3/2006	9,6 -17,7	668.921(16)	0.750(22)
8 - 9	RAK co	10_089b	10/4/2005	9,7 - 17,8	324.367(14)	0.956(22)
8 - 9	RAK counter	10_090c	10/4/2005	9,7 - 17,8	323.791(22)	0.928(44)
8 - 9	PLJA co	12_020c	4/26/2006	9,8 - 17,9	324.315(19)	0.683(22)
8 - 9	PLJA counter	12_018	4/26/2006	9,8 - 17,9	323.660(29)	0.706(33)
8 - 9	PLJB co	12_031b	5/3/2006	9,8 - 17,9	324.322(12)	0.772(11)
8 - 9	PLJB counter	12_032c	5/3/2006	9,8 - 17,9	323.809(14)	0.772(22)
9 - 10	RAK co	10_093	10/4/2005	9,8 - 17,9	168.999(30)	0.950(67)
9 - 10	PLJA co	12_020b	4/26/2006	9,8 - 17,9	168.907(21)	0.667(22)
9 - 10	PLJA counter	12_018b	4/26/2006	9,8 - 17,9	168.621(22)	0.683(22)
9 - 10	PLJB co	12_031	5/3/2006	9,8 - 17,9	168.932(24)	0.744(28)
9 - 10	PLJB counter	12_032b	5/3/2006	9,8 - 17,9	168.712(21)	0.767(28)
*9 - 11	PLJA co	12_020	4/26/2006	9,8 - 17,9	131.243(28)	0.933(61)
*9 - 11	PLJA counter	12_019b	4/26/2006	9,8 - 17,9	131.013(30)	0.822(50)
*9 - 11	PLJB co	12_031c	5/3/2006	9,8 - 17,9	131.313(12)	1.456(67)
*9 - 11	PLJB counter	12_032	5/3/2006	9,8 - 17,9	131.087(15)	1.472(78)

Reproduced with permission of the copyright owner. Further reproduction prohibited without permission.

Table 3.3: All of the observations of two magnesium n=20 lines are listed with the corresponding type of microwave scan, the lab book page number and date, the optical line used to access the microwave transition, the observed frequency is the centroid of the observed lineshape.

n=20 L - L'	rf region	page #	date	Optical line	Centroid (MHz)
7 - 8	PLJB co	12_030b	5/3/2006	9,7 - 20, 8	415.6(1)
7 - 8	PLJA co	12_012	4/26/2006	9,7 - 20, 8	415.6(1)
7 - 8	PLJA co	12_016	4/26/2006	9,7 - 20, 8	415.6(1)
7 - 8	PLJA co	12_021c	4/26/2006	9,7 - 20, 8	415.8(2)
7 - 8	PLJB counter	12_030	5/3/2006	9,7 - 20, 8	415.0(1)
7 - 8	PLJA counter	12_011	4/26/2006	9,7 - 20, 8	414.8(2)
8 - 9	PLJB co	12_030c	5/3/2006	9,7 - 20, 8	200.7(2)
8 - 9	PLJB co	12_034b	5/3/2006	9,7 - 20, 8	201.0(1)
8 - 9	PLJA co	12_021b	4/26/2006	9,7 - 20, 8	201.2(2)
8 - 9	PLJB counter	12_028	5/3/2006	9,7 - 20, 8	200.8(2)
8 - 9	PLJB counter	12_028b	5/3/2006	9,7 - 20, 8	201.0(1)
8 - 9	PLJA counter	12_028b	5/3/2006	9,7 - 20, 8	200.8(1)

lineshape is assumed to be the transition frequency with an uncertainty of 2% of the linewidth. Appendix B shows examples of each of the n=20 magnesium microwave scans observed as they may be of interest for future studies.

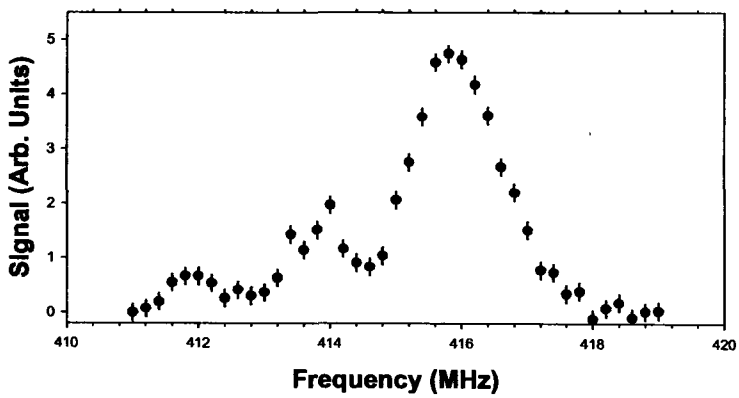

Figure 3.3: Measured ion current resulting from the magnesium n=20, L=7 excitation to the n=20, L=8 state for a co-propagating microwave field versus frequency.

Reproduced with permission of the copyright owner. Further reproduction prohibited without permission.

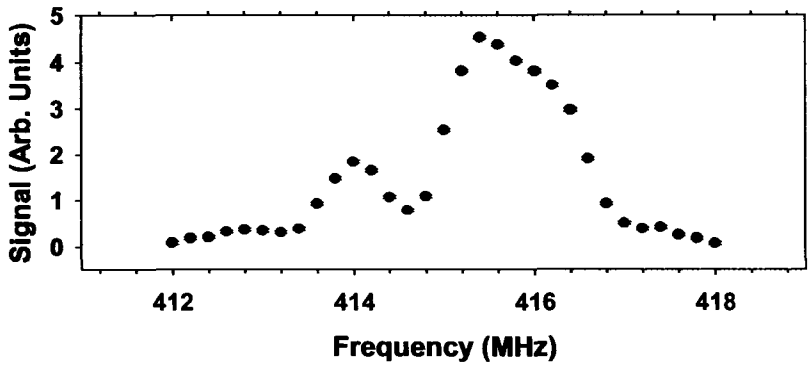

Figure 3.4: Measured ion current resulting from the magnesium n=20, L=7 excitation to the n=20, L=8 state for a counter-propagating microwave field versus frequency.

One important systematic must be addressed here; Stark shifts due to stray DC electric fields. As a result of the higher-L states sensitivity to electric fields, the polarization plot as discussed in Chapter 1.3, will display significant downward curvature near x=0 if a field is present. Figure 3.5 shows the polarization plots, the measured intervals normalized to $\Delta \langle r^{-4} \rangle$ versus $\Delta \langle r^{-6} \rangle / \Delta \langle r^{-4} \rangle$, for three separate days. The second order energies and relativistic effects have been removed as in Section 1.3 for helium. In the interest of simplicity a more detailed discussion will be delayed until Chapter 4. It can be seen in fig. 3.5 that the measurements are all consistent with the exception of one day. These inconsistent measurements taken on Day 1 show the downward curvature pattern, which is characteristic of the presence of an electric field. The measurements taken in this day can be brought into agreement by applying a Stark shift correction due to a field of 0.035 V/cm. This is a small amount of stray field based on previous observations [20]. This day by day comparison does not lead to an evaluation of the total existing stray field, but does apply a correction

Reproduced with permission of the copyright owner. Further reproduction prohibited without permission.

in order to treat all the data as if the measurements were obtained in an identical environment.

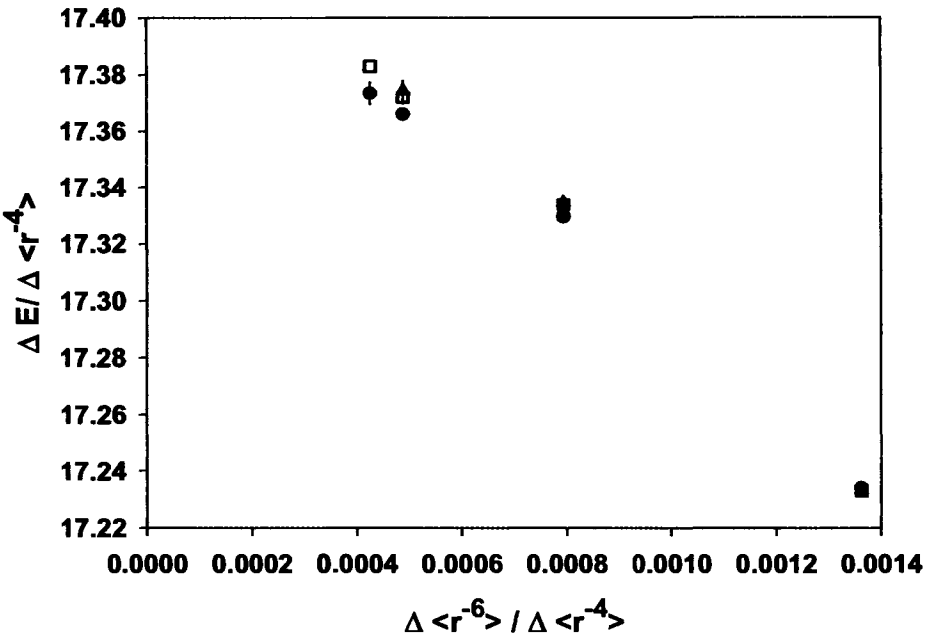

Figure 3.5: The Mg n=17 fine structure intervals observed on three separate days are normalized to $\Delta < r^{-4} >$ and plotted versus $\Delta < r^{-6} > / \Delta < r^{-4} >$. The three types of points represent the three separate sets of data. The downward curvature for the day represented by solid points is an indication of a larger stray electric field presence on that day.

In order to determine the overall effect of stray DC electric fields, the use of the n=20 measurements can illuminate the situation, because of their increased sensitivity. The Stark shift rates increase not only with L, but go as n^7 causing the heightened sensitivity to electric fields for the higher n states, which is reflected in the calculated Stark shift rates given in Tables 3.4. The electric field was shown not to change significantly throughout the span of a day, and a variation of only 0.035 V/cm was observed from one day to the next on one occasion, which has been accounted for in

Reproduced with permission of the copyright owner. Further reproduction prohibited without permission.

both the n=17 and 20 observations when necessary. Therefore, it seems justifiable to assume now that the same field is continuously present in this Stark field corrected data. The normalized intervals of the same L for n=17 and 20 should be consistent, creating an overall linear plot, however, it can be seen in fig. 3.6 that the n=20 data (triangles) does not lie on the same line with the n=17 data (circles). The calculated Stark shift rates can be used to find the amount of field present which results in a final polarization plot that is linear. This is done by fitting the data to

$$y = A_4 + A_6 \frac{\Delta \langle r^{-6} \rangle}{\Delta \langle r^{-4} \rangle} + A_E \frac{\Delta \kappa}{\Delta \langle r^{-4} \rangle}, \tag{3.4}$$

where A_E is the stray electric field squared. The fitted parameters were found to be 17.51(1), -197(8), and 0.008(2) respectively. The n=17 and 20 normalized intervals lie on the same line, as shown by open circles (n=17) and open triangles (n=20) in fig. 3.6, when a field of 0.089(11)V/cm is present. This is certainly a plausible value for the electric field based on previous observation [20].

The final Doppler-free transition frequencies can be found now that the systematics due to stray electric fields have been determined. The weighted average of all the line centers adjusted for appropriate Stark field corrections is taken for all orientations of both rf regions. Then the straight average of the co- and counter-propagating signals determines the Doppler-free energy intervals. Table 3.4 lists all the Doppler-free energy intervals for n=17 neutral magnesium used in this study. The first error bar is the uncertainty in the fitted line center. The second error bar represents the uncertainty in the DC Stark shift correction. In addition to the measured intervals, the corresponding Stark shift rates, $\Delta\kappa(nL - n'L')$, are also listed.

Reproduced with permission of the copyright owner. Further reproduction prohibited without permission.

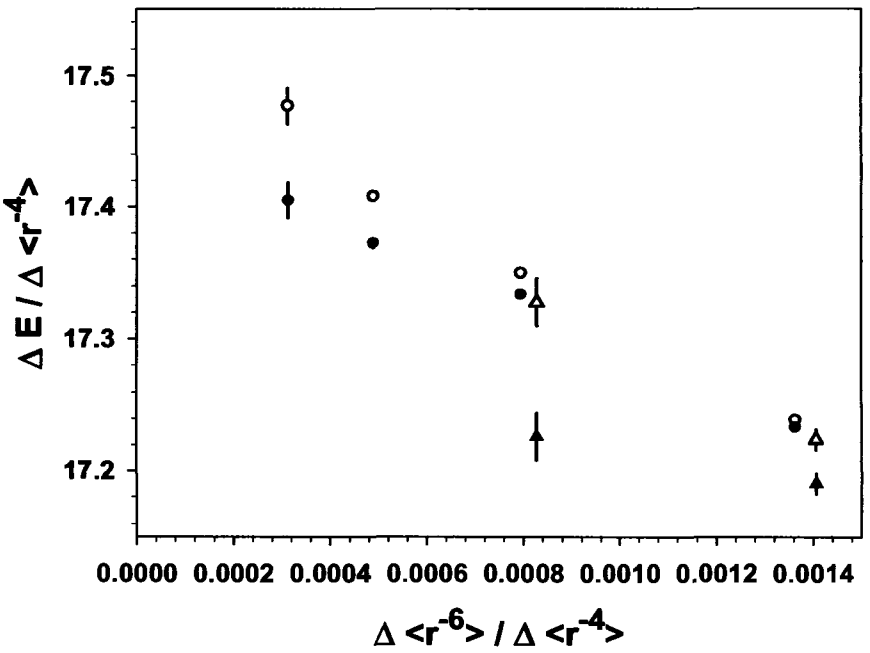

Figure 3.6: The measured magnesium fine structure intervals are normalized to $\Delta\langle r^{-4}\rangle$ are plotted versus $\Delta\langle r^{-6}\rangle / \Delta\langle r^{-4}\rangle$. The open points indicate the fine structure pattern corrected for a Stark field of 0.089(12) V/cm.

Reproduced with permission of the copyright owner. Further reproduction prohibited without permission.

Table 3.4: The final results of the fine structure measurements of magnesium n=17 and the two n=20 magnesium transitions are listed here with the Stark shift rates. The second error is due only to the uncertainty in the stray electric field.

n=17, L - L'	ΔE_{Obs} (MHz)	κ [MHz/(V/cm)^2]	$\Delta E_{E=0}$ (MHz)
6 - 7	1520.812(8)	-17.8	1520.954(8)(32)
7 - 8	669.585(13)	-27	669.801(13)(49)
8 - 9	324.067(12)	-36.8	324.363(12)(66)
9 - 10	168.826(17)	-43.2	169.172(17)(78)
*10 - 11	93.483(62)	-48.2	93.869(62)(87)
n=20, L - L'			
7 - 8	415.4(2)	-102	416.2(2)(2)
8 - 9	201.0(2)	-148	202.2(2)(3)

3.2 Barium n=17 and 20 Fine Structure

The observed transitions are fitted with a $\sin^2(\pi T(f-f_0))/(\pi T(f-f_0))^2$ line shape as discussed earlier. The line centers of each of the observed transitions is listed with the fit parameter T, the type of microwave scan, the optical line used in the RESIS technique, and the corresponding lab book page number. Examples of each of the transitions are given in Appendix B.

The presence of stray DC electric field fluctuations on the time scale of days is evaluated by comparing the n=20 data taken on three separate days. Figure 3.7 shows the polarization plot for the barium fine structure data taken on three different days. All of the polarization plots presented below have adjustments for relativistic and effective second order energies. The exact values are given in Chapter 4. Each point represents the center of gravity of the two K states for each n, L level. It can be seen that the measurements from Day 1 (open circles) are not consistent with the

Reproduced with permission of the copyright owner. Further reproduction prohibited without permission.

Table 3.5: All of the observed barium n=17 lines are listed with the corresponding type of microwave scan, the lab book page number and date, the optical line used to access the microwave transition, the observed frequency and the parameter T, which is related to the line width.

n=17 L_K - $L'_{K'}$	rf region	page #	date	optical line	frequency (MHz)	T (μs)
$6_{5.5}$ - $7_{6.5}$	PLJA co	8_110	4/14/2005	$9,6_{5.5}$ - $17,7_{6.5}$	5856.591(9)	1.411(28)
$6_{5.5}$ - $7_{6.5}$	PLJA co	8_117	4/15/2005	$9,6_{5.5}$ - $17,7_{6.5}$	5856.581(114)	1.44(20)
$6_{5.5}$ - $7_{6.5}$	PLJA counter	8_117	4/15/2005	$9,6_{5.5}$ - $17,7_{6.5}$	5852.210(55)	1.22(13)
$6_{6.5}$ - $7_{7.5}$	PLJA co	8_104	4/11/2005	$9,6_{6.5}$ - $17,7_{7.5}$	5635.522(27)	1.433(78)
$6_{6.5}$ - $7_{7.5}$	PLJA counter	8_133	4/27/2005	$9,6_{6.5}$ - $17,7_{7.5}$	5631.256(19)	1.478(56)
$6_{6.5}$ - $7_{6.5}$	PLJA co	8_114	4/15/2005	$9,6_{5.5}$ - $17,7_{6.5}$	5594.797(20)	1.100(39)
$6_{6.5}$ - $7_{6.5}$	PLJA counter	8_111	4/14/2005	$9,6_{5.5}$ - $17,7_{6.5}$	5590.654(37)	1.022(72)
$6_{6.5}$ - $7_{6.5}$	PLJA counter	8_114	4/15/2005	$9,6_{5.5}$ - $17,7_{6.5}$	5590.648(50)	0.994(94)
$6_{6.5}$ - $7_{6.5}$	PLJA counter	8_117b	4/15/2005	$9,6_{5.5}$ - $17,7_{6.5}$	5590.462(38)	1.156(89)
$7_{6.5}$ - $8_{7.5}$	PLJA co	8_115	4/15/2005	$9,6_{5.5}$ - $17,7_{6.5}$	2440.907(63)	1.71(12)
$7_{6.5}$ - $8_{7.5}$	PLJA co	8_116	4/15/2005	$9,6_{5.5}$ - $17,7_{6.5}$	2440.758(69)	1.74(13)
$7_{6.5}$ - $8_{7.5}$	PLJA counter	8_116	4/15/2005	$9,6_{5.5}$ - $17,7_{6.5}$	2438.941(23)	1.74(13)
$7_{7.5}$ - $8_{8.5}$	PLJA co	8_131	4/27/2005	$9,7_{7.5}$ - $17,8_{8.5}$	2412.199(13)	1.578(72)
$7_{7.5}$ - $8_{8.5}$	PLJA co	8_132c	4/27/2005	$9,7_{7.5}$ - $17,8_{8.5}$	2412.174(18)	1.62(10)
$7_{7.5}$ - $8_{8.5}$	PLJA counter	8_132c	4/27/2005	$9,7_{7.5}$ - $17,8_{8.5}$	2410.328(29)	1.83(19)
$8_{7.5}$ - $9_{8.5}$	PLJA co	8_121c	4/19/2005	$9,7_{6.5}$ - $17,8_{7.5}$	1166.352(17)	1.533(89)
$8_{7.5}$ - $9_{8.5}$	PLJA counter	8_121	4/19/2005	$9,7_{6.5}$ - $17,8_{7.5}$	1165.401(8)	1.722(56)
$8_{8.5}$ - $9_{9.5}$	RAK co	9_078b	6/23/2005	$9,7_{7.5}$ - $17,8_{8.5}$	1158.303(50)	1.300(78)
$8_{8.5}$ - $9_{9.5}$	PLJA co	8_127	4/22/2005	$9,7_{7.5}$ - $17,8_{8.5}$	1158.221(55)	1.77(16)
$8_{8.5}$ - $9_{9.5}$	PLJA co	8_130b	4/27/2005	$9,7_{7.5}$ - $17,8_{8.5}$	1158.196(15)	1.644(39)
$8_{8.5}$ - $9_{9.5}$	RAK counter	9_080	6/23/2005	$9,7_{7.5}$ - $17,8_{8.5}$	1157.405(51)	1.322(67)
$8_{8.5}$ - $9_{9.5}$	PLJA counter	8_132b	4/27/2005	$9,7_{7.5}$ - $17,8_{8.5}$	1157.318(30)	1.717(67)
*$8_{7.5}$ - $10_{9.5}$	RAK co	9_057b	6/7/2005	$9,7_{6.5}$ - $17,8_{7.5}$	885.440(16)	1.294(67)
*$8_{7.5}$ - $10_{9.5}$	PLJA co	8_122	4/19/2005	$9,7_{6.5}$ - $17,8_{7.5}$	885.385(38)	2.9(9)
*$8_{7.5}$ - $10_{9.5}$	RAK counter	9_056	6/7/2005	$9,7_{6.5}$ - $17,8_{7.5}$	884.766(17)	1.100(39)
*$8_{8.5}$ - $10_{10.5}$	RAK co	9_077b	6/23/2005	$9,7_{7.5}$ - $17,8_{8.5}$	879.989(14)	1.083(39)
*$8_{8.5}$ - $10_{10.5}$	RAK counter	9_053	6/7/2005	$9,7_{7.5}$ - $17,8_{8.5}$	879.355(19)	1.333(78)
*$8_{8.5}$ - $10_{10.5}$	RAK counter	9_054	6/7/2005	$9,7_{7.5}$ - $17,8_{8.5}$	879.349(17)	2.28(20)

Reproduced with permission of the copyright owner. Further reproduction prohibited without permission.

Table 3.6: All of the observed barium n=20 lines are listed with the corresponding type of microwave scan, the lab book page number and date, the optical line used to access the microwave transition, the observed frequency and the parameter T, which is related to the line width.

n=20 L_K - $L'_{K'}$	rf region	page #	date	optical line	frequency (MHz)	T (μs)
$7_{6.5}$ - $8_{7.5}$	PLJB co	12_042	5/10/2006	$9,7_{6.5}$ - $20,8_{7.5}$	1519.318(11)	1.99(10)
$7_{6.5}$ - $8_{7.5}$	PLJA counter	8_020	2/17/2006	$9,7_{6.5}$ - $20,8_{7.5}$	1518.043(25)	1.58(14)
$7_{6.5}$ - $8_{7.5}$	PLJB counter	12_044	5/10/2006	$9,7_{6.5}$ - $20,8_{7.5}$	1518.065(38)	1.64(24)
$7_{7.5}$ - $8_{8.5}$	PLJA co	8_013	2/17/2006	$9,7_{7.5}$ - $20,8_{8.5}$	1500.532(23)	1.58(13)
$7_{7.5}$ - $8_{8.5}$	PLJB co	12_039b	5/7/2006	$9,7_{7.5}$ - $20,8_{8.5}$	1500.493(63)	1.66(15)
$7_{7.5}$ - $8_{8.5}$	PLJB co	12_039b	5/7/2006	$9,7_{7.5}$ - $20,8_{8.5}$	1500.479(60)	1.61(11)
$7_{7.5}$ - $8_{8.5}$	PLJB co	12_039b	5/7/2006	$9,7_{7.5}$ - $20,8_{8.5}$	1500.585(48)	1.63(14)
$7_{7.5}$ - $8_{8.5}$	PLJA counter	8_016	2/17/2006	$9,7_{7.5}$ - $20,8_{8.5}$	1499.393(24)	1.66(15)
$7_{7.5}$ - $8_{8.5}$	PLJB counter	12_045b	5/10/2006	$9,7_{7.5}$ - $20,8_{8.5}$	1499.450(15)	1.62(9)
$7_{7.5}$ - $8_{7.5}$	PLJB co	12_042b	5/10/2006	$9,7_{6.5}$ - $20,8_{7.5}$	1492.712(33)	1.66(22)
$7_{7.5}$ - $8_{7.5}$	PLJB co	12_043	5/10/2006	$9,7_{6.5}$ - $20,8_{7.5}$	1492.655(48)	2.07(44)
$7_{7.5}$ - $8_{7.5}$	PLJB counter	12_044b	5/10/2006	$9,7_{6.5}$ - $20,8_{7.5}$	1491.578(64)	1.86(50)
$8_{7.5}$ - $9_{8.5}$	PLJB co	12_043b	5/10/2006	$9,7_{6.5}$ - $20,8_{7.5}$	728.152(15)	1.68(10)
$8_{7.5}$ - $9_{8.5}$	PLJA counter	8_019	2/17/2006	$9,7_{6.5}$ - $20,8_{7.5}$	727.424(29)	1.36(12)
$8_{7.5}$ - $9_{8.5}$	PLJB counter	12_043c	5/10/2006	$9,7_{6.5}$ - $20,8_{7.5}$	727.568(10)	2.06(9)
$8_{8.5}$ - $9_{9.5}$	PLJA co	8_014	2/17/2006	$9,7_{7.5}$ - $20,8_{8.5}$	722.645(12)	1.82(9)
$8_{8.5}$ - $9_{9.5}$	PLJB co	12_046b	5/10/2006	$9,7_{7.5}$ - $20,8_{8.5}$	722.801(12)	1.74(9)
$8_{8.5}$ - $9_{9.5}$	PLJA counter	8_015	2/17/2006	$9,7_{7.5}$ - $20,8_{8.5}$	722.047(19)	1.67(13)
$8_{8.5}$ - $9_{9.5}$	PLJB counter	12_046	5/10/2006	$9,7_{7.5}$ - $20,8_{8.5}$	722.231(12)	1.66(8)
$9_{8.5}$ - $10_{9.5}$	PLJA co	8_032	2/24/2006	9,8 - 20,9	378.481(26)	1.73(19)
$9_{8.5}$ - $10_{9.5}$	PLJA counter	8_023	2/17/2006	9,8 - 20,9	378.165(50)	1.51(25)
$9_{9.5}$ - $10_{10.5}$	PLJA co	8_032	2/24/2006	9,8 - 20,9	376.66(28)	1.51(15)
$9_{9.5}$ - $10_{10.5}$	PLJA counter	8_023	2/17/2006	9,8 - 20,9	376.452(49)	1.51(25)
*$9_{8.5}$ - $11_{10.5}$	PLJA co	8_033	2/24/2006	9,8 - 20,9	294.041(21)	2.78(36)
*$9_{8.5}$ - $11_{10.5}$	PLJA counter	8_035	2/24/2006	9,8 - 20,9	293.787(11)	3.36(28)
*$9_{9.5}$ - $11_{11.5}$	PLJA co	8_033	2/24/2006	9,8 - 20,9	292.780(21)	2.99(41)
*$9_{9.5}$ - $11_{11.5}$	PLJA counter	8_035	2/24/2006	9,8 - 20,9	292.531(11)	3.36(28)

Reproduced with permission of the copyright owner. Further reproduction prohibited without permission.

other two days represented by open squares and open triangles. These inconsistent measurements taken on Day 1 show a downward displacement indicating the presence of a larger electric field. Similar to the magnesium data, the measurements taken in this day can be brought into agreement, as shown by the solid circles, by applying a shift due to a field of 0.055 V/cm. This adjustment to Day 1 allows the data set to now be treated under the assumption of similar overall electric field. For the n=17 transitions, which are unaffected by the small possible daily fluctuations of stray field, it is reasonable to assume a constant field.

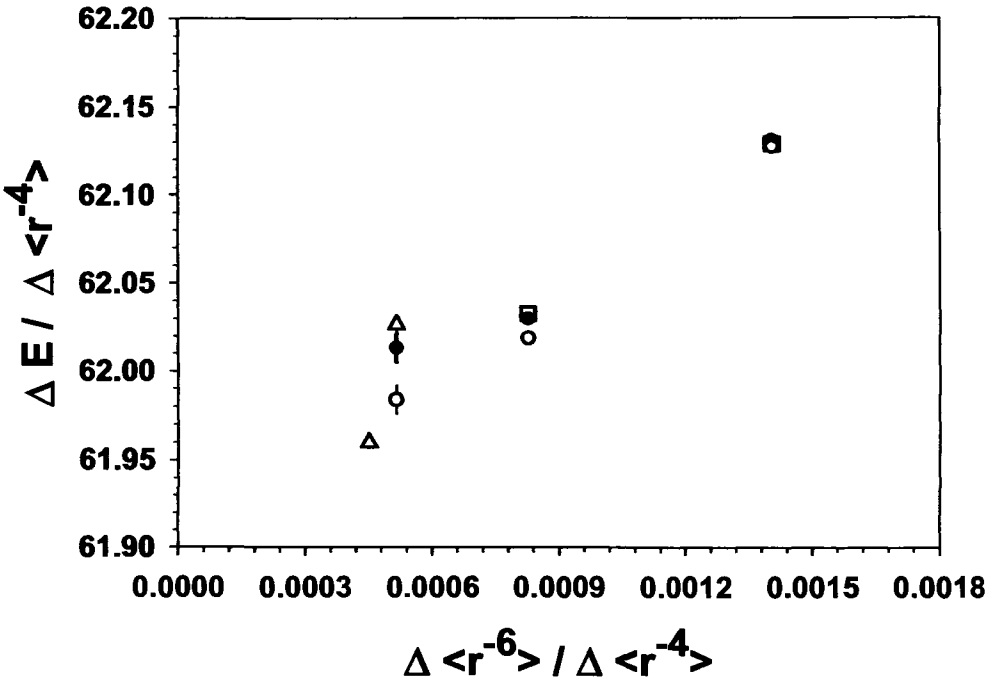

Figure 3.7: The n=20 barium fine structure intervals observed on three separate days are normalized to $\Delta < r^{-4} >$ and plotted versus $\Delta < r^{-6} > / \Delta < r^{-4} >$. The three types of points represent the three separate sets of data. The downward displacement for the day represented by circles is an indication of a larger stray electric field presence on that day.

The issue again arises of how to properly account for the overall stray DC electric

Reproduced with permission of the copyright owner. Further reproduction prohibited without permission.

fields that shift the measured intervals. For the case of barium, two different sets of data were obtained in different principle quantum states. The rate at which energy levels are shifted by electric fields depends not only on the angular momentum but also on the principle quantum state scaling with n^7. Fortunately, the n=17 states of barium are not significantly effected by stray fields. For the highest L state where there is n=17 and 20 data a field of 0.077(19) V/cm is determined to be present, which makes the measured intervals consistent. This amount of field is certainly plausible based on past experience and is consistent with the amount of field determined in the magnesium data that was obtained on the same apparatus [20].

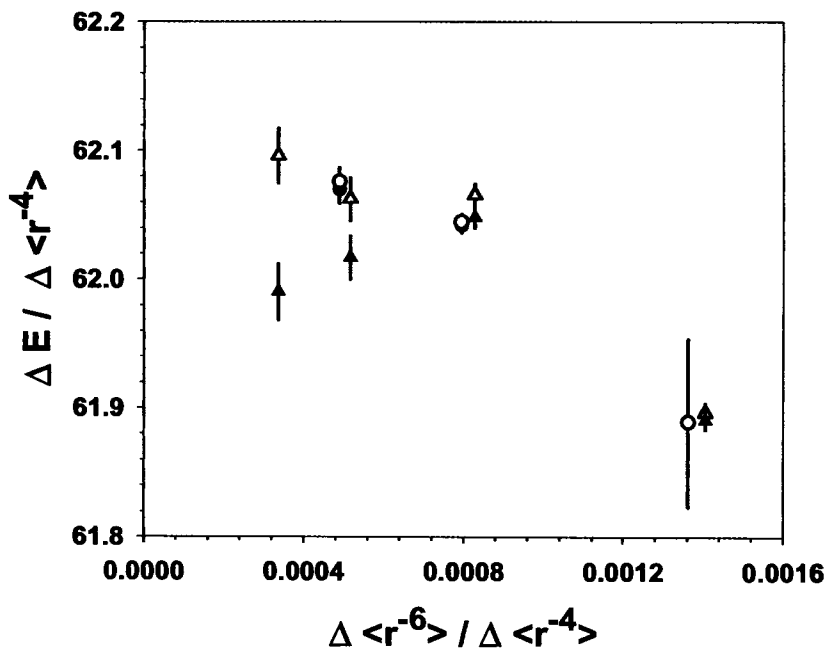

Figure 3.8: The measured n=17 and n=20 barium fine structure intervals corrected for relativistic and 2nd order energy effects and normalized to $\Delta < r^{-4} >$ are plotted versus $\Delta < r^{-6} > / \Delta < r^{-4} >$. The open points indicate the fine structure pattern corrected for a Stark field of 0.077(19) V/cm.

Reproduced with permission of the copyright owner. Further reproduction prohibited without permission.

The final line centers for barium are determined as follows. First the correction for the electric field on Day 1 is applied. Then the weighted average is taken of the resonances for all orientations of the rf region. The Doppler-free centers are calculated by averaging the co- and counter-propagating intervals. The overall Stark shift due to the presence of a 0.077(19) V/cm DC electric field is removed. Then the center of gravity is found for the two K states of each L level. The two observed transition energies are transitions between corresponding levels in the two states, either between K=L+1/2 states or between K=L-1/2 states, where K is the total angular momentum exclusive of Rydberg electron spin. According to the long-range polarization model that includes core spin, the state with higher K has the higher energy. Therefore the expression for the interval between the center of gravity of the two spin doublets is:

$$\Delta E_{C.G.} = \frac{L\Delta E_{K=L-1/2} + (L+1)\Delta E_{K=L+1/2}}{2L+1} + \frac{|\delta E_{L+1}|}{(2L+1)(2L+3)}, \tag{3.5}$$

where δE_{L+1} is the splitting in the upper level of the transition, and $\Delta E_{K=L-1/2}$ ($\Delta E_{K=L+1/2}$) is the transition energy between L, $K = L-1/2$ ($K = L+1/2$) and $L+1$, $K = L+1/2$ ($K = L+3/2$) states. The splittings are experimentally known, so the second term can be evaluated and the center of gravity of the transitions determined. The final intervals are presented in the following tables with their corresponding Stark shift rates.

The spin-orbit splittings can be determined with the observed interval measurements. The $\Delta K = 0$ transitions combined with the $\Delta K = 1$ transitions observed allow for the determination of the splitting within each L level. Simply taking the difference of the two transitions will give the splitting of one level and then this infor-

Reproduced with permission of the copyright owner. Further reproduction prohibited without permission.

Table 3.7: The final results of the fine structure measurements of barium n=17 are listed here with the Stark shift rates. The second error is due only to the uncertainty in the stray electric field.

n=17 L, K - L', K'	ΔE_{Obs} (MHz)	κ [MHz/(V/cm)^2]	$\Delta E_{E=0}$ (MHz)	$\Delta E_{C.G.}$ (MHz)
6, 11/2 - 7, 13/2	5854.401(40)	-5.6	5854.429(40)(17)	
6, 13/2 - 7, 15/2	5633.389(17)	-5.6	5633.417(17)(17)	5735.582(16)(17)
7, 13/2 - 8, 15/2	2439.890(26)	-7.5	2439.928(26)(23)	
7, 15/2 - 8, 17/2	2411.259(16)	-7.5	2411.297(16)(23)	2424.695(15)(23)
8, 15/2 - 9, 17/2	1165.877(20)	-10.3	1165.929(9)(31)	
8, 17/2 - 9, 19/2	1157.773(20)	-10.3	1157.825(20)(31)	1161.648(11)(31)
*9, 17/2 - 10, 19/2	604.289(28)	-12.7	604.353(28)(38)	
*9, 19/2 - 10, 21/2	601.535(28)	-12.7	601.599(28)(38)	602.906(19)(38)
6, 13/2 - 7, 13/2	5592.689(16)	-5.6	5592.717(16)(17)	

Table 3.8: The final results of the fine structure measurements of barium n=20 are listed here with the Stark shift rates. The second error is due only to the uncertainty in the stray electric field.

n=20 L, K - L', K'	ΔE_{Obs} (MHz)	κ [MHz/(V/cm)^2]	$\Delta E_{E=0}$ (MHz)	$\Delta E_{C.G.}$ (MHz)
7, 13/2 - 8, 15/2	1518.699(20)	-28.2	1518.840(20)(85)	
7, 15/2 - 8, 17/2	1499.999(23)	-28.2	1500.140(23)(85)	1508.971(15)(85)
8, 15/2 - 9, 17/2	727.860(24)	-40.2	728.061(24)(121)	
8, 17/2 - 9, 19/2	722.515(27)	-40.2	722.716(27)(121)	725.256(18)(121)
9, 17/2 - 10, 19/2	378.405(67)	-54.5	378.678(67)(164)	
9, 19/2 - 10, 21/2	376.638(67)	-54.5	376.911(67)(164)	377.754(47)(164)
*10, 19/2 - 11, 21/2	209.379(71)	-121.7	209.988(71)(365)	
*10, 21/2 - 11, 23/2	208.630(71)	-121.7	209.239(71)(365)	209.597(50)(365)
7, 15/2 - 8, 15/2	1492.136(35)	-28.2	1492.277(35)(85)	

mation is propagated in order to determine the remaining splittings. These spin-orbit splittings are listed in Table 3.9 and 3.10.

Reproduced with permission of the copyright owner. Further reproduction prohibited without permission.

Table 3.9: Barium n=17 Observed Fine Structure Level Splittings

n=17, L	δE_{Obs} (MHz)
6	261.712(43)
7	40.700(23)
8	12.069(38)
9	3.965(44)
10	1.213(59)

Table 3.10: Barium n=20 Observed Fine Structure Level Splittings

n=20, L	δE_{Obs} (MHz)
7	26.563(40)
8	7.863(42)
9	2.518(55)
10	0.751(110)
11	0.002(149)

Reproduced with permission of the copyright owner. Further reproduction prohibited without permission.

Chapter 4

Discussion of Results

As discussed in Chapter 1.3, the experimental fine structure data of $L \geq 7$ Rydberg states can be analyzed with the long-range model. Two refinements, the effective second order energies and relativistic effects, must be made to the observed intervals before the long-range model can be appropriately applied. The first of these is especially significant when the dipole polarizability is large, as in the case of Ba^+. The most significant portion of the fourth-order perturbation in V is found to be equivalent to the action of $V_{eff} = \frac{1}{2}\alpha_d r^{-4} + \cdots$, applied in second-order in the space of Rydberg levels. This "effective second-order polarization energy" is simply a function of α_d, n, and L in the case where the scale of the fine structure pattern is largely determined by α_d, and it has been explicitly calculated by Drake et al. in this case [49]. Given an approximate knowledge of α_d, the second-order polarization energy can be calculated for each state of interest and subtracted from the observed intervals. An error bar attached to the calculation of the effective second order energy accounts for the uncertainty in the dipole polarizability and the neglect of the next term in the

Reproduced with permission of the copyright owner. Further reproduction prohibited without permission.

effective potential. The second refinement removes the small relativistic contribution to the measured intervals, which come from the well known "p4" correction to the Rydberg electron's kinetic energy,

$$\left\langle -\frac{p^4}{8m^3c^2} \right\rangle = -\frac{Q^2\alpha^2}{2n^3}\left[-\frac{3}{4n} + \frac{1}{L+1/2}\right] a.u. \tag{4.1}$$

The contribution for the effective second order energy and the relativistic effects will be removed, so as to leave only the "corrected" interval, which should be well represented by the long-range model.

The accuracy of the long-range model with respect to the fine structure data pattern can be evaluated through the use of a polarization plot. The rough variation of the measured intervals can be removed by normalizing each measurement to the difference in the expectation value of r^{-4} in the two states, $\Delta\langle r^{-4}\rangle$. The difference of hydrogenic radial expectation values in each pair of states can be computed, using the analytic expressions for the radial expectation values, corrected for finite core ion mass (See Appendix D). The normalization of the corrected intervals produces values that are approximately constant, which would be expected to vary approximately linearly when displayed in a polarization plot versus $\Delta\langle r^{-6}\rangle / \Delta\langle r^{-4}\rangle$. A simple fit should model the data pattern, if the long-range model applies. The equation including the first few parameters corresponding to the first terms in the series is,

$$\frac{E}{\Delta\langle r^{-4}\rangle} = A_4 + A_6\frac{\Delta\langle r^{-6}\rangle}{\Delta\langle r^{-4}\rangle} + A_8\frac{\Delta\langle r^{-8}\rangle}{\Delta\langle r^{-4}\rangle}, \tag{4.2}$$

where A_4 is 1/2 the dipole polarizability, α_d. A_6 is 1/2 the quadrupole polarizability, α_Q, minus three times the first correction term to the dipole polarizability, β_d, and A_8 is a contribution from higher order terms.

Reproduced with permission of the copyright owner. Further reproduction prohibited without permission.

4.1 Polarization Analysis of Magnesium

Intervals of high-L states of Rydberg n=17 magnesium were experimentally determined and are listed in Table 4.1 with the corresponding effective second order energy and relativistic contributions. Recall, that the first error bar on the transition energy is due to the random error of the line center fit, and the second error bar represents the uncertainty in the Stark shift corrections. The error assigned to the effective second order energies, in column 4, is almost entirely due to the uncertainty from neglecting all but the first term in the effective potential. The "corrected" interval normalized by the difference in the expectation of the r^{-4} radial matrix element is given in column (7). According to the long-range polarization model these values are expected to vary approximately linearly when plotted versus $\Delta\langle r^{-6}\rangle / \Delta\langle r^{-4}\rangle$, which are listed in column (6). As seen from column (7), there is an increase in the normalized intervals as the progression to higher L states occurs.

Table 4.1: The relativistic (ΔE_{rel}) and second order (ΔE_{Sec}) contributions to each measured magnesium transition are shown in columns 3 and 4 respectively. ΔE_{Corr} is the measured interval, ΔE_{Obs}, corrected for the relativistic effects and second order energies. The first error bar is due to the random error of the fitted line center, while the second error bar represents the uncertainty in the electric field correction. The corrected interval is normalized to $\Delta < r^{-4} >$ in column 6 and the calculated ratio $\Delta < r^{-6} > / \Delta < r^{-4} >$ for each transition is also given. All energies are given in MHz.

nL - n'L'	ΔE_{Obs}	ΔE_{rel}	ΔE_{Sec}	$\Delta \langle r^{-4} \rangle$	$\Delta \langle r^{-6} \rangle / \Delta \langle r^{-4} \rangle$	$\Delta E_{Corr} / \Delta \langle r^{-4} \rangle$
17,6 - 17,7	1520.954(8)(32)	0.732	8.126(101)	88.7668	0.00252	17.0345(1)(12)
17,7 - 17,8	669.801(13)(49)	0.560	1.497(55)	38.7349	0.00136	17.2388(3)(19)
17,8 - 17,9	324.363(12)(66)	0.442	0.338(28)	18.6507	0.00079	17.3496(6)(38)
17,9 - 17,10	169.172(17)(78)	0.358	0.089(16)	9.6924	0.00049	17.4080(12)(82)
*17,10 - 17,11	93.869(62)(87)	0.296	0.027(10)	5.3526	0.00031	17.4767(116)(164)

Reproduced with permission of the copyright owner. Further reproduction prohibited without permission.

The fit to the data pattern of the normalized corrected intervals, plotted in Fig. 4.1, will lead to the experimentally extracted core properties. The dotted line represents a linear fit to the experimental data. The solid line indicates the prediction of the long-range model including terms up to $\langle r^{-6} \rangle$ by use of the calculated core properties α_d, α_Q, and β_d as given in Appendix D. These calculated core properties were determined by use of an all-order relativistic many-body perturbation theory [22]. Upon initial inspection, the agreement of the fitted data to the theory prediction only seems consistent with the intercept and not the slope.

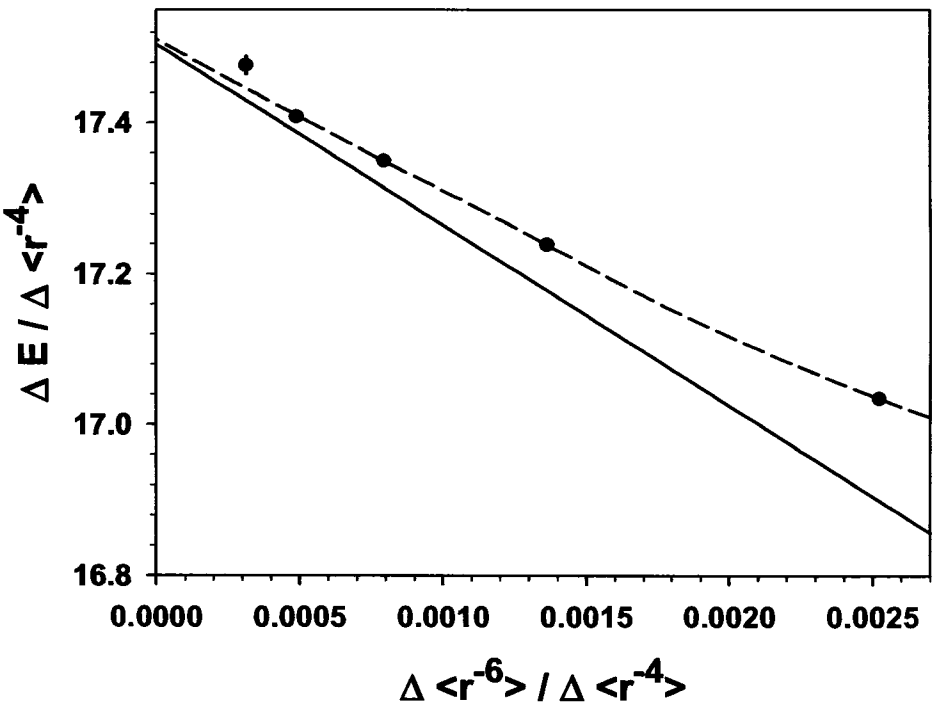

Figure 4.1: The measured magnesium fine structure intervals corrected for relativistic and 2nd order energy effects as described in the text and normalized to $\Delta < r^{-4} >$ are plotted versus $\Delta < r^{-6} > / \Delta < r^{-4} >$. The solid line represents the theory prediction based on terms up to and including $\Delta < r^{-6} >$.

A series of three fits are done for the uncertainty in the stray electric field and

Reproduced with permission of the copyright owner. Further reproduction prohibited without permission.

effective second order energy correction in order to evaluate the appropriate size of the error bars on the fitted parameters, since these errors are correlated. Recall that in Chapter 3, the electric field was determined to be 0.089(11) V/cm, and the calculated Stark shift was applied to the measured intervals. The data pattern is fit to Eq.(4.2) for the assumed electric field and also for cases of plus and minus one standard deviation of the correlated errors. The fit to the first few terms in the polarization model results in fitted parameters of

$$A_4 = 17.512(4)(14)$$

$$A_6 = \text{-}211(5)(14)$$

$$A_8 = 7320(1058)(3654).$$

This leads to the following ion core properties for Mg^+,

$$\alpha_d = 2A_4 = 35.02(3)$$

$$\alpha_Q = 2A_6 + 6\beta_d = 214(36),$$

where $\beta_d = 106(1)$ as determined with the calculated matrix elements. The dipole polarizability is in perfect agreement with the theoretical calculations, $\alpha_d = 35.01$, but the quadrupole polarizability is inconsistent with theory [22]. The relativistic many-body theory gives a value of 156 for α_Q, which is approximately two standard deviations from the experimentally extracted value given above.

Higher order terms of r^{-7} and $L(L+1)r^{-8}$ can be included in the long-range polarization model. These terms due to the third order and second non-adiabatic dipole energies can be calculated, as discussed in Chapter 1, using theoretical matrix elements and experimental core energies. The matrix elements are listed in Appendix

Reproduced with permission of the copyright owner. Further reproduction prohibited without permission.

C for all states of interest and are considered to be uncertain by 0.5%. Although the quoted uncertainty is small, the fact that only the lowest excited core state is included causes an uncertainty in the calculation. A very crude estimate of the next term in the summation indicates a contribution of 0.05% of the first term. The total uncertainty, therefore, will include an additional error of 0.1% for the truncation after the first term. The calculation of these higher order terms was performed for the spinless case and the case where the core fine structure is included as done in section 1.2. Both calculations give the same results for the contribution of the higher order terms to the energy of state nL

$$E_{H.O.T.} = 1684(19) < r^{-7} >_{nL} -1170(12)L(L+1) < r^{-8} >_{nL}, \qquad (4.3)$$

where $E_{H.O.T}$ is the contribution of the second non-adiabatic dipole and third order dipole energy contribution from only the lowest core excited states. The error bars reflect the uncertainty in both the calculation of the matrix elements and the neglect of the remaining excited core states. These values are subtracted from the measured intervals and shown in the polarization plot as open circles in Fig. 4.2, where the previous data points are shown as solid circles.

Correction of the data to remove contributions of the higher order terms in the long-range model results in excellent agreement between the experiment and theory for both the intercept and slope of the polarization plot. Fits to this data pattern, which have the higher order terms removed, are repeated again for three values of stray electric field to evaluate the appropriate uncertainty due to electric field corrections. The fitted parameters and subsequent core properties are given in Table 4.2 with

Reproduced with permission of the copyright owner. Further reproduction prohibited without permission.

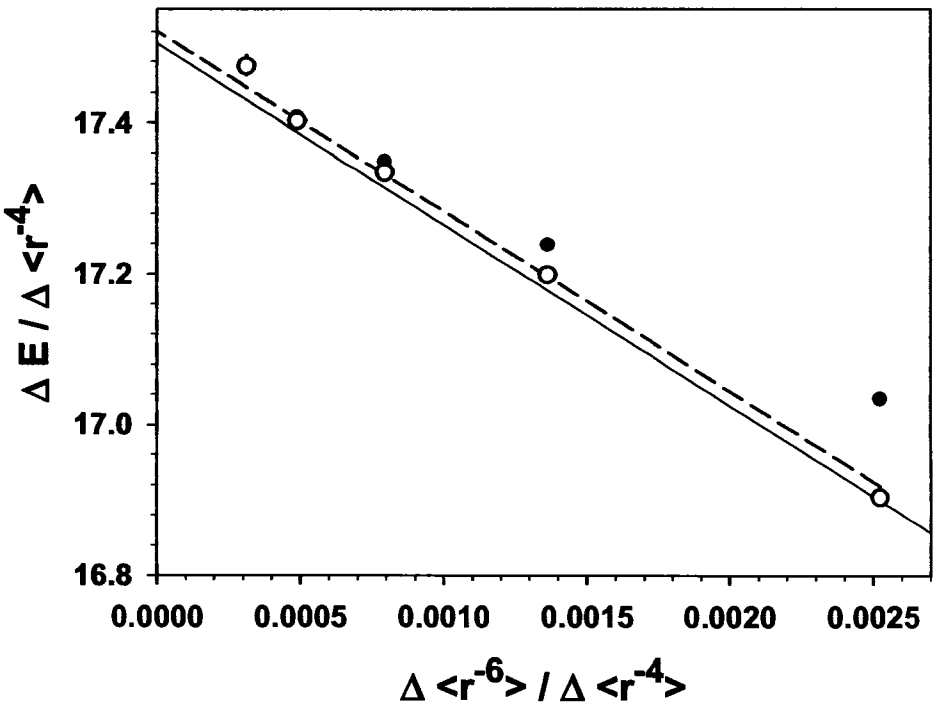

Figure 4.2: The Stark corrected magnesium fine structure intervals corrected for relativistic and 2nd order energy effects as described in the text and normalized to $\Delta < r^{-4} >$ are plotted versus $\Delta < r^{-6} > / \Delta < r^{-4} >$ (solid circles). The open circles represent the data with the higher order contributions removed. The solid line indicates the theory prediction based on terms up to and including $\Delta < r^{-6} >$. The dotted line represents the fit to the open circle points.

Reproduced with permission of the copyright owner. Further reproduction prohibited without permission.

a previous work [15], and the separate theoretical calculations given in column (4). The rough estimate of how the slope will change by including terms of $\langle r^{-7} \rangle$ and $L(L+1)\langle r^{-8} \rangle$ from Chapter 1.1 predicted a change in slope of -33, and the experiment finds a change in slope of only -7(25), which is consistent with the prediction. The fitted A8 parameter changed dramatically, however, even changing sign.

Table 4.2: The fitted parameters and subsequent core parameters are given along with a previous study [15] and the theoretical values [22]. The two error bars on the parameters correspond to the random error of the fit and the correlated error, due to the electric field corrections and effective second order energy corrections.

	This work	Lyons et al. [15]	Theory
A4	17.5117(88)(163)	16.9(3)	17.505
A6	-217(16)(18)	-31(1)	-240
A8	-8000(5200)(4000)		
α_d	35.02(4)	33.8(5)	35.01
α_Q	202(54)		156

The final results from the magnesium experiment are a dipole polarizability of $35.02(4)a_0$ and a quadrupole polarizability of $202(54)a_0$. The dipole polarizability is not altered by the inclusion of higher order terms, but the slope, which is directly related to the quadrupole polarizability, is slightly affected. As discussed in the introduction the main motivation of this thesis was to investigate the discrepancies between experiment and theory with respect to the slope. The case of magnesium was one of these systems in which a discrepancy was long standing. For the first time, the use of high-L Rydberg fine structure reveals a measurement of the quadrupole polarizability that is consistent with calculations.

Reproduced with permission of the copyright owner. Further reproduction prohibited without permission.

4.2 Polarization Analysis of Silicon III

Experimental work previously performed in $^2S_{1/2}$ silicon III by Komara, et al. [20] found a large discrepancy between the fitted A_6 and independent theoretical calculations. Perhaps this discrepancy can also be resolved by the inclusion of higher order terms as found above for neutral magnesium. The same theory applies, but care must be taken in order to appropriately account for the Q=3 ion core charge.

Stray electric fields were included in the previous analysis by allowing for an extra parameter that scaled with the Stark shift rates. As discussed by Komara, the stray DC electric fields could range from 0.1 to 0.2 V/cm on any given day. A field of 0.110(10) V/cm was determined to best explain the measured data pattern. This value is adopted here, with an additional two fits at the extreme limits in order to assign a suitable error bar that accounts for the uncertainty in the stray field.

The higher order contribution to the state energies from the first excited ion core state of the second non-adiabatic and third order energies, $E_{H.O.T}$, are given here,

$$E_{H.O.T.} = 122.3(2) < r^{-7} >_{nL} -60.6(2)L(L+1) < r^{-8} >_{nL} . \qquad (4.4)$$

The calculation attributes the 0.04% uncertainty the theoreticians assigned to the matrix elements and 0.1% to the uncertainty from only including the lowest excited core state contribution. These contributions are subtracted from the corrected intervals.

Now that the contribution to the higher order terms has been removed the simple polarization analysis can be performed. The open circles in figure 4.3 represent the corrected normalized intervals reported by Komara et al. The open squares in the silicon III polarization plot indicate the corrected intervals with the higher order

Reproduced with permission of the copyright owner. Further reproduction prohibited without permission.

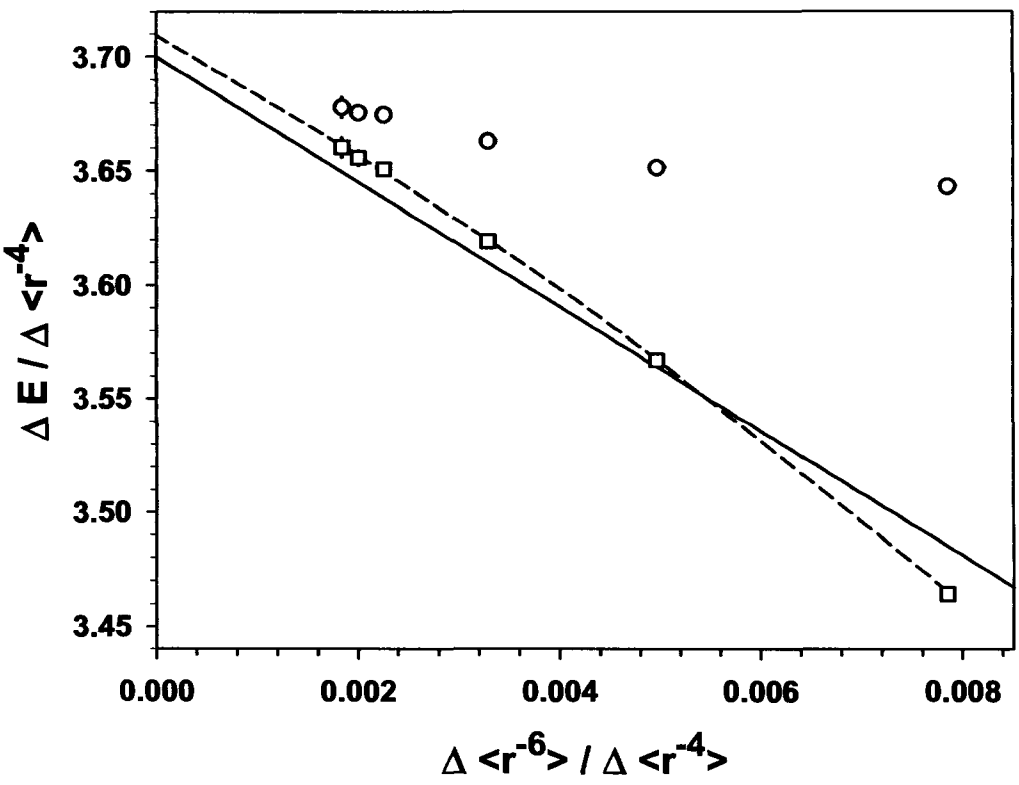

Figure 4.3: The measured Si^{2+} fine structure intervals corrected for relativistic and 2nd order energy effects and normalized to $\Delta < r^{-4} >$ are plotted versus $\Delta < r^{-6} > / \Delta < r^{-4} >$. The open circles indicate the fine structure pattern corrected for a Stark field of 0.110 V/cm. The open squares represent the previous data with the higher order contributions removed. The dotted line represents the fit to the open square points. The solid line indicates the theory prediction based on terms up to and including $\Delta < r^{-6} >$.

Reproduced with permission of the copyright owner. Further reproduction prohibited without permission.

term contributions removed. The results from the fits to the first three terms in the polarization model and subsequent core properties are given, along with the previous studies results and the theoretical predictions, in Table 4.3. A calculated β_d, 11.0(1), is used in order to convert the slope of the polarization plot into a value for the quadrupole polarizability.

Table 4.3: The fitted parameters and subsequent core properties for Si^{3+} are given along with the results from the previous study [20] and theoretical values [22]. The two error bars on the parameters correspond to the random error of the fit and the uncertainty due to the electric field corrections respectively.

	This work	Komara et al. [19]	Theory
A4	3.709(2)(5)	3.702(5)	3.7
A6	-24.7(1.1)(1.7)	-14.5(1.6)	-27.4
A8	-776(105)(119)	$-2.5(1.1)\times10^3$	
α_d	7.419(11)	7.404(11)	7.4
α_Q	17(4)	37(3)	11.2

It can be seen that just as in the case presented in the last section for magnesium, the disagreement of the quadrupole polarizability with theoretical calculations has been resolved. For the case of Si^{2+}, the effect of the higher order terms is very dramatic, altering the slope by nearly a factor of two.

4.3 Polarization Analysis of Barium

Table 4.4 lists the observed intervals with the corresponding contributions for relativistic effects and effective second order energies. Unlike the cases of magnesium and Si^{2+}, barium is not expected to have a convergent quadrupole series as discussed in Chapter 1.1. In order to account for significant non-adiabatic quadrupole energies,

Reproduced with permission of the copyright owner. Further reproduction prohibited without permission.

the multiplicative factor, k_Q, is used to estimate the contributions for each transition. This quadrupole non-adiabatic correction, ΔE_{NA}, is listed in column 5 of Table 4.4. The error bar assigned to this correction is determined by assuming 30% uncertainty in the lowest ion core state quadrupole polarizability. Then column 8 lists the corrected interval normalized to $\Delta \langle r^{-4} \rangle_{nl}$. Table 4.5 gives the values used in this work for the correction factors, k_Q, determined by use of Method 2 involving the Dalgarno-Lewis technique.

Table 4.4: The relativistic (ΔE_{rel}) and second order (ΔE_{Sec}) contributions to each measured barium transition are shown in columns 3 and 4 respectively. The quadrupole non-adiabatic energy correction, ΔE_{NA}, estimated by use of the Dalgarno-Lewis method is given in column 5. The ΔE_{Corr} value is the measured center of gravity interval, $\Delta E_{C.G.}$, corrected for the relativistic effects, second order energies, and first excited core state quadrupole non-adiabatic effects. The corrected interval is normalized to $\Delta \langle r^{-4} \rangle$ and is given in column 8. The calculated $\Delta \langle r^{-4} \rangle$ and ratio $\Delta \langle r^{-6} \rangle / \Delta \langle r^{-4} \rangle$ for each transition is also given.

nL - n'L'	$\Delta E_{C.G.}$	ΔE_{rel}	ΔE_{Sec}	ΔE_{NA}	$\Delta \langle r^{-4} \rangle$	$\Delta \langle r^{-6} \rangle / \Delta \langle r^{-4} \rangle$	$\Delta E_{Corr} / \Delta \langle r^{-4} \rangle$
17,7 - 17,8	2424.695(15)(23)	0.560	18.815(76)	8.061(2.417)	38.7347	0.00136	61.8892(4)(624)
17,8 - 17,9	1161.648(11)(31)	0.442	4.252(29)	-0.235(71)	18.6509	0.00079	62.0447(6)(44)
*17,9 - 17,10	602.906(19)(38)	0.358	1.123(14)	-0.240(72)	9.6924	0.00049	62.0760(20)(85)
20,7 - 20,8	1508.971(15)(85)	0.344	11.879(58)	5.731(1.720)	24.0889	0.00141	61.8964(6)(715)
20,8 - 20,9	725.256(18)(121)	0.271	2.713(24)	-0.191(57)	11.6403	0.00083	62.0656(15)(117)
20,9 - 20,10	377.754(47)(164)	0.220	0.726(13)	-0.146(44)	6.0738	0.00052	62.0622(77)(280)
*20,10 - 20,11	209.597(50)(365)	0.181	0.220(6)	-0.055(17)	3.3698	0.00034	62.0960(148)(1084)

Table 4.5: The correction factors, k_Q, calculated by use of Method 2, involving the Dalgarno-Lewis technique, are listed for the states of barium observed in this work.

(n,L)	k_Q Method 2	(n,L)	k_Q Method 2
(17,6)	1.614	(20,7)	1.073
(17,7)	1.059	(20,8)	0.989
(17,8)	0.984	(20,9)	0.973
(17,9)	0.971	(20,10)	0.974
(17,10)	0.973	(20,11)	0.978

Reproduced with permission of the copyright owner. Further reproduction prohibited without permission.

These are the values plotted in Fig. 4.4 versus $\Delta\langle r^{-6}\rangle_{nL}/\Delta\langle r^{-4}\rangle_{nL}$. It can be easily seen that the data is lacking in agreement with theoretical calculations including up to $\langle r^{-6}\rangle$, as shown by the solid line.

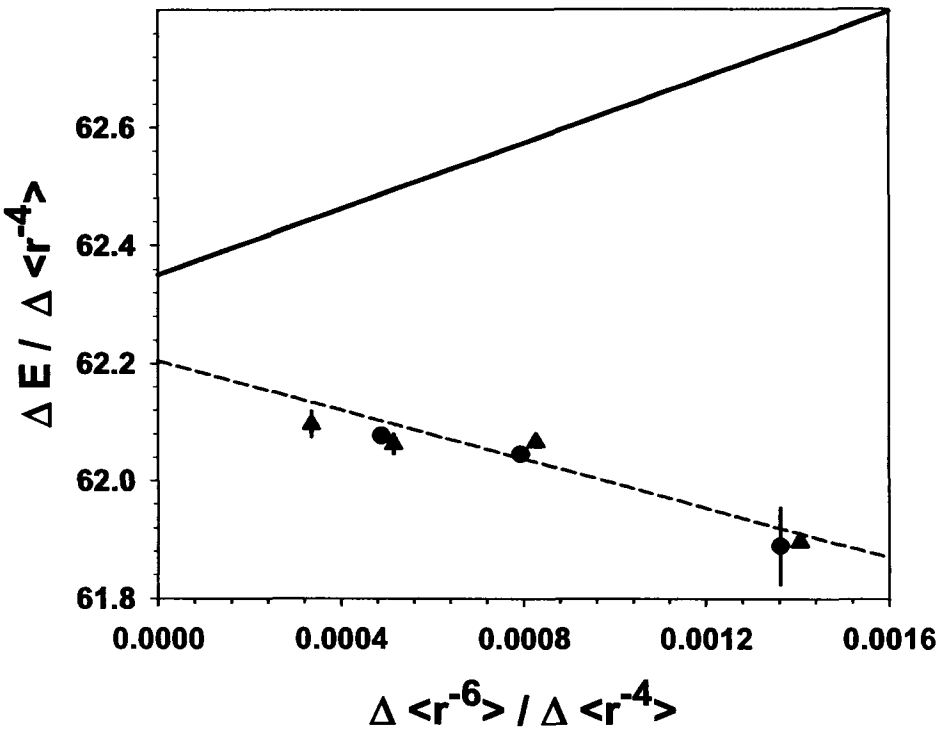

Figure 4.4: The measured n=17 (circles) and n=20 (triangles) barium fine structure intervals corrected for relativistic and 2nd order energy effects and normalized to $\Delta < r^{-4} >$ are plotted versus $\Delta < r^{-6} > /\Delta < r^{-4} >$. The solid line indicates the theory prediction based on terms up to and including $\Delta < r^{-6} >$.

Again the higher order terms, $\left(\frac{1}{2}\delta + \frac{8}{5}\gamma\right)\langle r^{-7}\rangle$ and $\frac{18}{5}\gamma L(L+1)\langle r^{-8}\rangle$, can be included in this analysis. The matrix elements listed in Appendix C for barium are determined to an uncertainty of one percent. Of all the systems studied in this work, barium has the largest core fine structure. Thus the higher order terms were evaluated both by the spinless theory and the theory presented in the second section

Reproduced with permission of the copyright owner. Further reproduction prohibited without permission.

of Chapter 1, where the core spin was included, for comparison. A difference of only 0.1 % is found for the calculated δ and 3% for γ both of which are within the calculated uncertainty. The calculations including the spin of the core electron give contributions to the state energies as follows,

$$E_{H.O.T.} = 2.99(6) \times 10^4 < r^{-7} >_{nL} -1.11(2) \times 10^4 L(L+1) < r^{-8} >_{nL}, \qquad (4.5)$$

where $E_{H.O.T}$ is the second non-adiabatic dipole and third order dipole energy contribution from only the lowest core excited states. Note that based on the rough analysis in Chapter 1.1, the expected change in the fitted slope is -1389 from the higher order terms.

Figure 4.5 shows, in addition to the theory, the intervals where the contribution of the second non-adiabatic and third order energies have been removed, which are displayed as open circles (n=17) and open triangles (n=20). The corresponding error bars are expanded to include the 1% uncertainty in the calculated Ba^+ matrix elements used to determine the higher order contributions.

Fitted parameters are found for three different values of the stray electric field of 0.054V/cm, 0.071V/cm, and 0.088V/cm. The fit with a field equal to 0.071 V/cm is taken to be the final value. The error bars are expanded, as determined by the other two fits, to allow for the correlated uncertainty in the electric field estimate, the quadrupole non-adiabatic correction and the effective second order energy correction. The value for β_d, the first non-adiabatic dipole correction, was obtained by use of the theoretical matrix elements to be 598(10). Table 4.6 lists the fitted parameters and corresponding ion core properties for the fit function in Eq.(4.2). Column 3 gives the

Reproduced with permission of the copyright owner. Further reproduction prohibited without permission.

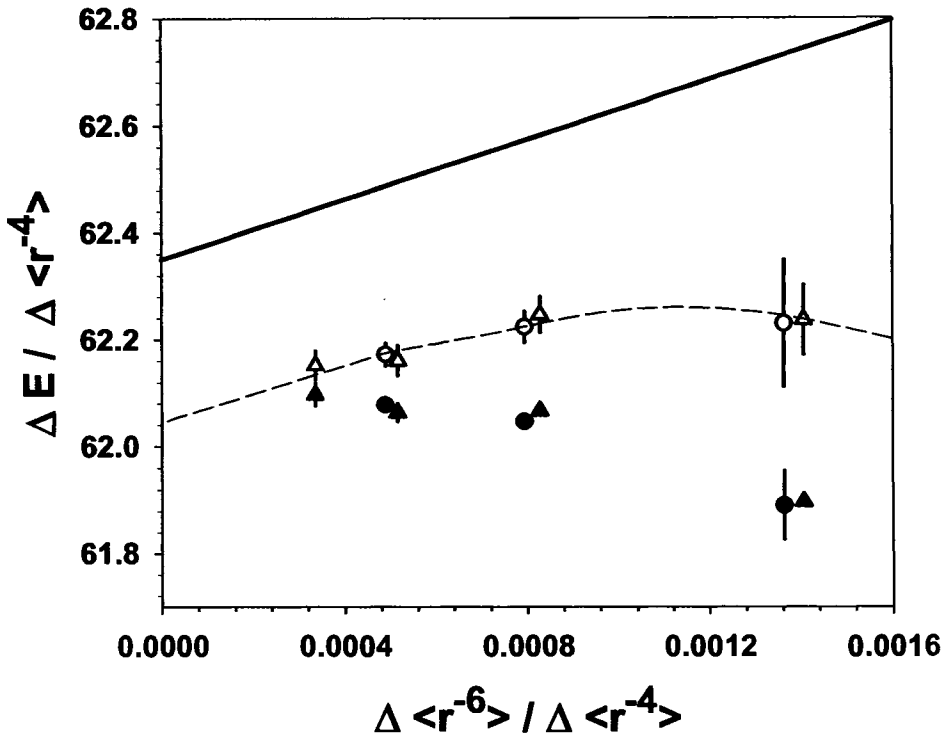

Figure 4.5: The measured barium fine structure intervals corrected for relativistic and 2nd order energy effects and normalized to $\Delta \langle r^{-4} \rangle$ are plotted versus $\Delta \langle r^{-6} \rangle / \Delta \langle r^{-4} \rangle$ as solid circles (n=17) and solid triangles (n=20). The open circles (n=17) and open triangles (n=20) represent the data with the higher order contributions removed. The dotted line represents the linear fit to the intervals which have the higher order contributions removed. The solid line indicates the theory prediction based on terms up to and including $\Delta \langle r^{-6} \rangle$.

Reproduced with permission of the copyright owner. Further reproduction prohibited without permission.

results from a previous study by Snow et al. and column 4 lists the theoretical values [23, 22].

Table 4.6: The fitted parameters and subsequent core parameters are given along with the theoretical values. The two error bars on the parameters correspond to the random error of the fit and the uncertainty due to the correlated errors respectively.

	This work	Snow et al. [22]	Theory
A4	62.044(72)(112)	62.152(74)	62.4(13)
A6	325(196)(229)	-518(170)	279(70)
A8	-1.2(11)(10) x 10^5		
α_d	124.09(27)	124.30(16)	124.7(2.5)
α_Q	4238(643)	2462(361)	4145(83)

The polarizabilities of Ba^+ are found to be consistent with the theoretical calculations. The dipole polarizability is found to be 124.09(27). The quadrupole polarizability determined to be 4238(643) is different from theory by only 2%, which is consistent unlike the previous study. This value of the quadrupole polarizability is also consistent with lifetime measurements of the 5D states in Ba^+, which correspond to the inverse of the square matrix element [29, 31].

The value extracted here for the quadrupole polarizability is larger than determined in previous studies by Gallagher et al. [13] and Snow et al. [23]. Neither of these two works included the contribution from the third order adiabatic energy and the second non-adiabatic dipole energy. Using the crude argument from Chapter 1, it is predicted that the slope would be altered by 29916*0.041-11088*0.087=262. This contribution to the slope from the higher order energy could explain the disagreement in the values found by both Gallagher et al. and Snow et al.

Reproduced with permission of the copyright owner. Further reproduction prohibited without permission.

4.4 Spin Splitting Analysis of Barium

Observations in barium provided precise measurements of the spin-orbit splittings in the fine structure. The large core fine structure and non-adiabatic characteristics in barium result in very large spin-orbit splittings. Analysis of these splittings offer an independent check of the calculated dipole and quadrupole matrix elements of the lowest excited core states, which are directly related to the induced dipole and quadrupole polarizabilities. The spin-orbit splittings are also sensitive to the deviation from LS coupling as demonstrated in Chapter 1.3.

Measurements of the fine structure intervals from each of the K states combined with a $\Delta K = 0$ measurement allows for precise determination of the splittings within each L state. Tables 4.7 and 4.8 list all the measured spin splittings. Fortunately these measurements are not susceptible to stray electric fields, due to the fact that the Stark shift rate is very similar for states of same L. Since the splittings are the difference between states of the same L, the relativistic and second order energies also do not contribute. The analysis of the spin splittings, therefore, gives a simpler test of the theoretical calculations because there are fewer systematic corrections.

As mentioned above, the observed splittings can also be used to evaluate the accuracy of the calculated ion core matrix elements. The observed splittings consist of both the K splitting and the "normal" spin-orbit splittings described by the approximate spin Hamiltonian (See Eq.(1.28)). The "normal" spin orbit splittings can be calculated,

$$\Delta E_{Normal} = \frac{\alpha^2 Q^4}{n^3 L(L+1)}, \tag{4.6}$$

Reproduced with permission of the copyright owner. Further reproduction prohibited without permission.

Table 4.7: The energy splitting observed for each fine structure level of n=17 and the "normal" spin-orbit splittings are listed in column 2 and 3 respectively. The difference of these two, column 3, is the K splitting.

n=17, L	δE_{Obs} (MHz)	δE_{Norm} (MHz)	$\delta E_{Obs} - \delta E_{normal}$ (MHz)
6	261.712(43)	-1.7	263.412(43)
7	40.700(23)	-1.27	41.970(23)
8	12.069(38)	-0.988	13.057(38)
9	3.965(44)	-0.79	4.755(44)
10	1.213(59)	-0.65	1.863(59)

Table 4.8: The energy splitting observed for each fine structure level of n=20 and the "normal" spin-orbit splittings are listed in column 2 and 3 respectively. The difference of these two, column 3, is the K splitting.

n=20, L	δE_{Obs} (MHz)	δE_{Norm} (MHz)	$\delta E_{Obs} - \delta E_{normal}$ (MHz)
7	26.563(40)	-0.780	27.343(40)
8	7.863(42)	-0.608	8.471(42)
9	2.518(55)	-0.485	3.003(55)
10	0.751(110)	-0.399	1.150(110)
11	0.002(149)	-0.330	0.332(149

Reproduced with permission of the copyright owner. Further reproduction prohibited without permission.

and subtracted from the observed splittings. Then the remaining portion, the K splitting, is normalized to $(2L+1)\langle r^{-6}\rangle$ and plotted versus $\langle r^{-8}\rangle / \langle r^{-6}\rangle$. Just as in the polarization analysis, the data can be simply fit to

$$\frac{\delta E - \Delta E_{Normal}}{(2L+1) < r^{-6} >} = B_0 + B_1 \frac{< r^{-8} >}{< r^{-6} >}, \tag{4.7}$$

where

$$\begin{aligned} B_0 &= \frac{1}{12}\left(\frac{2 < g\|\vec{D}\|6P_{1/2} >^2}{E(6P_{1/2})^2} - \frac{< g\|\vec{D}\|6P_{3/2} >^2}{E(6P_{3/2})^2}\right) \\ B_1 &= \frac{1}{20}\left(\frac{3 < g\|\vec{Q}\|5D_{3/2} >^2}{E(5D_{3/2})^2} - \frac{2 < g\|\vec{Q}\|5D_{5/2} >^2}{E(5D_{5/2})^2}\right) \\ &\quad -\frac{3}{4}\left(\frac{2\left\langle g\|\vec{D}\|6P_{1/2}\right\rangle^2}{E(6P_{1/2})^3} - \frac{\left\langle g\|\vec{D}\|6P_{3/2}\right\rangle^2}{E(6P_{3/2})^3}\right), \end{aligned} \tag{4.8}$$

A simple fit to a straight line leads to a precision in the parameters related to the dipole and quadrupole matrix elements of 1% and 5% respectively. The results of the linear fit are summarized here,

$$\mathrm{B_0} = 30.6(4)$$

$$\mathrm{B_1} = 5280(274)$$

The parameters can be reduced to the radial matrix elements and a value for the deviation from pure LS coupling. The deviation from pure LS coupling for each level, $\epsilon = \bar{\epsilon} \pm \Delta\epsilon/2$, is included as was done in Chapter 1.3. However, the energies will not be approximated, because the experimental values of the ion core states are extremely well determined and therefore will be assumed to be exact. Rewriting the parameters in terms of the radial matrix elements keeping only terms of first order in

Reproduced with permission of the copyright owner. Further reproduction prohibited without permission.

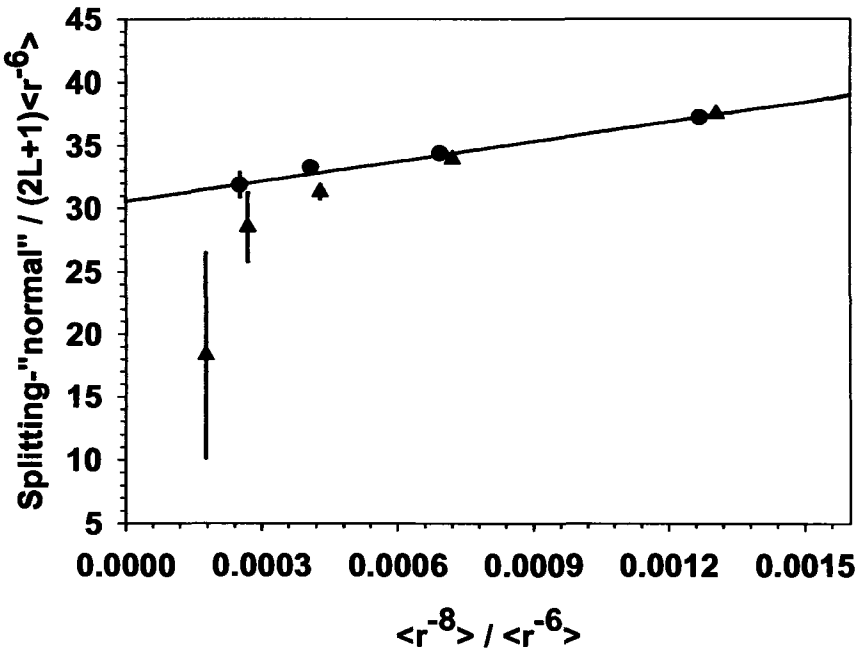

Figure 4.6: The splitting of each fine structure level minus the "normal" spin-orbit splitting is normalized to $\Delta < r^{-4} >$ and plotted versus $\Delta < r^{-6} > / < r^{-4} >$. The triangles represent the n=20 splittings while the circles represent the n=17. The solid line is the linear fit to this data pattern.

Reproduced with permission of the copyright owner. Further reproduction prohibited without permission.

$\Delta\epsilon$ gives,

$$\begin{aligned} B_0 &\approx \frac{1}{9}\left[< g\|\vec{D}\|P > (1+\bar{\epsilon}_p)\right]^2 \left[\frac{1+\frac{\Delta\epsilon_p}{1+\bar{\epsilon}_p}}{E(6P_{1/2})^2} - \frac{1-\frac{\Delta\epsilon_p}{1+\bar{\epsilon}_p}}{E(6P_{3/2})^2}\right] \\ B_1 &\approx \frac{3}{25}\left[< g\|\vec{Q}\|D > (1+\bar{\epsilon}_d)\right]^2 \left[\frac{1+\frac{\Delta\epsilon_d}{1+\bar{\epsilon}_d}}{E(5D_{3/2})^2} - \frac{1-\frac{\Delta\epsilon_d}{1+\bar{\epsilon}_d}}{E(5D_{5/2})^2}\right] \\ &\quad - \left[\left\langle g\|\vec{D}\|P\right\rangle (1+\bar{\epsilon}_p)\right]^2 \left[\frac{1+\frac{\Delta\epsilon_p}{1+\bar{\epsilon}_p}}{E(6P_{1/2})^3} - \frac{1-\frac{\Delta\epsilon_p}{1+\bar{\epsilon}_p}}{E(6P_{3/2})^3}\right]. \end{aligned} \tag{4.9}$$

This expression can be written as shown below in order to emphasize the strong dependence on the difference from pure LS coupling for the two states.

$$\begin{aligned} B_0 &\approx \frac{1}{9}\left[< g\|\vec{D}\|P > (1+\bar{\epsilon}_p)\right]^2 \left[\left(\frac{1}{E(6P_{1/2})^2} - \frac{1}{E(6P_{3/2})^2}\right)\right. \\ &\quad \left. + \left(\frac{\Delta\epsilon_p}{1+\bar{\epsilon}_p}\right)\left(\frac{1}{E(6P_{1/2})^2} + \frac{1}{E(6P_{3/2})^2}\right)\right] \\ B_1 &\approx \frac{3}{25}\left[< g\|\vec{Q}\|D > (1+\bar{\epsilon}_d)\right]^2 \left[\left(\frac{1}{E(5D_{3/2})^2} - \frac{1}{E(5D_{5/2})^2}\right)\right. \\ &\quad \left. + \left(\frac{\Delta\epsilon_d}{1+\bar{\epsilon}_d}\right)\left(\frac{1}{E(5D_{3/2})^2} + \frac{1}{E(5D_{5/2})^2}\right)\right] \\ &\quad - \left[\left\langle g\|\vec{D}\|P\right\rangle (1+\bar{\epsilon}_p)\right]^2 \left[\left(\frac{1}{E(6P_{1/2})^3} - \frac{1}{E(6P_{3/2})^3}\right)\right. \\ &\quad \left. + \left(\frac{\Delta\epsilon_p}{1+\bar{\epsilon}_p}\right)\left(\frac{1}{E(6P_{1/2})^3} + \frac{1}{E(6P_{3/2})^3}\right)\right]. \end{aligned} \tag{4.10}$$

Inserting the experimental values for these lowest core state energies of Ba^+ [41] gives,

$$\begin{aligned} B_0 &= 1.9310\left[< g\|\vec{D}\|P > (1+\bar{\epsilon}_p)\right]^2 \left[1 + 12.50\left(\frac{\Delta\epsilon_p}{1+\bar{\epsilon}_p}\right)\right] \\ B_1 &= 63.842\left[< g\|\vec{Q}\|D > (1+\bar{\epsilon}_d)\right]^2 \left[1 + 6.62\left(\frac{\Delta\epsilon_d}{1+\bar{\epsilon}_d}\right)\right] \\ &\quad -271.642\left[< g\|\vec{D}\|P > (1+\bar{\epsilon}_p)\right]^2 \left[1 + 8.36\left(\frac{\Delta\epsilon_p}{1+\bar{\epsilon}_p}\right)\right] \end{aligned} \tag{4.11}$$

Reproduced with permission of the copyright owner. Further reproduction prohibited without permission.

where,

$$E(P_{1/2}) = 0.09231847 a.u.$$

$$E(P_{3/2}) = 0.10002251 a.u.$$

$$E(D_{3/2}) = 0.02220690 a.u.$$

$$E(D_{5/2}) = 0.02585632 a.u. \tag{4.12}$$

The dipole results in terms of the radial matrix element and the average deviation from pure LS coupling are shown in figure 4.7. The value of $\left\langle g\|\vec{D}\|P\right\rangle(1+\epsilon_p)$ as determined from the B_0 parameter is plotted as a function of the assumed value $\Delta\epsilon_P/(1+\bar{\epsilon}_P)$, the LS coupling difference between the two ion core excited states The two solid lines indicate one standard deviation limits. The dashed lines show one standard deviation of the radial matrix element determined from the experimental lifetime measurements [28]. The lifetime is calculated as: $\tau_a = (\sum_{b\leq a} A_{ab})^{-1}$, which necessitates calculating the transition amplitudes for the $6p_j$ to $5d_j$ states in order to extract the matrix element. The transition amplitude for electric dipole transitions is

$$A_{ab} = \frac{2.02613 \times 10^{18} \left|\langle a\|r\|b\rangle\right|^2}{\lambda^3(2j_a+1)}, \tag{4.13}$$

where λ is the wavelength of the transition in angstroms. The theoretical calculations for these transition amplitudes were in perfect agreement with experiment [22, 50] and an error of 1% from the matrix element is propagated through this calculation. The geometric mean of the experimental values for the $6p_{1/2}$ and the $6p_{3/2}$ matrix

Reproduced with permission of the copyright owner. Further reproduction prohibited without permission.

elements from the lifetime measurements give

$$\left\langle g\|\vec{D}\|6P_{1/2}\right\rangle \left\langle g\|\vec{D}\|6P_{1/2}\right\rangle \approx \frac{2\sqrt{2}}{3}\left\langle g\|\vec{D}\|6P\right\rangle^2 (1+\epsilon_p)^2, \tag{4.14}$$

which results in the value plotted in figure 4.7. The intersection area of the lifetime measurements and the splitting measurements of this work put limits on both the radial matrix element and the deviation from pure LS coupling. A determination of both of these values is only possible with both the splitting data and the lifetime measurements. The theoretical value, based on the calculated values of both $\langle g|r|p_{1/2}\rangle$ and $\langle g|r|p_{3/2}\rangle$ matrix elements, is represented by a point at the value for $\Delta\epsilon/(1+\bar{\epsilon})$ with which the matrix elements correspond. The results of the polarization analysis is also shown on this plot as the dotted line. In order to calculate this value it is assumed that the fractional contribution to the dipole polarizability from the 6P states is 0.93 based on theoretical calculations. Not shown on the graph but noteworthy, is the measurement of Shuman et al., which gives a value of the radial matrix element of 4.03(26) regardless of the deviation from LS coupling because any deviation from pure LS coupling was neglected. Due to the large uncertainty in Shuman's measurement it is consistent with the theory and both the lifetime and splitting experiments.

The information displayed in Fig. 4.7 offers two different scenarios. If the theoretical value for the deviation from pure LS coupling is assumed to be true, then the matrix element extracted from the splitting measurements are inconsistent with the lifetime and polarizability measurements and theory. A previous study in cesium confirms the theoretical calculations of the matrix elements and the deviation from LS coupling for that particular case [51]. This instills some confidence in the calcula-

Reproduced with permission of the copyright owner. Further reproduction prohibited without permission.

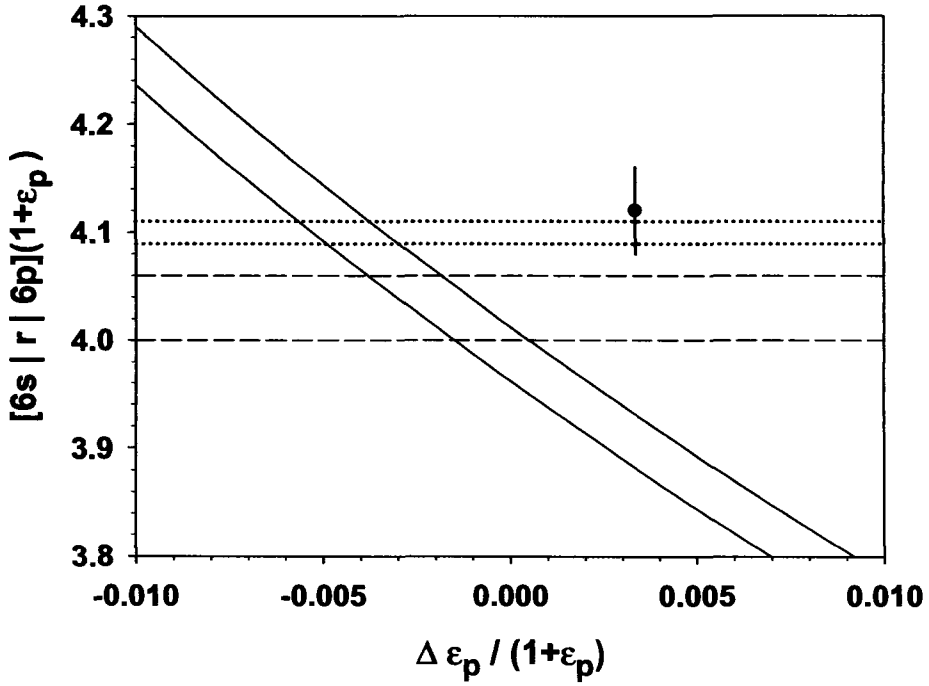

Figure 4.7: The dipole radial matrix elements with only a small deviation factor are plotted versus the deviation from pure LS coupling, $\Delta\epsilon_p/(1+\epsilon_p)$. The area between the solid lines represents one standard deviation of the radial matrix element value obtained from the B_0 parameter. The dashed lines are the limits from experimental lifetime measurements [28]. The values for the radial matrix element and deviation from LS coupling are bounded by the splitting and lifetime measurements. The point represents the theoretical calculation.

Reproduced with permission of the copyright owner. Further reproduction prohibited without permission.

tions and casts doubt on the new method of analysis for the splittings. On the other hand, it is possible to adjust the calculated value for the LS coupling deviation to bring the theory and the three experimental results into good agreement.

The results for the quadrupole radial matrix element and corresponding deviation from pure LS coupling are presented in figure 4.8. In order to extract the quadrupole matrix element the value of B_0 was used to calculate the second term shown in Eq.(4.8). A generous error in $\Delta\epsilon_p/(1+\bar{\epsilon}_p)$ of ± 0.005 was included. The error due to this additional term was not significant compared to the experimental error in B_1. This results in the following constraint,

$$B_1 = 5280(274) = 63.842\left[< g\|\vec{Q}\|D > (1+\bar{\epsilon_d})\right]^2\left[1+6.62\left(\frac{\Delta\epsilon_d}{1+\bar{\epsilon}_d}\right)\right] - 4305(104) \tag{4.15}$$

The quadrupole radial matrix element is plotted as a function of the difference of deviation from pure LS coupling for the two D states, more specifically $\Delta\epsilon_d/(1+\bar{\epsilon}_d)$, as two solid lines representing one standard deviation. The dashed lines bound the value of the radial matrix element as determined by lifetime measurements of both Ba^+ 5D states [29, 31]. The quadrupole polarizability measurement in the previous section is not shown here but is entirely consistent with the lifetime measurements, but is not as precise. The theoretical value, based on the calculated values of both $\langle 6s|r^2|d_{3/2}\rangle$ and $\langle 6s|r^2|d_{5/2}\rangle$ matrix elements, is represented by a point at the value for $\bar{\epsilon}$ which theory predicts. The quadrupole radial matrix element agrees to only within 3 standard deviations of the theoretical predictions. The dotted lines represent the measurements of Shuman et al.

Reproduced with permission of the copyright owner. Further reproduction prohibited without permission.

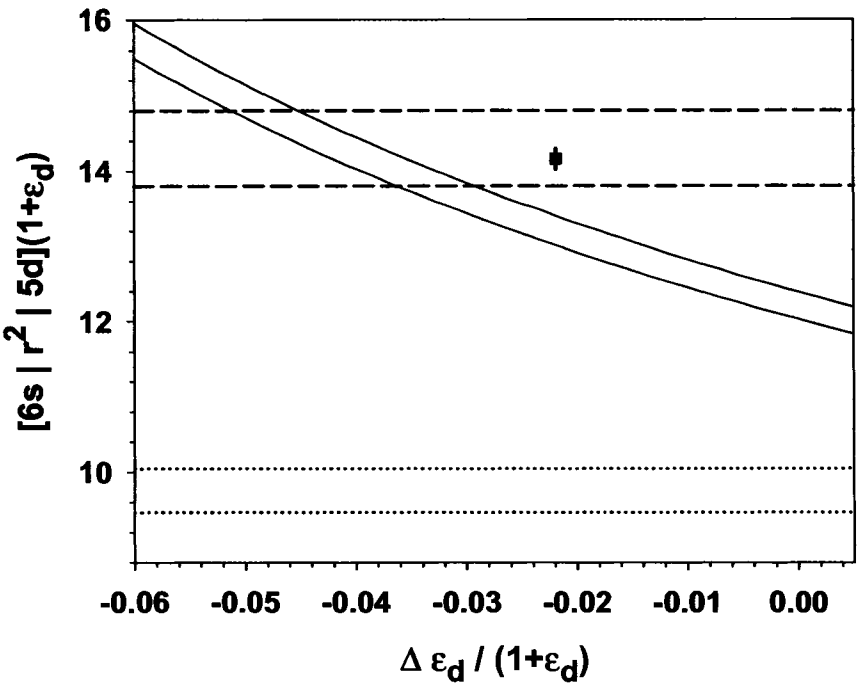

Figure 4.8: The quadrupole radial matrix elements with only a small deviation factor are plotted versus the deviation from pure LS coupling, $\Delta\epsilon_d/(1+\epsilon_d)$. The area between the solid lines represents one standard deviation of the radial matrix element value obtained from the B_1 parameter. The dashed lines are the limits from experimental lifetime measurements [29, 31]. The values for the radial matrix element and deviation from LS coupling are bounded by the splitting and lifetime measurements. The dotted lines represent the bounds put on the radial matrix element by a previous spin splitting analysis by Shuman et al. The square point represents the theoretical calculation.

Reproduced with permission of the copyright owner. Further reproduction prohibited without permission.

The bounds on the quadrupole matrix element disagrees with the previous study by Shuman, et al., $\langle 6s|r^2|5d\rangle = 9.7(3)$ [40]. In Shuman's work, the assumption was made that the states are independent of deviation from pure LS coupling, which seems unlikely. Our results here give $\langle 6s|r|6p\rangle = 3.99(3)$ and $\langle 6s|r^2|5d\rangle = 11.4(7)$ if pure LS coupling is assumed. This agrees well with the results given by Shuman et al. for the dipole radial matrix element, however, the disagreement with the quadrupole matrix element is not fully understood.

The interpretation of the final results, as was also the case for the dipole, is dependent on the assumed value of the deviation from LS coupling. For the case of assuming the theoretical LS deviation, the splitting analysis gives a value of the quadrupole matrix element of 13.2(4). This value for the quadrupole matrix element is 7% lower than the theoretical calculations and nearly two standard deviations from the lifetime measurements. However, if the deviation from LS coupling is larger than the calculated value, then agreement for all the measurements and theory mayb be obtained.

4.5 Conclusions

The long standing discrepancy between theoretical calculations and the extracted quadrupole polarizabilities from fine structure measurements has been resolved. The realization that terms scaling with r^{-7} and $L(L+1)r^{-8}$ significantly affect the slope of the polarization plot differed from the previous assumptions that these terms would only contribute curvature to the data pattern. The slope of a polarization plot can

Reproduced with permission of the copyright owner. Further reproduction prohibited without permission.

now be used to determine the quadrupole polarizability with confidence. This is based on the consistent results between theory and experiment for the three cases in this work; Mg^+, Si^{3+}, and Ba^+.

The dipole polarizabilities of Mg^+ and Ba^+ were determined to be 35.02(4) and 124.09(27) respectively. The quadrupole polarizabilities of Mg^+, Si^{3+}, and Ba^+ were found to be 202(54), 17(4), and 4238(643) respectively. These measurements are all consistent with the best theoretical calculations. The precision on the dipole polarizability measurements are an order of magnitude more precise than the theoretical calculations, which provides an excellent check of the current theory.

For largely non-adiabatic systems, such as barium, splittings appear in the fine structure. These splittings, termed the K splittings or indirect spin-orbit splittings, can be easily explained by including the ion core fine structure in the polarization model. This entirely non-adiabatic characteristic is sensitive to the difference from pure LS coupling, the core fine structure, and the values of the matrix elements of the ion core.

New methods of analysis for the spin splittings has been developed in this work. It is not possible with measurements of just the spin splittings to obtain unique values for both the deviation from LS coupling and the corresponding matrix elements. However, comparison with theory and lifetime measurements can provide insight. If the deviation from LS coupling from theory is assumed to be correct, then a discrepancy exists between the splitting measurements and both the lifetime measurements and theory. On the other hand, if adjustments are made to the theoretical deviation

Reproduced with permission of the copyright owner. Further reproduction prohibited without permission.

from *LS* coupling it may be possible to bring all the measurements and theory into agreement.

Reproduced with permission of the copyright owner. Further reproduction prohibited without permission.

Appendix A

Details of spinless calculation

This Appendix gives details of how to obtain the relations given in the main text (Eqs.(1.22)(1.16)). The calculation begins by using the radial wave equation satisfied by the Rydberg radial wavefunction,

$$\left(\frac{1}{Z}\right)^2\left[\frac{d^2}{dr^2}+\frac{2Z}{r}-\frac{L(L+1)}{r^2}\right]P_{nL}(r)=\frac{1}{n^2}P_{nL}(r) \tag{A.1}$$

The following term is part of the summation of interest in this calculation,

$$(\frac{1}{n^2}-\frac{1}{n'^2})<nL|r^{-s}|n'L'> \tag{A.2}$$

Substitution of the radial wave equation gives,

$$\begin{aligned}\left(\frac{1}{n_2}-\frac{1}{n'^2}\right)\left\langle n',l'\left|r^{-s}\right|n,l\right\rangle &= \left(\frac{1}{Z}\right)^2\int r^{-s}P_{n'L'}\frac{d^2P_{nL}}{dr^2}dr\\ &-\left(\frac{1}{Z}\right)^2\int r^{-s}P_{nL}\frac{d^2P_{n'L'}}{dr^2}dr\\ &-\left(\frac{1}{Z}\right)^2[L(L+1)-L'(L'+1)]\int r^{-s-2}P_{nL}P_{n'L'}dr.\end{aligned} \tag{A.3}$$

Reproduced with permission of the copyright owner. Further reproduction prohibited without permission.

The first term in Eq.(A.3) can be rewritten using integration by parts as

$$\int r^{-s}P_{n'L'}\frac{d^2P_{nL}}{dr^2}dr = \int r^{-s}P_{nL}\frac{d^2P_{n'L'}}{dr^2}dr + s(s+1)\int r^{-s-2}P_{nL}P_{n'L'}dr - 2s\int r^{-s-1}P_{nL}\frac{dP_{n'L'}}{dr}dr \quad (A.4)$$

This can be substituted back into Eq.(A.2), which results in

$$\left(\frac{1}{n_2}-\frac{1}{n'^2}\right)\langle n',l'\left|r^{-s}\right|n,l\rangle = -2s\left(\frac{1}{Z}\right)^2\int r^{-s-1}P_{nL}\frac{dP_{n'L'}}{dr}dr + [s(s+1)-L(L+1)+L'(L'+1)]\left(\frac{1}{Z}\right)^2\int r^{-s-2}P_{nL}P_{n'L'}dr \quad (A.5)$$

Integration by parts is performed on the first term one more time and then the entire result is multiplied by $\langle nL|r^{-s}|n'L'\rangle$. Now the summation over n' in the relationship given in Eq.(1.16) can be written as

$$\sum_{n'}\left(\frac{1}{n_2}-\frac{1}{n'^2}\right)\left|\langle n',l'\left|r^{-s}\right|n,l\rangle\right|^2 = +2s\left(\frac{1}{Z}\right)^2\int r_1^{-s-1}P_{n'L'}\frac{dP_{nL}}{dr_1}dr_1\int r_2^{-s}P_{nL}P_{n'L'}dr_2 + [-s(s+1)-L(L+1)+L'(L'+1)]\left(\frac{1}{Z}\right)^2 \times \int r_1^{-s-2}P_{nL}P_{n'L'}dr_1\int r_2^{-s}P_{nL}P_{n'L'}dr_2 \quad (A.6)$$

Now invoking completeness, which states

$$\sum_{n'}P_{n'l'}(r_1)P_{n'l'}(r_2) = \delta(r_1-r_2), \quad (A.7)$$

the relation can be written as

$$\sum_{n'}\left(\frac{1}{n_2}-\frac{1}{n'^2}\right)\left|\langle n',l'\left|r^{-s}\right|n,l\rangle\right|^2 = 2s\left(\frac{1}{Z}\right)^2\int r^{-2s-1}P_{nL}\frac{dP_{nL}}{dr}dr + [-s(s+1)-L(L+1)+L'(L'+1)]\left(\frac{1}{Z}\right)^2\int r^{-2s-2}P_{nL}^2dr \quad (A.8)$$

Reproduced with permission of the copyright owner. Further reproduction prohibited without permission.

Using integration by parts yet again, the first term can be rewritten in terms of, $\langle r^{-2s-2}\rangle$, the expectation value of the radial matrix element. This brings us to the relation given in Eq.(1.16) of the main text.

In order to obtain the relation given to calculate the 2nd non-adiabatic dipole, we must back track to Eq.(A.5). From this point, again integration by parts must be performed on the first term as before. Now instead of only multiplying by the expectation of the radial matrix element, we must square the whole equation and invoke completeness of the radial wave function again. By doing this the left side of the equation is exactly what we want to sum over and the right side it will be shown that it can be reduced to that given in Eq.(1.16) from Chapter 1.

$$\begin{aligned}
&\left|\langle n', L'\left|r^{-s}\right|n, L\rangle\right|^2\left(\frac{1}{n_2}-\frac{1}{n'^2}\right)^2 = \\
&\quad +\left[-s(s+1)-L(L+1)+L'(L'+1)\right]^2\left(\frac{1}{Z}\right)^2\left\langle r^{-2s-4}\right\rangle \\
&\quad +2s\left[-s(s+1)-L(L+1)+L'(L'+1)\right]\left(\frac{1}{Z}\right)^2\int r^{-2s-3}\frac{dP_{nL}}{dr}P_{nL}dr \\
&\quad +4s^2\left(\frac{1}{Z}\right)^2\int r^{-2s-2}\left(\frac{dP_{nL}}{dr}\right)^2 dr. \qquad \text{(A.9)}
\end{aligned}$$

Integration by parts must be utilized yet again, reducing Eq.(A.10) to

$$\begin{aligned}
&\left|\langle n', L'\left|r^{-s}\right|n, L\rangle\right|^2\left(\frac{1}{n_2}-\frac{1}{n'^2}\right)^2 = \\
&\quad +\left[-s(s+1)-L(L+1)+L'(L'+1)\right]^2\left(\frac{1}{Z}\right)^2\left\langle r^{-2s-4}\right\rangle \\
&\quad +(2s+3)s\left[-s(s+1)-L(L+1)+L'(L'+1)\right]\left(\frac{1}{Z}\right)^2\left\langle r^{-2s-4}\right\rangle \\
&\quad +4s^2\left(\frac{1}{Z}\right)^2\left((s+1)(2s+3)\left\langle r^{-2s-4}\right\rangle-\int r^{-2s-2}P_{nL}\frac{d^2P_{nL}}{dr^2}dr\right). \qquad \text{(A.10)}
\end{aligned}$$

In order to evaluate the last term in the equation directly above, the radial wave equation can be substituted back in for $\frac{d^2P_{nL}}{dr^2}$. Integration by parts will simplify

Reproduced with permission of the copyright owner. Further reproduction prohibited without permission.

the term after substitution of the radial wave equation is performed. This gives the following general which can be tailored to a particular case such as the dipole (s=2) or quadrupole (s=3),

$$\begin{aligned}\sum_{n'} \left|\langle n', L' \left| r^{-s} \right| n, L\rangle\right|^2 \left(\frac{1}{n_2} - \frac{1}{n'^2}\right)^2 = \\ +[-s(s+1) - L(L+1) + L'(L'+1)]^2 \left(\frac{1}{Z}\right)^2 \left\langle r^{-2s-4}\right\rangle \\ +(2s+3)s\,[-s(s+1) - L(L+1) + L'(L'+1)] \left(\frac{1}{Z}\right)^2 \left\langle r^{-2s-4}\right\rangle \\ +4(s+1)(2s+3)s^2 \left(\frac{1}{Z}\right)^2 \left\langle r^{-2s-4}\right\rangle \\ -4s^2 \left(\frac{1}{Z}\right)^2 \left(-2Z\left\langle r^{-2s-3}\right\rangle + L(L+1)\left\langle r^{-2s-4}\right\rangle + \frac{1}{n^2}\left\langle r^{-2s-2}\right\rangle\right).\end{aligned} \tag{A.11}$$

For the particular case of s=2, the relation given by Drachman (See Eq.(1.23)) can simplify the last term. This results in one other term that scales with r^{-7} which is of interest here.

Reproduced with permission of the copyright owner. Further reproduction prohibited without permission.

Appendix B

Observed RESIS Microwave Lines

B.1 Magnesium n=17 and n=20 Microwave Lines

A co-propagating microwave scan is shown below for each of the magnesium intervals observed in this study.

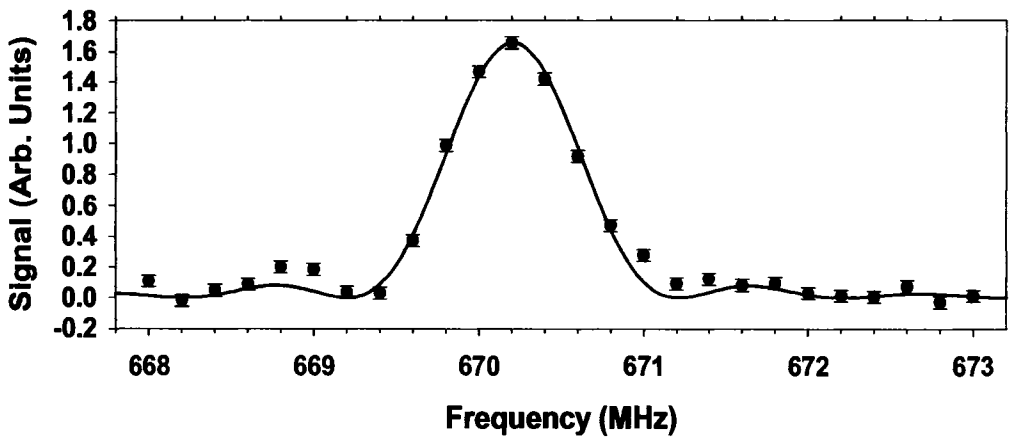

Figure B.1: Mg 17K-17L copropagating

Reproduced with permission of the copyright owner. Further reproduction prohibited without permission.

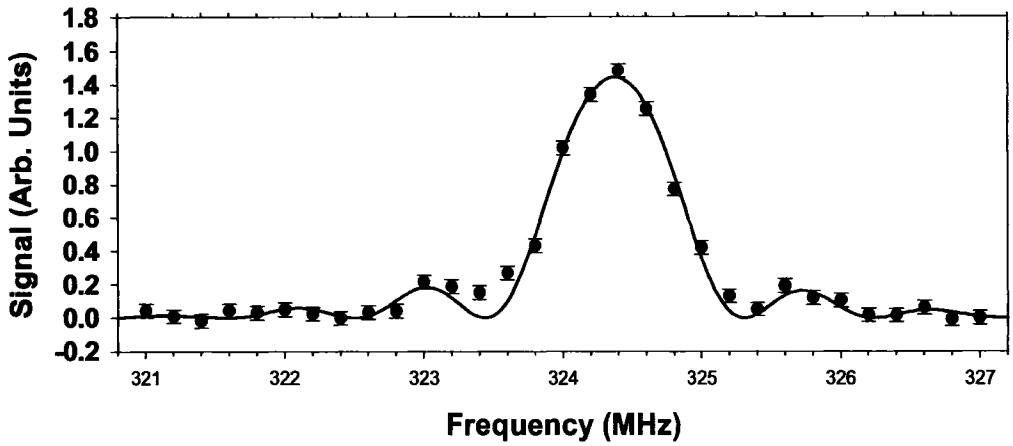

Figure B.2: Mg 17L-17M copropagating

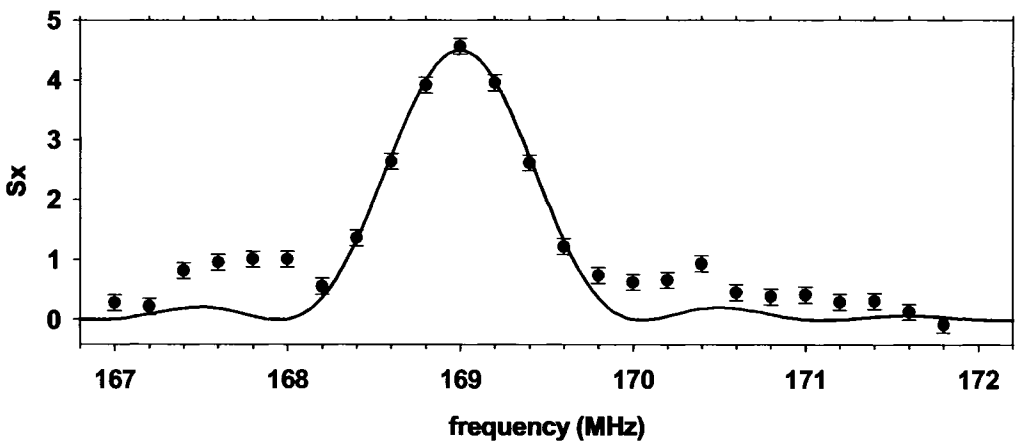

Figure B.3: Mg 17M-17N copropagating

Reproduced with permission of the copyright owner. Further reproduction prohibited without permission.

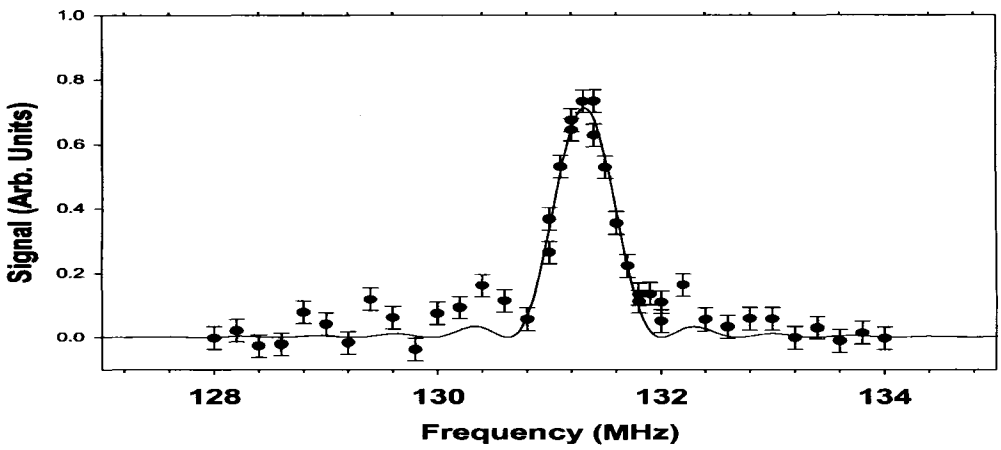

Figure B.4: Mg 17M-17O copropagating

Reproduced with permission of the copyright owner. Further reproduction prohibited without permission.

The observed line shape revealed an asymmetry in n=20 levels of magnesium. This is strongly dependent on the sensitivity of the transition to electric fields. It is possible that this line shape is due to inhomogeneous DC electric fields that develop as a result of charge deposition in the region. This would essentially act as two or more different regions with different geometries and therefore one would expect to observe different line widths and saturation curves for each segment. Effects arising from inhomogeneous DC fields have previously been observed to be greatly reduced or eliminated by heating the microwave region, and heating of the region had no effect on the asymmetric line shape. Inspection of the microwave input signal observed before and after the region affirmed that the line shape is not a result of asymmetries in the microwave field produced in the region or interference with reflections.

Reproduced with permission of the copyright owner. Further reproduction prohibited without permission.

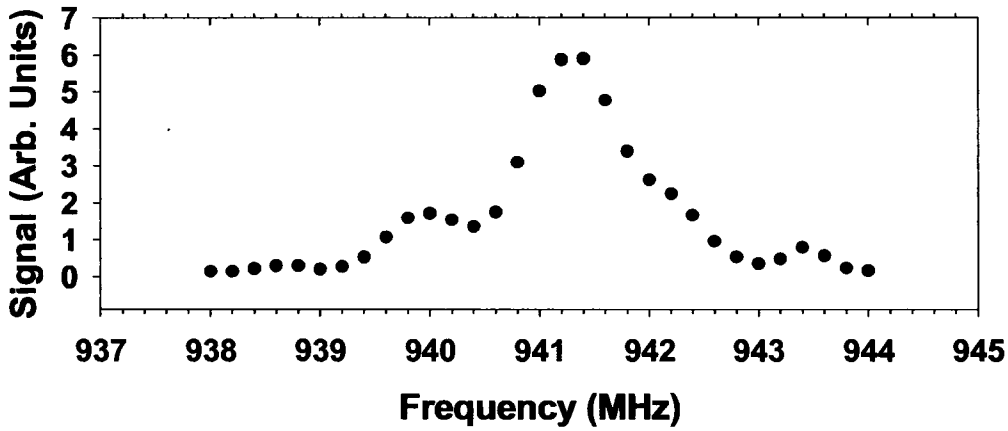

Figure B.5: Mg 20I-20K counterpropagating

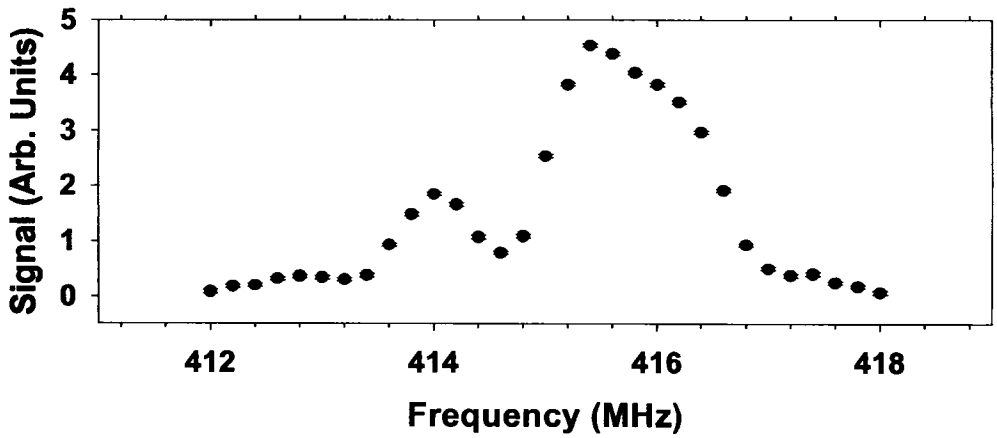

Figure B.6: Mg 20K-20L counterpropagating

Reproduced with permission of the copyright owner. Further reproduction prohibited without permission.

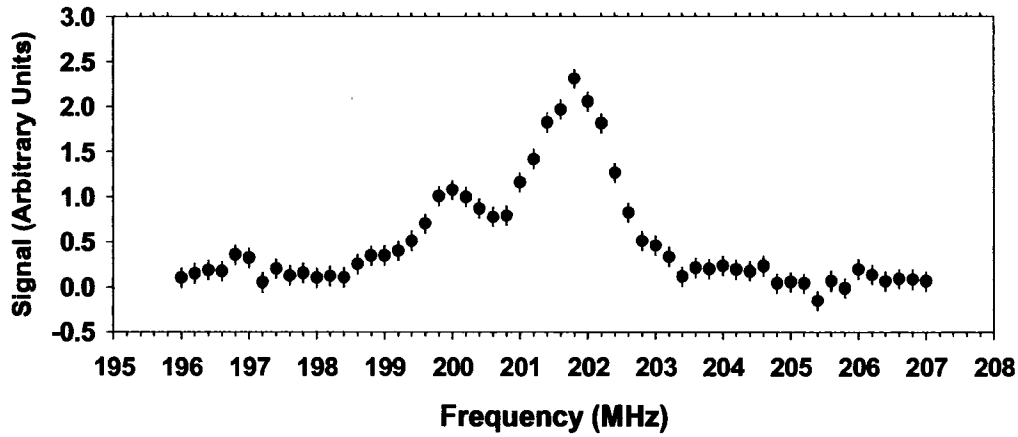

Figure B.7: Mg 20L-20M counterpropagating

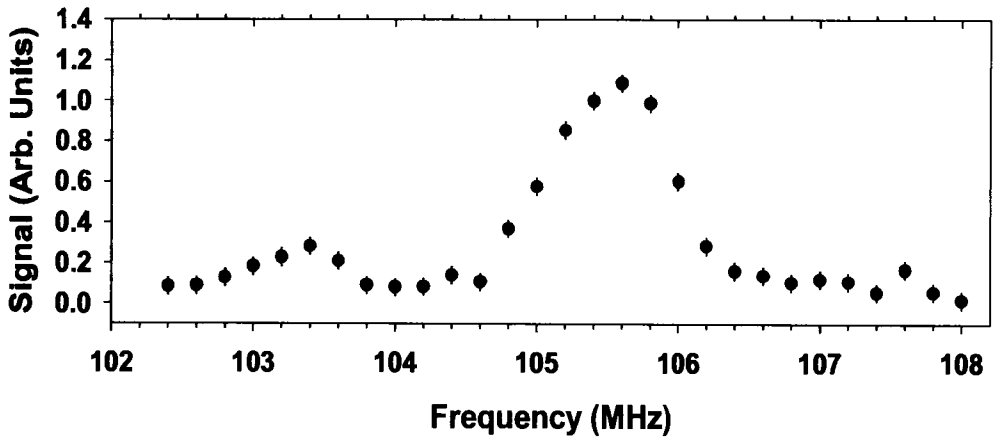

Figure B.8: Mg 20M-20N counterpropagating

Reproduced with permission of the copyright owner. Further reproduction prohibited without permission.

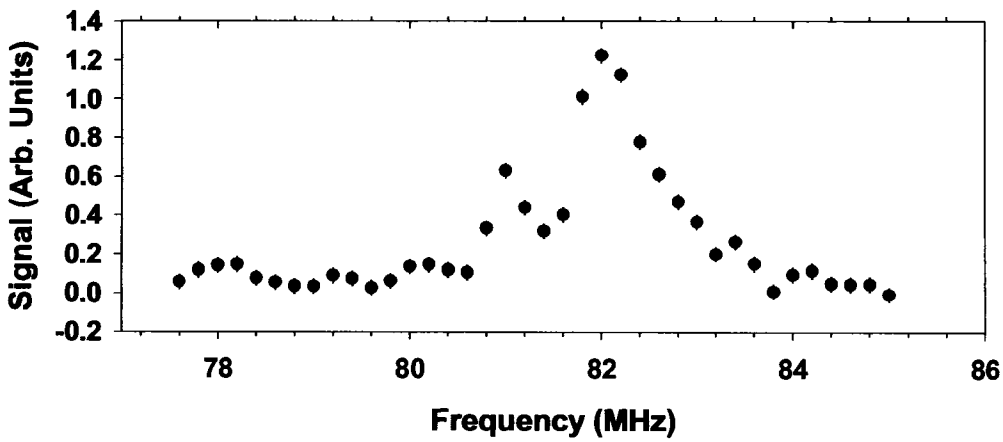

Figure B.9: Mg 20M-20O counterpropagating

Reproduced with permission of the copyright owner. Further reproduction prohibited without permission.

B.2 Barium n=17 and 20 RESIS Microwave Lines

An example of each barium microwave transition is shown below.

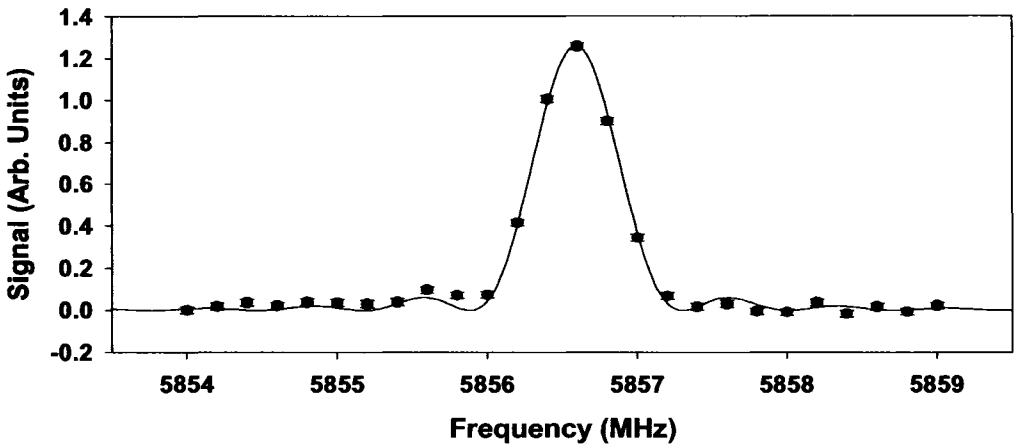

Figure B.10: Ba $17I_{5.5}$-$17K_{6.5}$ copropagating

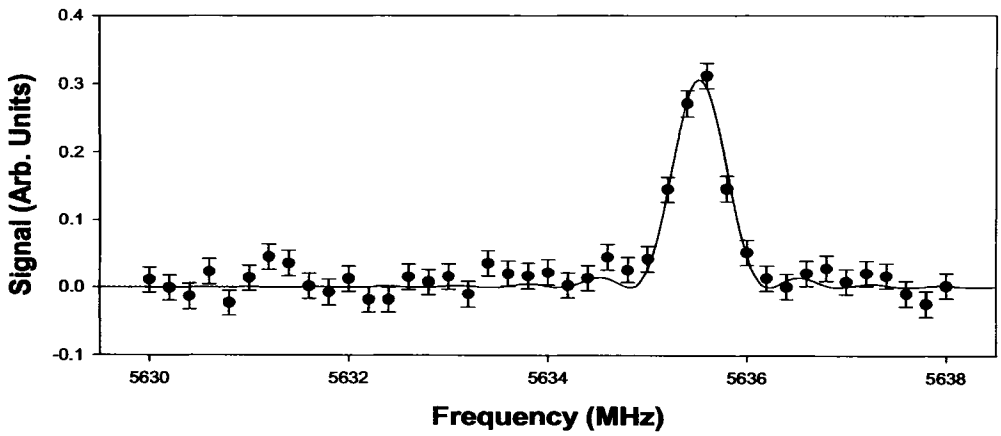

Figure B.11: Ba $17I_{6.5}$-$17K_{7.5}$ copropagating

Reproduced with permission of the copyright owner. Further reproduction prohibited without permission.

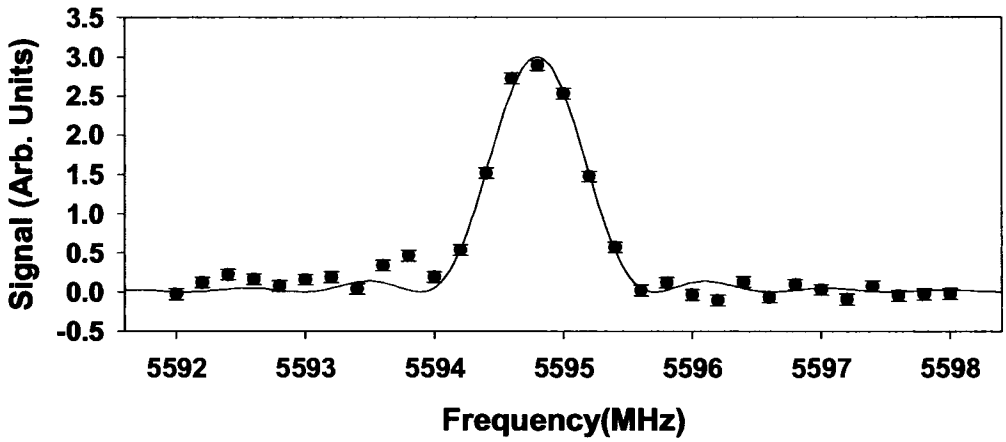

Figure B.12: Ba $17I_{6.5}$-$17K_{6.5}$ copropagating

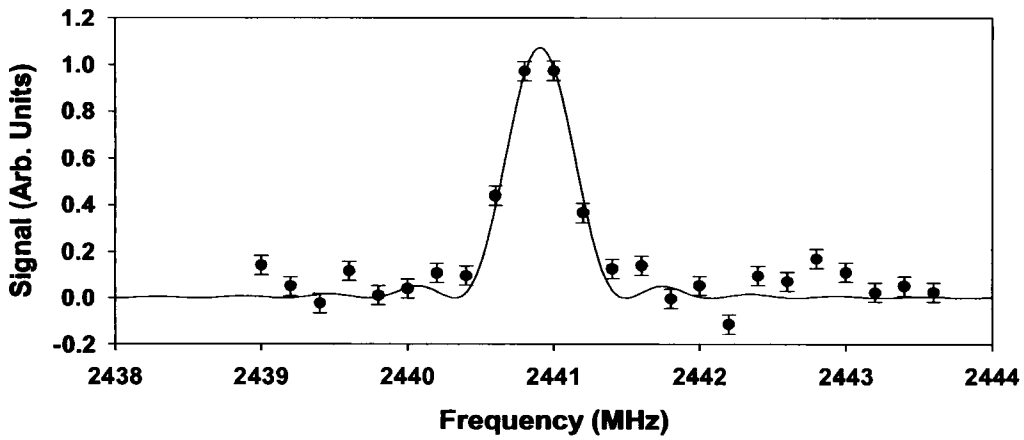

Figure B.13: Ba $17K_{6.5}$-$17L_{7.5}$ copropagating

Reproduced with permission of the copyright owner. Further reproduction prohibited without permission.

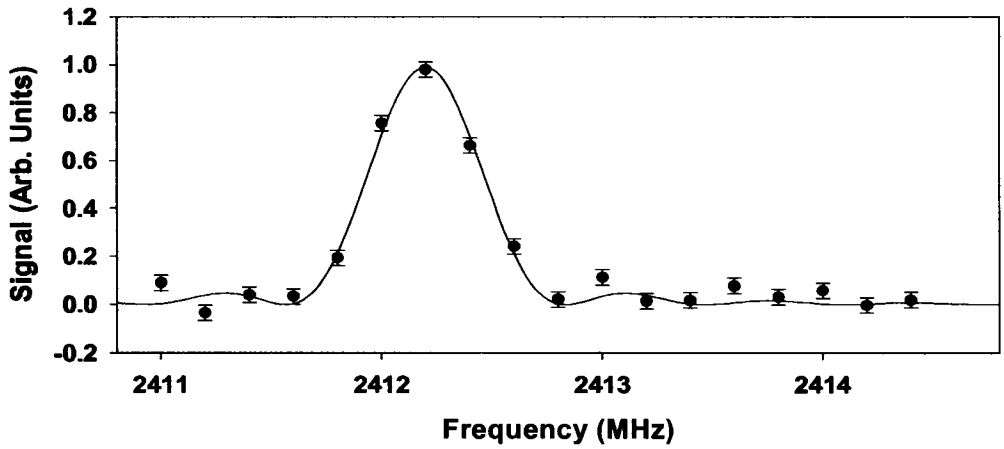

Figure B.14: Ba $17K_{7.5}$-$17L_{8.5}$ copropagating

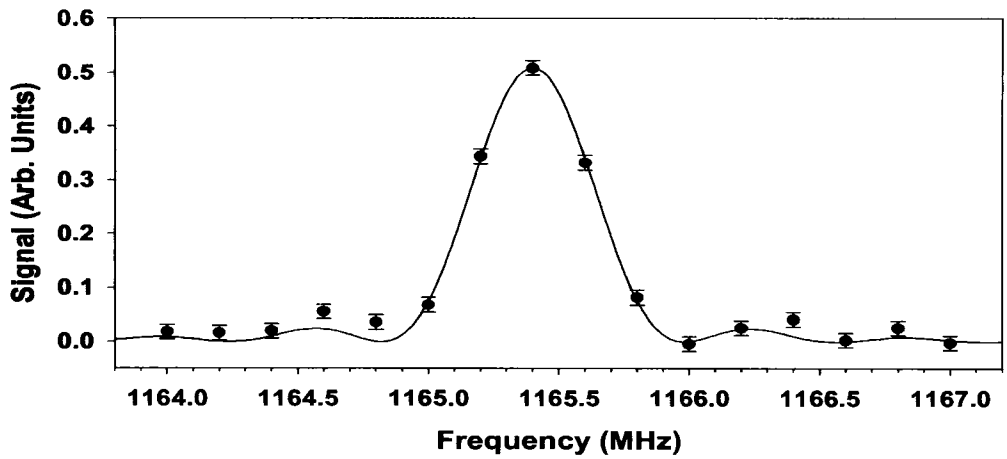

Figure B.15: Ba $17L_{7.5}$-$17M_{8.5}$ counter-propagating

Reproduced with permission of the copyright owner. Further reproduction prohibited without permission.

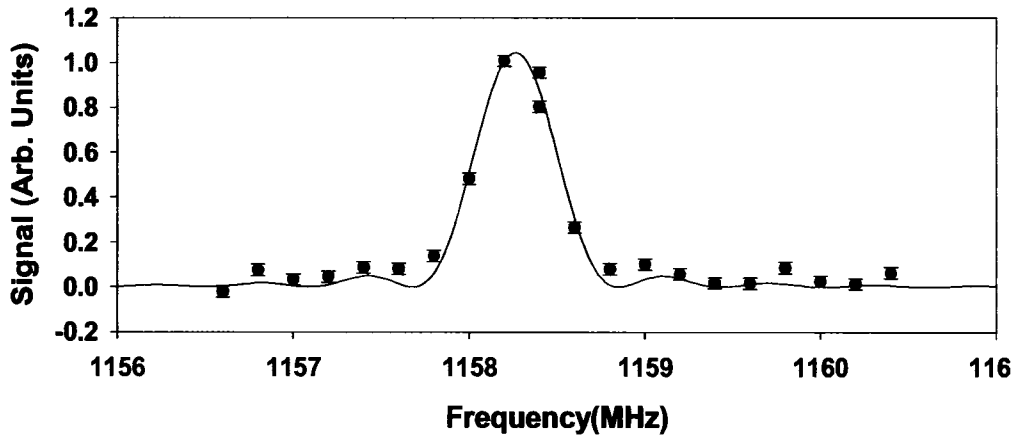

Figure B.16: Ba $17L_{8.5}$-$17M_{9.5}$ copropagating

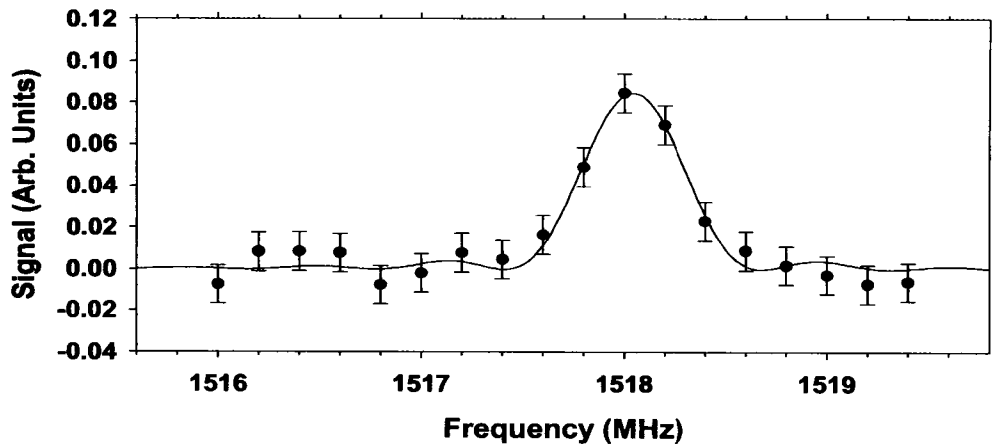

Figure B.17: Ba $20K_{6.5}$-$20L_{7.5}$ counter-propagating

Reproduced with permission of the copyright owner. Further reproduction prohibited without permission.

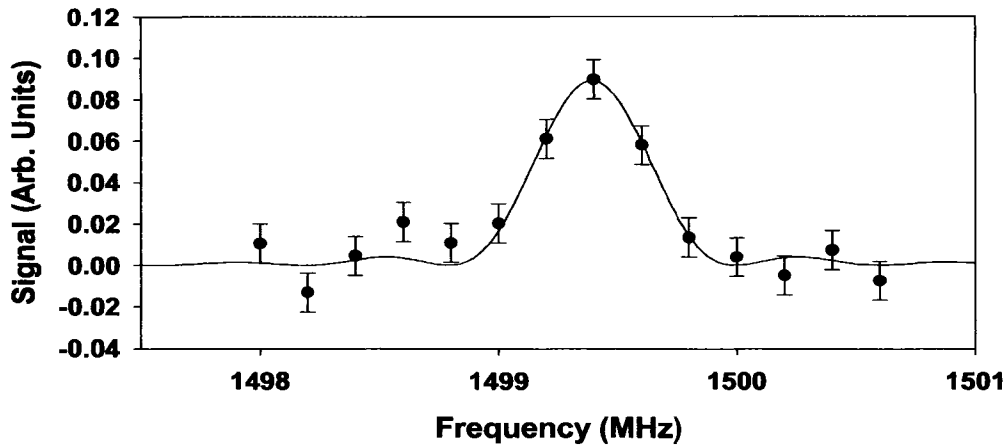

Figure B.18: Ba $20K_{7.5}$-$20L_{8.5}$ counter-propagating

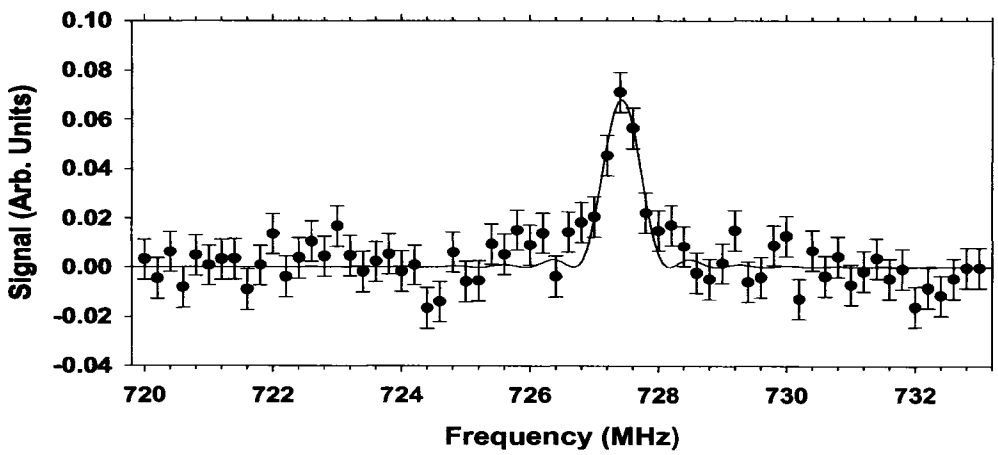

Figure B.19: Ba $20L_{7.5}$-$20M_{8.5}$ counter-propagating

Reproduced with permission of the copyright owner. Further reproduction prohibited without permission.

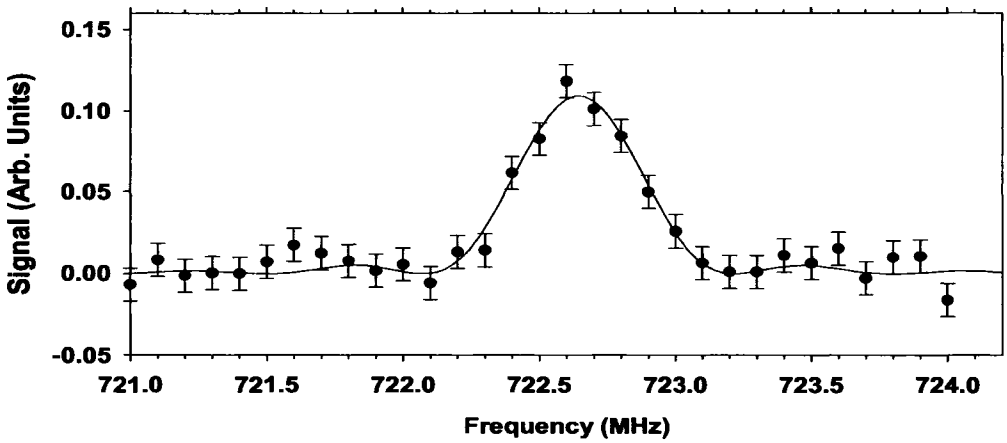

Figure B.20: Ba $20L_{8.5}$-$20M_{9.5}$ copropagating

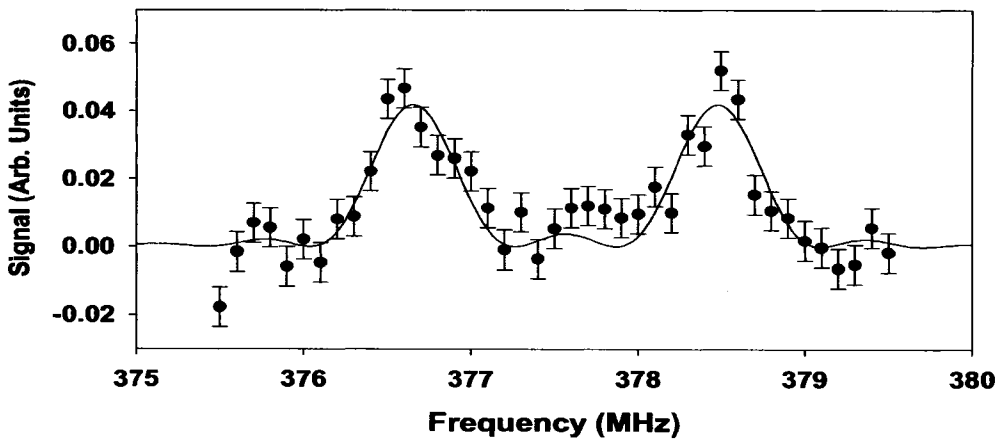

Figure B.21: Ba $20M_{8.5}$-$20N_{9.5}$ and Ba $20M_{9.5}$-$20N_{10.5}$ copropagating

Reproduced with permission of the copyright owner. Further reproduction prohibited without permission.

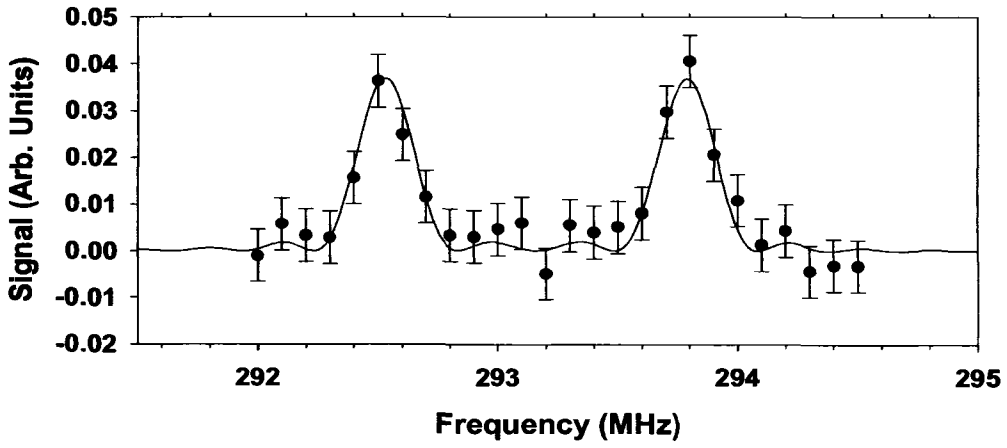

Figure B.22: Ba $20M_{8.5}$-$20O_{10.5}$ and Ba $20M_{9.5}$-$20N_{11.5}$ counter-propagating

Reproduced with permission of the copyright owner. Further reproduction prohibited without permission.

Appendix C

Matrix Elements

The following absolute values of the matrix elements were provided by the theory group at University of Delaware directed by M. Safronova. These matrix elements were used in their calculation of the dipole and quadrupole polarizabilities for Mg^+, Si^{3+}, and Ba^+ which are given in Table 4.

Table C.1: Absolute value of theoretical dipole and quadrupole matrix elements of Ba^+ are given here in atomic units. An uncertainty of 1% is assigned to all of the values.

transition	Dipole	transition	Quadrupole
6S1/2 - 6P1/2	3.37	6S1/2 - 5D3/2	12.53
6S1/2 - 6P3/2	4.75	6S1/2 - 5D5/2	15.69
6P1/2 - 5D3/2	3.05	6P1/2 - 6P3/2	28.08
6P3/2 - 5D3/2	1.33	6P3/2 - 6P3/2	28.08
6P3/2 - 5D5/2	4.11		

Reproduced with permission of the copyright owner. Further reproduction prohibited without permission.

Table C.2: Absolute value of theoretical dipole and quadrupole matrix elements of Mg^+ are given here in atomic units. An uncertainty of 0.5% is assigned to all of the values.

transition	Dipole	transition	Quadrupole
3S1/2 - 3P1/2	2.369	3S1/2 - 3D3/2	9.873
3S1/2 - 3P3/2	3.351	3S1/2 - 3D5/2	12.092
3P1/2 - 3D3/2	4.158	3P1/2 - 3P3/2	12.309
3P3/2 - 3D3/2	1.862	3P3/2 - 3P3/2	12.309
3P3/2 - 3D5/2	5.587		

Table C.3: Absolute value of theoretical dipole and quadrupole matrix elements of Si^{3+} are given here in atomic units. An uncertainty of 0.04% is assigned to all of the values.

transition	Dipole	transition	Quadrupole
3S1/2 - 3P1/2	1.530	3S1/2 - 3D3/2	4.11
3S1/2 - 3P3/2	2.165	3S1/2 - 3D5/2	5.028
3P1/2 - 3D3/2	2.436	3P1/2 - 3P3/2	4.341
3P3/2 - 3D3/2	1.091	3P3/2 - 3P3/2	4.341
3P3/2 - 3D5/2	3.273		

Table C.4: Theoretical dipole and quadrupole polarizabilities of Mg^+, Si^{3+}, and Ba^+ are given here in atomic units.

	Mg^+	Si^{3+}	Ba^+
α_d	35.01	7.418(9)	124.7(2.5)
β_d	106.0	11.0	598(10)
α_Q	156.0	11.2	4145(78)

Reproduced with permission of the copyright owner. Further reproduction prohibited without permission.

Appendix D

Hydrogenic Mean Values of r^{-S}

Radial expectation values for hydrogenic atoms or ions are given explicitly for powers of -4, -6, -7 and -8 [52]. The core ion mass is represented by M and the electron mass is m. The results are given in atomic units.

$$\langle r^{-4}\rangle = \left(\frac{Q}{1+\frac{m}{M}}\right)^4 \frac{3n^2 - L(L+1)}{2n^5(L-\frac{1}{2})L(L+\frac{1}{2})(L+1)(L+\frac{3}{2})}, \qquad (L>0)$$

$$\langle r^{-6}\rangle = \left(\frac{Q}{1+\frac{m}{M}}\right)^6 \frac{35n^4 - n^2[30L(L+1)-25] + 3(L-1)L(L+1)(L+2)}{8n^7(L-\frac{3}{2})(L-1)(L-\frac{1}{2})L(L+\frac{1}{2})(L+1)(L+\frac{3}{2})(L+2)(L+\frac{5}{2})}, \qquad (L>1)$$

$$\langle r^{-7}\rangle = \left(\frac{Q}{1+\frac{m}{M}}\right)^7 \frac{63n^4 - n^2[70L(L+1)-105] + 15(L-1)L(L+1)(L+2) - 20L(L+1) + 12}{8n^7(L-2)(L-\frac{3}{2})(L-1)(L-\frac{1}{2})L(L+\frac{1}{2})(L+1)(L+\frac{3}{2})(L+2)(L+\frac{5}{2})(L+3)},$$
$$(L>2)$$

$$\langle r^{-8}\rangle = \frac{\left(\frac{Q}{1+\frac{m}{M}}\right)^8}{16n^9(L-\frac{5}{2})(L-2)(L-\frac{3}{2})(L-1)(L-\frac{1}{2})L(L+\frac{1}{2})(L+1)(L+\frac{3}{2})(L+2)(L+\frac{5}{2})(L+3)(L+\frac{7}{2})}$$
$$\times\Big[231n^6 - n^4[315L(L+1)-735] + n^2[105(L-1)L(L+1)(L+2) - 315L(L+1) + 294]$$
$$-5(L-2)(L-1)L(L+1)(L+2)(L+3)\Big], \qquad (L>2) \qquad \text{(D.1)}$$

Reproduced with permission of the copyright owner. Further reproduction prohibited without permission.

Bibliography

[1] Chun C. Lin and Paul Berman, editors. "Fine Structure in High-L Rydberg states: A Path to Properties of Positive Ions" *in Advances in Atomic, Molecular, and Optical Physics*, volume 52. Academic Press, (2005).

[2] J. E. Mayer and M. G. Mayer. *Phys. Rev.* **43**, 605 (1933).

[3] J. H. Van Vleck and N. G. Whitelaw. *Phys. Rev.* **44**, 551 (1933).

[4] R. J. Drachman. *Phys. Rev. A* **26**, 1228 (1982).

[5] P. Risberg. *Arkiv for Fysik* **9**, 483 (1955).

[6] C. H. H. Van Deurzen. *J. Opt. Soc. Am.* **67**, 476 (1977).

[7] C. J. Sansonetti, K. L. Andrew, and J. Vergese. *J. Opt. Soc. Am.* **71**, 423 (1981).

[8] G. Herzberg and Ch. Jungen. *J. Chem. Phys.* **77**, 5876 (1982).

[9] Ch. Jungen, I. Dabrowski, G. Herzberg, and D. J. W. Kendall. *J. Chem. Phys.* **91**, 3926 (1989).

[10] J. Brault and R. Noyes. *Astrophysical Journal* **269**, L61 (1983).

[11] E. S. Chang and R. W. Noyes. *Astrophysical Journal* **275**, L11 (1983).

Reproduced with permission of the copyright owner. Further reproduction prohibited without permission.

[12] K. A. Safinya, T. F. Gallagher, and W. Sander. **22**, 2672 (1980).

[13] T. F. Gallagher, R. Kachru, and N. H. Tran. *Phys. Rev. A* **26**, 2611 (1982).

[14] A. G. Vaidyanathan, W. P. Spencer, J. R. Rubbmark, H. Kuiper, C. Fabre, D. Kleppner, and T. W. Ducas. *Phys. Rev. A* **26**, 3346 (1982).

[15] B. J. Lyons and T. F. Gallagher. *Phys. Rev. A* **57**, 2426 (1983).

[16] E. A. Hessels, P. W. Arcuni, F. J. Deck, and S. R. Lundeen. *Phys. Rev. A* **46**, 2622 (1992).

[17] R. F. Ward Jr., W. G. Sturrus, and S. R. Lundeen. *Phys. Rev. A* **53**, 113 (1996).

[18] W. G. Sturrus, E. A. Hessels, P. W. Arcuni, and S. R. Lundeen. *Phys. Rev. A* **44**, 4400 (1991).

[19] R. A. Komara, M. A. Gearba, C. H. Fehrenbach, and S. R. Lundeen. *J. Phys. B At. Mol. Opt. Phys.* **38** (2005).

[20] R. A. Komara, M. A. Gearba, S. R. Lundeen, and C. H. Fehrenbach. *Phys. Rev. A* **67**, 062502 (2003).

[21] L. J. Curtis. *Phys. Rev. A* **23**, 362 (1981).

[22] M. S. Safronova. Unpublished.

[23] E. L. Snow, M. A. Gearba, R. A. Komara, W. G. Sturrus, and S. R. Lundeen. *Phys. Rev. A* **71**, 022510 (2005).

[24] S. C. Bennett and C. E. Wieman. *Phys. Rev. Lett.* **82**, 2484 (1999).

Reproduced with permission of the copyright owner. Further reproduction prohibited without permission.

[25] J. E. Simsarian, S. Aubin, J. S. Grossman, L. A. Orozco, M. R. Pearson, G. D. Sprouse, and W. Z. Zhao. *Parity Violations in Atoms and Polarized Electron Scattering*, p. 312. World Scientific, Singapore (1999).

[26] T. W. Koerber, M. Schacht, W. Nagourney, and E. N. Fortson. *J. Phys. B At. Mol. Opt. Phys.* **36**, 637 (2003).

[27] V. A. Dzuba, V. V. Flambaum, and J. S. M. Ginges. *Phys. Rev. A* **63**, 062101 (2001).

[28] E. H. Pinnington, R. W. Berends, and M. Lumsden. *J. Phys. B At. Mol. Opt. Phys.* **28**, 2095 (1995).

[29] W. Nagourney N. Yu and H. Dehmelt. *Phys. Rev. Lett.* **78**, 4898 (1997).

[30] W. Nagourney, J. Sandberg, and H. Dehmelt. *Phys. Rev. Lett.* **56**, 2797 (1986).

[31] A. Madej and J. Sankey. *Phys. Rev. A* **41**, 2621 (1990).

[32] J. A. Sherman, T. W. Koerber, A. Markhotok, W. Nagourney, and E. N. Fortson. *Phys. Rev. Lett.* **94**, 243001 (2005).

[33] P. L. Jacobson, R. A. Komara, W. G. Sturrus, and S. R. Lundeen. *Phys. Rev. A* **62**, 012509 (2000).

[34] William Clark, Chris H. Greene, and Gregory Miecznik. *Phys. Rev. A* **53**, 2248 (1996).

[35] W. G. Schoenfeld. PhD thesis, University of Massachusetts, (1994).

[36] C. Laughlin. *J. Phys. B At. Mol. Opt. Phys.* **28**, 2787 (1995).

Reproduced with permission of the copyright owner. Further reproduction prohibited without permission.

[37] A. R. Edmonds. *Angular Momentum in Quantum Mechanics.* Princeton University Press, (1960).

[38] E. A. Hessels, W. G. Sturrus, David R. Cok, and S. R. Lundeen. *Phys. Rev. A* **35**, 4489 (1987).

[39] E. L. Snow, R. A. Komara, M. A. Gearba, and S. R. Lundeen. *Phys. Rev. A* **68**, 022510 (2003).

[40] E. S. Shuman and T. F. Gallagher. *Phys. Rev. A* , 022502 (2006).

[41] Yu. Ralchenko, F.-C. Jou, D. E. Kelleher, A. E. Kramida, A. Musgrove, J. Reader, W. L. Wiese, and K. Olsen. (2006). *NIST Atomic Spectra Database* (version 3.1.0). [Online]. Available: http://www.physics.nist.gov/asd3 [2006, July].

[42] B. Zygelman. *Phys. Rev. Lett.* **64**, 256 (1990).

[43] G. D. Stevens and S. R. Lundeen. *Comments on Atomic and Molecular Physics, Comments on Modern Physics* **1**, Part D, pp. 207–219 (2000).

[44] C. W. Fehrenbach, S. R. Lundeen, and O. L. Weaver. *Phys. Rev. A* **51** (1995).

[45] P. L. Jacobson. PhD thesis, Colorado State University, (1998).

[46] M. J. Weber, editor. *Handbook of Laser Science and Technology*, volume 2. CRC Press, Boca Raton, (1982).

[47] G. W. F. Drake. *Atomic, Molecular, and Optical Physics Handbook.* AIP.

[48] E. A. Hessels. PhD thesis, University of Notre Dame, (1992).

Reproduced with permission of the copyright owner. Further reproduction prohibited without permission.

[49] G. W. F. Drake and R. A. Swainson. *Phys. Rev. A* **44**, 5448 (1991).

[50] Alan Gallagher. *Phys. Rev.* **157**, 24 (1967).

[51] A. Sieradzan, M. D. Havey, and M. S. Safronova. *Phys. Rev. A* **69**, 022502 (2004).

[52] Kjell Bockasten. *Phys. Rev. A* **9**, 1087 (1974).

Reproduced with permission of the copyright owner. Further reproduction prohibited without permission.